

UNIVERSITY OF SOUTH AFRICA

DOCTORAL THESIS

**VLBI Imaging of ICRF Sources in the
Southern Hemisphere using Geodetic
and Astrometric Observations**

Author:
Sayan Basu

Supervisors:
Prof. Lerothodi L. Leeuw
Dr Aletha de Witt
Dr Jonathan Quick

*A thesis submitted in fulfilment of the requirements
for the degree of Doctor of Philosophy*

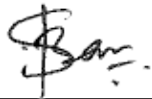
*in
Astronomy*

Department of Mathematical Sciences
University of South Africa

Declaration of Authorship

I, Sayan Basu, declare that this thesis, titled ‘VLBI Imaging of ICRF Sources in the Southern Hemisphere using Geodetic and Astrometric Observations’, and the work presented in it are my own. I confirm that:

- This work was done wholly while in candidature for a research degree at this University.
- I have not previously submitted this work, or part of it, for examination at Unisa for another qualification or at any other higher education institution.
- Where I have consulted the published work of others, this is always clearly attributed.
- Where I have quoted from the work of others, the source is always given. With the exception of such quotations, this thesis is entirely my own work.
- I have acknowledged all main sources of help.
- Where the thesis is based on work done by myself jointly with others, I have made clear exactly what was done by others and what I have contributed myself.



21.05.2020

Sayan Basu

Date

Student Number: 53502671

“Know how to solve every problem that has ever been solved”

Richard Feynman

UNIVERSITY OF SOUTH AFRICA

Abstract

College of Science, Engineering and Technology

Department of Mathematical Sciences

Doctor of Philosophy

VLBI Imaging of ICRF Sources in the Southern Hemisphere using Geodetic and Astrometric Observations

by Sayan BASU

The present International Celestial Reference Frame (ICRF), the ICRF-3 is based on a catalogue of 4536 quasar positions obtained from Very Long Baseline Interferometry (VLBI) radio measurements. This radio frame is crucial for many applications, from measurements of Earth's orientation in space to spacecraft navigation and measurements of sea-level rise. However, the deficit in ICRF source density in the South and lack of dedicated imaging campaigns in the South, to monitor structural changes, remain a big concern. These ICRF sources can exhibit spatially extended emission structures that can have a significant effect on astrometric VLBI measurements. The Celestial Reference Frame Deep South (CRDS) is a dedicated astrometric VLBI programme to observe Southern ICRF sources on a regular basis. In an effort to improve the situation in the South, these CRDS sessions have recently been optimized for VLBI imaging. In this thesis, I present VLBI images and source structure analysis results for southern ICRF sources observed in four of these CRDS sessions. For some of these sources, I present the very first high-resolution radio images. I also present results from source structure analysis and a corresponding assessment of astrometric quality, and I also present results from efforts to increase the ICRF source density in the South.

Key words: techniques: interferometric - astrometry — galaxies: active — quasars: general — radio continuum: galaxies — reference systems — surveys.

Acknowledgements

Firstly, I would like to thank my supervisor, Prof Lerothodi Leeuw, of the University of South Africa. He has been supportive and helpful throughout my research. I am thankful to him for providing me with the National Research Foundation (NRF) grant-holder bursary to carry out my PhD studies.

I would like to take this opportunity to express my sincere gratitude to my co-supervisors, Dr Aletha de Witt and Dr Jonathan Quick, of the Hartebeesthoek Radio Astronomy Observatory (HartRAO). It was the most exciting period of my life, like being on a roller coaster, and Dr Aletha de Witt and Dr Jonathan Quick made sure my focus was always on track throughout it. Without their tremendous support, it would never have been possible to finish this research work in time. I am indebted to Dr de Witt for her enthusiasm and passion that kept me inspired to carry on the research and to contribute to the VLBI working group globally. Dr de Witt, especially, was so understanding and considerate when I needed a break during my toughest time.

I thank the de Witt family for being supportive. I always felt as if I was not so very far away from my home in India. Their affection and wishes made my research and social life comfortable which ultimately contributed to my work.

My sincere thanks to the late Dr Michael Gaylard and also to Prof. Ludwig Combrinck, the former directors of the HartRAO facility, as well as to Dr Justin Jonas and Dr Rob Adam of the South African Radio Astronomy Observatory (SARAO) for providing the financial support to complete this research. I would like to thank Mrs Glenda Coetzer for giving me permission to have access to the HartRAO library and for allowing me to keep some reference books for the literature review. I am grateful to Dr Michael Bietenholz for his critical reviews of this thesis and useful comments and suggestions.

I am thankful to Mrs Marisa Nickola and the other VLBI operators, Mr Jacques Grobler, Mr Pieter Stronkhorst, Mr Philip Mey and Mr Ronnie Myataza for taking care of the VLBI observations that I have used in my research. All the staff members at the HartRAO facility contributed to my research, directly and indirectly, making me a good researcher and a better person. I would like to thank my fellow students. It was a great experience sharing office space with all of you during the last five years. I personally would like to thank my friends, Mr Arvind Ramessur and Mr Mekuanint Kifle, with whom I spent most of the time.

I am thankful to my collaborators, Dr Stanislav Shabala, Dr Lucia Plank and Dr Jamie McCallum, at the University of Tasmania (UTAS), for their suggestions and

inputs to the research work. My sincere thanks to Dr Alan Fey of the United States Naval Observatory (USNO), the principal investigator of the Celestial Reference Frame Deep South VLBI experiment, for allowing me to use the data for this research. I would like to thank Dr Alessandra Bertarini of the Institute for Geodesy and Geoinformation (IGG) / Max Plank Institute for Radio Astronomy (MPIfR), for her efforts in providing me with the requested data on time.

Finally, last but by no means least, I am grateful to my parents and family who have provided me throughout my life with moral, emotional and intellectual support.

Contents

Declaration of Authorship	i
Abstract	iii
Acknowledgements	iv
Contents	vi
List of Figures	viii
List of Tables	ix
Abbreviations	x
1 Introduction	1
2 Background Study	4
2.1 Interferometry: A short introduction	5
2.1.1 Two-element interferometer	5
2.1.2 VLBI	7
2.1.3 The visibility and Fourier transform relation	8
2.1.3.1 Sampling visibilities and image reconstruction	10
2.2 Calibrator sources for astronomy	12
2.3 Reference sources for geodesy	13
2.4 ICRF	14
2.5 AGN as ICRF sources	18
2.6 Importance of imaging and monitoring the intrinsic structure of ICRF sources	18
2.6.1 VLBI imaging using geodetic and astrometric observations	20
2.7 Source structure in VLBI	22
2.7.1 Source structure indicators in VLBI	24
2.7.1.1 Source structure index	24
2.7.1.2 Source compactness	26
2.7.1.3 Radial extent	26
2.7.1.4 Modulation index	27

3	Observations and Data Reduction	28
3.1	Sources observed in the CRDS sessions	31
3.2	Selected CRDS sessions	35
3.2.1	The CRDS-63 session	35
3.2.2	The CRDS-66 session	36
3.2.3	The CRDS-68 session	37
3.2.4	The CRDS-94 session	37
3.3	Conversion of the data to FITS file	38
3.4	Data reduction	39
3.4.1	Fringe fitting: delay, rate and phase calibration	41
3.4.2	Imaging	42
3.4.3	Model fitting	42
4	Results and Discussion	45
4.1	Astrometric quality assessment of the sources	45
4.1.1	The CRDS-63 session	45
4.1.2	The CRDS-66 session	47
4.1.3	The CRDS-68 session	48
4.1.4	The CRDS-94 session	49
4.2	Spectral index distribution	61
4.3	Modulation index	61
4.4	VLBI contour maps of the sources	65
4.4.1	Contour maps	65
4.5	Discussion	96
5	Conclusion	131
6	Future Work	136
6.1	Continuous VLBI imaging	136
6.2	Investigating source structure in VGOS observations	137
6.3	Effects of source structure on station position estimation	137
6.4	Core-shift effect	138
6.5	ICRF- <i>Gaia</i> transfer sources in the CRDS sessions	138
	Bibliography	140

List of Figures

2.1	Schematic diagram of a two-element interferometer	6
2.2	Earth-rotation aperture synthesis	9
2.3	Visibility function of various source models	10
2.4	An image from sampled visibilities	12
2.5	ICRF source distribution	16
2.6	Source structure in ICRF source-2	19
2.7	Source structure in ICRF source-1	19
2.8	Source Structure in ICRF source-3	20
2.9	Dual-frequency VLBI image of the source J0217+7349	21
2.10	Source structure correction plots	24
2.11	VLBI image and structure correction map of an ICRF source	26
3.1	Telescope locations in the CRDS sessions	30
3.2	The (u,v) -coverage in the CRDS-63 session	36
3.3	An improved visibility map in the CRDS session	39
4.1	Histogram plots of the CRDS-63 session analysis	46
4.2	Histogram plots of the CRDS-66 session analysis	47
4.3	Histogram plots from the CRDS-68 session analysis	48
4.4	Histogram plots from the CRDS-94 session analysis	50
4.5	Spectral index distribution	61
4.6	Modulation index distribution	62
4.7	Contour maps of the ICRF sources	66
5.1	Comparison of the contour map - Source J0538-4405	132
5.2	Comparison of the contour map - Source J0922-3959	133
5.3	Comparison of the contour map - Source J1147-3812	133
6.1	Effects of the source structure on the station coordinates	137

List of Tables

2.1	Angular resolution of different radio telescopes	5
2.2	List of ICRF catalogues	16
2.3	A comparison between the ICRF-2 and ICRF-3 showing the number of the sources in the sky based on source declination range.	17
3.1	Statistics of IVS programmes in the South in 2013	29
3.2	List of the CRDS sessions	32
3.3	List of sources with coordinates observed in the CRDS sessions	32
3.4	SEFD and T_{sys} of the telescopes	40
4.1	Astrometric quality of the sources from the CRDS-63 session	46
4.2	The CRDS-66 session astrometric quality analysis	47
4.3	Astrometric quality of the sources from the CRDS-68 session	48
4.4	Astrometric quality assessment of the CRDS-94 session	49
4.5	CRDS imaging results	51
4.6	Modulation index results	62

Abbreviations

AGN	A ctive G alactic N uclei
AIPS	A stronomical I mage P rocessing S ystem
BVID	B ordeaux V LBI I mage D atabase
CDDIS	C rustal D ynamics D ata I nformation S ystem
CDP	C rustal D ynamics P roject
CRDS	C elestial R eference F rame D eep S outh
CRF	C elestial R eference F rame
DBBC	D igital B aseband C onverter
DORIS	D oppler O rbital R adiography and R adiopositioning I ntegrated by S atellite
DOY	D ay O f Y ear
DPFU	D egree P er F lux U nit
FAST	F ive-hundred-meter A perture S pherical radio T elescope
FITS	F lexible I mage T ransport S ystem
FWHM	F ull W idth H alf M aximum
GAIA	G lobal A strometric I nterferometer for A strophysics
GBT	G reen B ank T elescope
GPS	G lobal P ositioning S ystem
GSFC	G oddard S pace F light C enter
HOPS	H aystack O bservatory P ost-processing S ystem
HST	H ubble S pace T elescope
IAU	I nternational A stronomical U nion
ICRF	I nternational C elestial R eference F rame
ICRS	I nternational C elestial R eference S ystem
IERS	I nternational E arth R otation and R eference S ystem S ervice
IF	I ntermediate F requency

ITRF	I nternational T errestrial R eference F rame
IVS	I nternational V LBI S ervice for Geodesy and Astrometry
LAB	L aboratoire d' A strophysique de B ordeaux
LBA	A ustralian L ong B aseline A rray
LCS	L BA C alibrator S urvey
NASA	N ational A eronautics and S pace A dministration
NED	N ASA/ I PAC E xtragalactic D atabase
NRAO	N ational R adio A stronomy O bservatory
RCP	R ight C ircular P olarization
RDV	R esearch and D evelopment V LBI P rogramme
RFC	R adio F undamental C atalogue
RMS	R oot M ean S quare
RRFID	R adio R eference F rame I mage D atabase
SC	S ource C ompactness
SEFD	S ystem E quivalent F lux D ensity
SHAO	S Hanghai A stronomical O bservatory
SI	S tructure I ndex
SLR	S atellite L aser R anging
SNR	S ignal to N oise R atio
SOAP	S Outhern A strometry P roject
TRF	T errestrial R eference F rame
USNO	U nited S tates N aval O bservatory
UT	U niversal T ime
VCS	V LBA C alibrator S urvey
VGOS	V LBI G lobal O bserving S ystem
VLBA	V ery L ong B aseline A rray
VLBI	V ery L ong B aseline I nterferometry
WACO	W ashington C orrelator

*Dedicated to my parents
and
the de Witt family for their unconditional love and support*

Chapter 1

Introduction

The International Celestial Reference Frame (ICRF) is based on high precision geodetic and astrometric Very Long Baseline Interferometric (VLBI) measurements of positions of extragalactic radio sources at 2.3 (S-band) and 8.4 GHz (X-band). VLBI observations of these sources are used in many applications, for example, the realization of the International Terrestrial Reference Frame (ITRF), calculating the orientation of the Earth in space, providing calibrator sources for parallax measurements, as well as for imaging faint sources in astronomy, studying the motion of tectonic plates, measurements of the sea level rise and spacecraft navigation, to name but a few. The ICRF also contributes to realizing a Global Geodetic Reference Frame (GGRF) for sustainable development, a resolution adopted by the United Nations in 2015.

It is a well-known fact that radio celestial reference frames (CRFs), including the ICRF, have always been weaker in the South than the North in terms of the source distribution. The smaller number of telescopes, and observing sessions in the Southern Hemisphere, have always resulted in catalogues of radio sources being weaker below a declination of -30° , in both density and precision. Although the present radio reference frame, the ICRF-3, provides a major improvement in the source density and precision of the ICRF in the South, parity between the North and South has not yet been reached and much work remains to be done.

The extragalactic radio sources making up the ICRF are mostly quasars, the most luminous and powerful of all active galactic nuclei (AGN). Quasars, being very distant objects, show no discernible proper motion on the sky, and on VLBI scales they appear as compact or core-dominated with a point-like structure. However, many of the extragalactic radio sources that make up the ICRF exhibit spatially extended intrinsic

structures on milliarcsecond (mas) scales. The extended emission structures in these sources may vary with time, frequency, and baseline projection. It is well-known that the effect of source structure on astrometric VLBI positions can be significant. For this reason, VLBI images of ICRF sources from multiple epochs are used to map and monitor the source structure on a regular basis.

Unlike the North, imaging and source structure analysis of the ICRF sources have not been done extensively in the South. For this purpose, I have selected an existing and ongoing geodetic and astrometric VLBI experiment in the South which proved to be suitable for imaging purposes. I have selected three sessions from 2013 and one session from 2018 for this purpose. A total of 103 sources were observed in these four sessions. Among the 103 sources, 76 sources were ICRF-2 defining sources that were regularly observed in these sessions. The remainder of the sources was added to the 2018 session as they were potential candidates for the ICRF-3 defining sources at the time. The defining sources in the ICRF are crucial because their source positions are used to maintain the axis stability of the frame. I present VLBI images and source structure analysis for 90 sources, out of the total of 103 sources that were observed. Due to insufficient data (only 2 or 3 telescopes participated) from some observing sessions, imaging was not possible for 13 of the sources. For the 90 sources for which imaging was possible, 31 sources were imaged for the first time at S- and X-band. The VLBI images from this work were used to select defining sources for the ICRF-3 in the South.

The thesis is divided into 5 chapters after this introductory chapter:

- Chapter 2 provides the background information and the problem statement. In this chapter, the basic principles of the interferometric technique and VLBI are discussed. Following this, the properties and physical characteristics of radio reference sources are discussed. The effects of radio source structure on geodetic VLBI observations are discussed, and I provide metrics that can be used to evaluate the astrometric quality of the sources. The chapter concludes with a discussion on the importance of VLBI imaging of reference sources.
- In Chapter 3, the observations and data reduction methods are discussed. I firstly present the details of the VLBI sessions used for this study and a list of the sources observed in these sessions and their physical properties. This is followed by a detailed discussion of the data reduction, imaging and model-fitting methods that were used.
- The results and a discussion of the results are presented in Chapter 4. Session-by-session results are discussed, followed by the epoch-based VLBI images of the

sources at both S- and X-bands. The chapter concludes with a discussion of individual sources.

- In Chapter 5, I summarise the main results and conclusions of this study.
- Chapter 6 outlines the possible future work that can be accomplished using the existing imaging results from this study as well as from the continued imaging of these sessions.

Chapter 2

Background Study

The angular resolution of any parabolic reflector, such as a radio telescope dish, depends on the diameter of the dish as well as on the frequency of observation. From diffraction theory, the angular resolution (θ) of a radio telescope is

$$\theta = 1.22 \frac{\lambda}{D}, \quad (2.1)$$

where the factor 1.22 is derived from the calculation of the position of the first dark circular region of the Airy disc of the diffraction pattern, λ is the wavelength of radiation received and D is the diameter of the dish. It should be noted that Equation 2.1 is only for a dish with uniform illumination. The angular resolution is the smallest angular separation between two point sources that can be distinguished as individual objects. The angular resolution of a telescope is inversely proportional to the telescope diameter. For a given wavelength, smaller resolutions require larger telescopes.

For example, the *Hubble Space Telescope (HST)* with a diameter $D = 2.4$ m gives an angular resolution $\theta = 0.1$ arcsec at a wavelength $\lambda = 9537\text{\AA}$ ¹. To achieve the same angular resolution at a wavelength of $\lambda = 5$ cm, a radio telescope of diameter $D = 125$ km is required. At present, the Green Bank Telescope (GBT) in West Virginia, US, with a diameter of 100 m is the world's largest fully steerable single-dish radio telescope. The Five-hundred-meter Aperture Spherical radio Telescope (FAST) in Guizhou, China, is the largest filled-aperture radio telescope in the world. Although the FAST telescope has a reflector diameter of 500 m, the effective illuminated diameter is only 300 m.

Some examples of the angular resolution obtained by single-dish radio telescopes with different diameters at a wavelength of 5 cm are given in Table 2.1.

¹1 Å is equivalent to 10^{-8} cm

TABLE 2.1: The angular resolution obtained by four radio telescopes with different diameters at a wavelength of 5 cm.

Telescope	Diameter (meter)	Angular resolution (arcmin)
Parkes	64	3.27
GBT	100	2.09
Arecibo	306	0.68
FAST	300	0.69

2.1 Interferometry: A short introduction

2.1.1 Two-element interferometer

The Michelson experiment (Michelson, 1890, 1920) showed that a resolving power of $\theta \simeq \lambda/b$ can be achieved by combining two reflectors with diameter $D \ll b$, where b is the separation between reflectors in a two-slit optical interferometer. Applying this concept, Ryle & Vonberg (1946) first built a two-element radio telescope in Cambridge, England, with a distance of approximately 0.5 km between the two telescopes to measure the diameter of the Sun.

The response of a two-element interferometer can be compared to Young's double-slit experiment with each radio telescope to be considered as a slit. A diagram of a two-element interferometer, where two identical telescopes are separated by a distance b , is shown in Figure 2.1. The telescopes are connected by cables. Both telescopes are pointing to the same distant point source, where \hat{s} is the unit vector in the direction of the source and \vec{b} is the baseline vector from telescope 1 to telescope 2. Both telescopes are operating at a frequency, ν . The angle between the direction to the point source and the normal to the telescope separation vector \vec{b} , is θ . A plane wave arriving from the point source in direction \hat{s} , will arrive first at telescope 2 and some time later at telescope 1. The geometric delay $\tau_g = \vec{b} \cdot \hat{s}/c$ is the difference between the arrival times of the observed signal at telescopes 1 and 2. The voltages V_1 and V_2 are induced at the focus of telescopes 1 and 2, respectively, and are proportional to the electric field at time t . The voltage at telescope 2 is $V_2 = V \cos(\omega t)$ where $\omega = 2\pi\nu$. Because of the geometric delay τ_g , the induced voltage at telescope 1 is $V_1 = V \cos[\omega(t - \tau_g)]$. The incoming wavefront arrives at each telescope at a different phase, causing interference fringes, similar to Young's double-slit experiment. These voltages are then multiplied

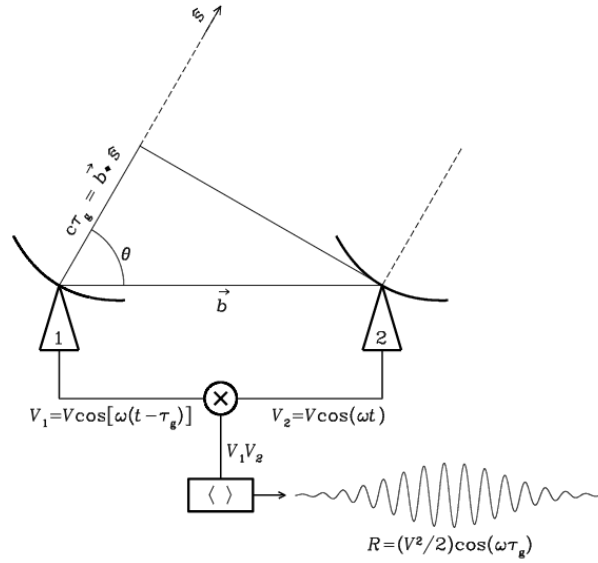


FIGURE 2.1: Schematic diagram of a two-element interferometer. Telescopes 1 and 2 are separated by a baseline vector \vec{b} and are observing a source in direction \hat{s} at frequency ν . The output voltage V_1 of telescope 1 is the same as the output voltage V_2 of telescope 2 but lags by a geometric delay $\tau_g = \vec{b} \cdot \hat{s} / c$. At the correlator, these voltages are input to a multiplier (' \otimes ' sign) and then time-averaged to get an output response of amplitude R . It is proportional to the flux density, and its phase is delay- and frequency-dependent. The output fringe that is shown occurs if the source direction in the interferometer frame changes at a constant rate of $d\theta/dt$. Image credit: [NRAO \(2018\)](#)

and time-averaged by the correlator. The product of the multiplication of V_1 and V_2 is

$$V_1 V_2 = \left(\frac{V^2}{2} \right) [\cos(2\omega t - \omega\tau_g) + \cos(\omega\tau_g)]. \quad (2.2)$$

The output amplitude $V^2/2$ in Equation 2.2 is proportional to the flux density of the point-source, multiplied by square root of the effective collecting areas of the two telescopes. The output R which is the time average of $V_1 V_2$, is

$$R = \langle V_1 V_2 \rangle = \left(\frac{V^2}{2} \right) \cos(\omega\tau_g). \quad (2.3)$$

In Equation 2.3, the time average is long enough to remove the high-frequency term $\cos(2\omega t - \omega\tau_g)$ from the output R . The correlator output voltage R changes sinusoidally with source direction in the interferometer frame. These sinusoids are called fringes and the fringe phase is

$$\phi = \omega\tau_g = \frac{\omega}{c} b \cos \theta \quad (2.4)$$

and changes with θ as $d\phi/d\theta = 2\pi(b \sin \theta / \lambda)$. The fringe phase ϕ (Equation 2.4) is sensitive to source position, where an angular displacement in the source produces a corresponding displacement in the fringe pattern.

The resolution of a two-element interferometer is $\sim \lambda/b$ radians, and a higher resolution is achieved by increasing the distance between the telescopes (or observing at higher frequencies). Two element interferometers can not distinguish between sources that are small compared to the fringe spacing and all such sources will appear as point sources. The minimum source size that can be resolved by an interferometer is given by

$$\theta \lesssim \frac{\lambda}{b}, \quad (2.5)$$

the resolution of the interferometer. On the other hand, the fringe amplitude of an extended source will be less than the fringe amplitude of a point source with the same total flux, and the more extended the source, the lower the fringe amplitude will become. For a sufficiently extended source, the interferometer will resolve out the source, and the fringe amplitude will become zero.

We can consider an extended source with source brightness distribution I , as a sequence of point sources each of which emits radiation uncorrelated with the emission from the others. The source brightness distribution can be written as the sum of its even and odd parts. The cosine function in Equation 2.3 is sensitive to the even part of I . To recover the odd part of I a sine correlator is needed with an output $R_s = (V^2/2) \sin(\omega\tau_g)$, where a 90° phase delay is inserted into the output of one telescope as $\sin(\omega\tau_g) = \cos(\omega\tau_g - \pi/2)$. The combination of cosine and sine correlators (R and R_s , respectively) is called a complex correlator because the correlator outputs are a complex number combining the amplitude and phase of the signal.

A two-element interferometer provides limited information about the source structure unless the telescopes are moved to change the baseline length and the observations are repeated. However, this situation can be improved by using an array of telescopes distributed in different directions and at different distances.

2.1.2 VLBI

When radio telescopes in an interferometer are separated by long baselines, the observables are no longer obtained in real-time but are generated at a correlator center, where the signals from individual telescopes are multiplied together in baseline pairs. An interferometer array with N number of telescopes provides $N(N - 1)/2$ pairs of telescopes and thus $N(N - 1)/2$ baselines. In this case of VLBI, the telescopes in an array can be separated across continents, and even further, to form an interferometer where telescopes are not physically connected to each other. At each participating station, there is a very stable frequency standard (typically a hydrogen maser) that provides a reference signal to enable very accurate time tagging of the signals as they

are being recorded at each of the telescopes. The time-tagged recorded data from each telescope during an experiment are shipped to a correlator center, where signals are played back and complex cross-correlated to obtain the observables for astronomical and geodetic purposes. The complex output of the correlator, when scaled for telescope sensitivities, is called the visibility function $V^t(u, v)$ and is the Fourier transform of the source brightness distribution $I(l, m)$.

2.1.3 The visibility and Fourier transform relation

The baseline vector \vec{b} is specified by the coordinate system (u, v, w) where u, v and w are in units of wavelength. The coordinates u and v form a plane with u oriented towards the East and v oriented towards the North. This plane is known as the (u, v) -plane and is perpendicular to the source direction. The direction of w is chosen to be in the direction of the source and normal to the (u, v) -plane. Each point in the (u, v) -plane defines a specific baseline length and orientation that corresponds to one Fourier component of the source brightness distribution.

In interferometry, the technique of aperture synthesis is used to synthesize a large telescope by combining the signals from smaller telescopes together. Aperture synthesis depends strongly on the geographical location and spacing of the telescopes and the corresponding orientation of the projected baselines from the pairs of telescopes within an array. The projected baseline coverage of the interferometer also changes with the rotation of the Earth. As the Earth rotates, the orientation of the baseline vector changes, which traces part of an ellipse in the (u, v) -plane. The superposition of all the ellipses from all the baselines in a specific array is called the (u, v) -coverage. Perfect reconstruction of the brightness distribution can only be achieved if all the points in the (u, v) -plane are measured. Interferometer baselines in an east-west direction will remain in a single plane perpendicular to the north-south rotation axis of the Earth. If the number of spacings in an interferometer is such to cover all baselines out to some maximum then we will have a synthesized fully filled aperture.

Figure 2.2 represents the aperture synthesis of an interferometer consisting of 8 telescopes. The figure on the left shows the telescope locations, the middle figure shows the corresponding u, v points for a snapshot observation at a time t at an hour angle of zero, and the figure on the right shows the corresponding (u, v) -coverage over a 12-hour integration. During the 12-hour period, each of the projected baselines traces an ellipse in the (u, v) -plane. In the figure, u is the east-west component and v is the north-south component of the projected baselines.

By the Van Cittert-Zernicke theorem, the Fourier transform of the source brightness distribution is known as the visibility function V^t . In this case, the visibility function is

$$V^t(u, v) = \text{FT}[I(l, m)], \quad (2.6)$$

where FT is the Fourier transform, (l, m) are coordinates in the tangent plane of the sky, and u, v are the two components of the baseline vector. As the sky brightness distribution is real, its Fourier transform (i.e., the visibility function) must be Hermitian, with $V^t(-u, -v)$ equal to the complex conjugate of $V^t(u, v)$. After 12 hours of observing, no new information is obtained, as each pair of telescopes sample the (u, v) -plane at both u, v and $-u, -v$. The unit vector \hat{s} in Figure 2.1 points to the nominal position of the source on the sky and defines the w -direction. The source is assumed to be located infinitely far away and therefore \hat{s} is the same for all telescopes regardless of location.

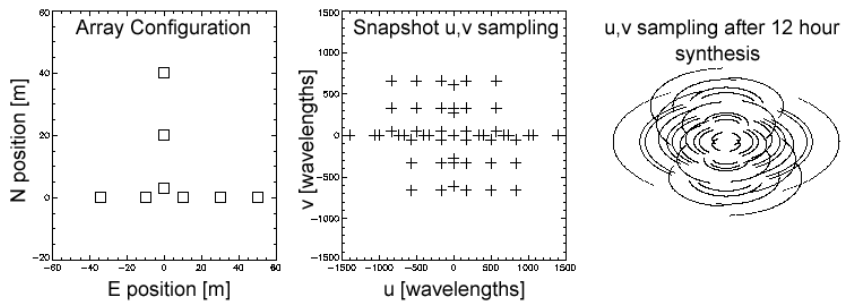


FIGURE 2.2: *Left*: An interferometer array of 8 telescopes, with telescope locations in meters towards the East (E) and North (N) respectively. *Middle*: The (u, v) -sampling from the array for a single time, at zero hour angle. Each cross represents a different baseline, and for this array there are $N(N - 1)/2 = 28$ baselines. In the figure, the Earth rotates counterclockwise with a period of one sidereal day. North (v) is up and East (u) is to the left. *Right*: The (u, v) -sampling after a 12-hour integration. During the 12-hour period, the projected baseline traces an ellipse in the (u, v) -plane. Image credit: Gary (2018)

It is important to know how the visibility function for various source brightness distributions behave as a function of increasing baseline length or (u, v) -distance. Figure 2.3 shows the visibility functions of a point source, an extended source, a point double source and an extended double source with the visibility amplitude and phase as functions of (u, v) -distance. A point source close to the phase-centre has a stable visibility amplitude over all the observed baselines. For any specific array, if a source has constant amplitude over all the baselines, then the source is called a point-like or compact source (Figure 2.3 (i)). A source consisting of two point sources has a visibility that is the sum of the two-point source functions (Figure 2.3 (iii)). The visibility amplitude changes sinusoidally and is inversely proportional to the separation between two point sources. An extended source will be resolved on long baselines (Figure 2.3 (ii)).

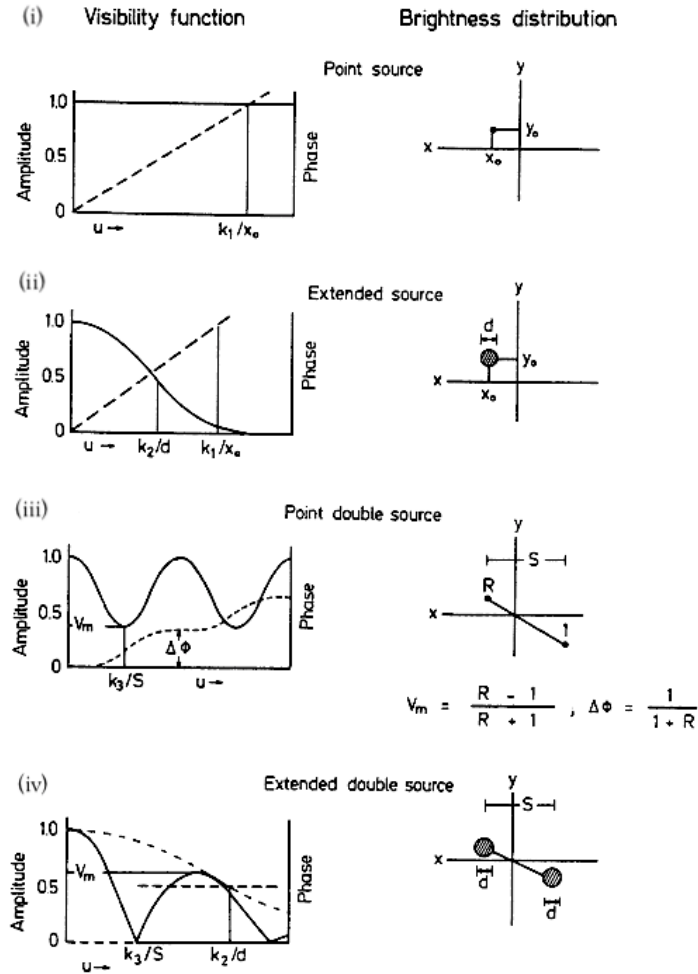


FIGURE 2.3: The visibility functions of the brightness distribution of various source models. The amplitude and phases are represented by the solid and dashed lines, respectively. (i) A point source model. The visibility amplitude and phase do not show any fluctuation. The visibility amplitude remains stable with a change in the (u, v) -distance. (ii) An extended source with a circular Gaussian brightness distribution. The visibility amplitude drops with an increase in (u, v) -distance. (iii) A double point source. The visibility amplitude and phase depend on the separation between the sources. (iv) An extended double source. The final visibility distribution is obtained after multiplication by the visibility function of each source. Adapted from [Fomalont & Wright \(1974\)](#).

2.1.3.1 Sampling visibilities and image reconstruction

An interferometer usually only samples a limited set of points in the (u, v) -plane, making it more difficult to reconstruct a reasonable estimate of the source brightness distribution. This measured set of points or sampling of the (u, v) -plane can be described by the sampling function $S(u, v)$. The measured visibility function $V^m(u, v)$ is only a sample of the true visibility $S(u, v)V^t(u, v)$ and is the actual data provided by the array. By Fourier transforming the sampled visibility function, we recover a “dirty image”

$I^D(l, m)$, where

$$I^D(l, m) = \text{FT}[S(u, v)V^t(u, v)]. \quad (2.7)$$

The dirty image contains only the sampled visibilities and not complete information about the sky brightness distribution. Therefore, some image reconstruction technique should be used to recover the missing spacings. Applying the convolution theorem, it is shown that

$$I^D(l, m) = S(u, v) * V^t(u, v), \quad (2.8)$$

where the symbol $*$ denotes convolution. Equation 2.8 can be interpreted as the Fourier transform of $S(u, v)$ convolved with $V^t(u, v)$. The inverse Fourier transform of the sampling function $S(u, v)$ is called the “dirty” or synthesized beam $B(l, m)$, also called the point-spread function and is

$$B(l, m) = \text{FT}^{-1}[S(u, v)], \quad (2.9)$$

where FT^{-1} is the inverse Fourier transform. The sampling function $S(u, v)$ has a value of 1 where we have measured data, and 0 elsewhere.

A “dirty image” is not the true image of the sky but the convolution of the true image $I(l, m)$ and the dirty beam $B(l, m)$. Figure 2.4 demonstrates the relationship between the sky plane (l, m) representations of the true image, dirty beam and the dirty image (upper panel) and the corresponding (u, v) -plane representations of the true visibility, the sampling function and the sampled visibility (lower panel). The actual measurements from the array are shown in the panel (vi) and the actual image of the source from the array, is shown in the panel (iii). Special image reconstruction techniques are used to predict the missing visibilities in the panel (iv) to arrive at the true map in the panel (i).

To produce an approximation of the true image of an observed source, a deconvolution method, such as the CLEAN algorithm (Högbom, 1974) is used. In this algorithm, the sky is assumed to be composed of a small number of point sources. The CLEAN algorithm is an iterative algorithm that (1) finds the position and strength of the brightest point in the dirty image, (2) subtracts the dirty beam convolved by the strength of the brightest source (and additionally the loop gain) from the dirty image at the position of the brightest point, (3) goes back to (1) unless any remaining peak is below the user-specified threshold, (4) convolves the accumulated point source model with an idealised CLEAN beam, and (5) adds the residuals from the dirty image (3) to the CLEAN image.

For a more detailed introduction to interferometry, interested readers are referred to Steel (1967); Thompson (1989); Taylor et al. (1999); Thompson et al. (2001).

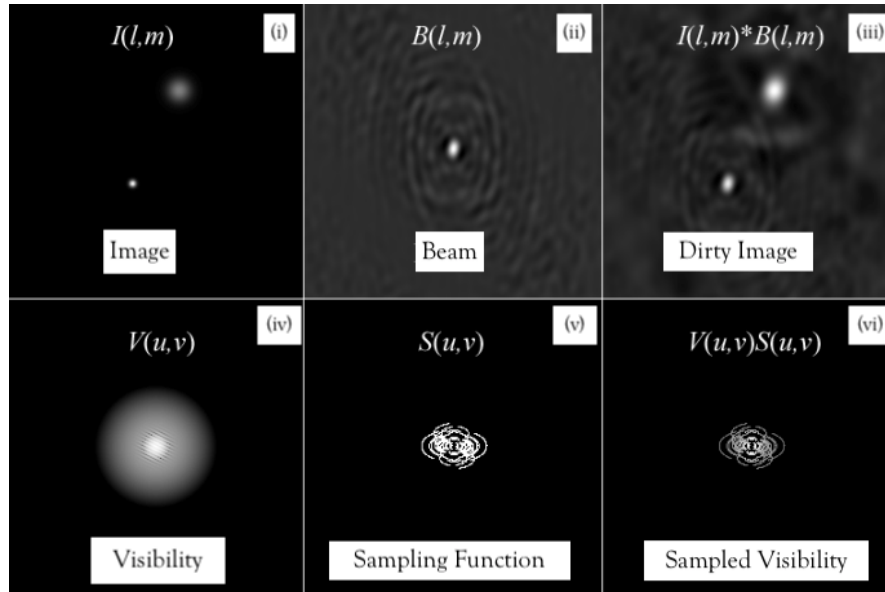


FIGURE 2.4: An example of (i) the true image and (iv) the corresponding true visibility, (iii) the dirty beam and (v) the sampling function of the array whose Fourier transform gives the dirty beam (ii). The product of (iv) and (v) gives the sampled visibility (vi). The dirty image (iii) is from the Fourier transform of the sampled visibilities. Image credit: Gary (2018).

2.2 Calibrator sources for astronomy

Extragalactic radio sources with point-like or compact structure and accurately known positions are considered as reference or calibrator sources. Calibrator sources are used to correct delay and rate residuals due to the correlator model errors. Because of their stable amplitude and phase, calibrator sources are observed along with a weak target source in phase referenced observations. In this case, fringe-fit solutions from the calibrator source are used to correct delay, rate and phase residuals of the target source.

A radio source position can be obtained accurately when it is measured with respect to a calibrator typically few degrees away (Fomalont, 1995). The accuracy of the source position is then dependent on the quality of the calibrator source as well as on the associated errors between the source and calibrator. The relative position can be used to measure the proper motion, parallax, and orbital trajectory of a radio source.

The characteristics of a source to be considered as a calibrator source are the following:

- The source should be strong so that it can be detected with a good Signal to Noise Ratio (SNR) on all baselines within the coherence time.
- The source should be compact on all baselines. For VLBI this implies that the source is compact on mas scales.

- The source position should be accurately known.

2.3 Reference sources for geodesy

The International VLBI Service for Geodesy and Astrometry (IVS; [Schuh & Behrend, 2012](#)) conducts geodetic and astrometric VLBI observations using telescopes distributed around the globe to provide a number of products. These products are updated frequently through continuous VLBI monitoring programmes. The three main products of geodetic and astrometric VLBI observations are CRF, the Terrestrial Reference Frame (TRF) , and the Earth Orientation Parameters (EOP).

- **CRF**

Astrometric VLBI observations of extragalactic radio sources are used to define and maintain a CRF centered at the barycenter of the Solar System. Extragalactic radio sources, such as quasars, are very distant objects that do not show any proper motion on the sky and therefore provide a grid of stationary reference objects on the sky. The coordinates of more than 4,000 extragalactic radio sources have been used in the current realization of the ICRF, described in more detail in [Section 2.4](#).

- **TRF**

A TRF is a reference system that co-rotates with the Earth in its daily motion in space. In such a reference system, the coordinates of points are attached to the Earth's solid surface and show variations with time, due to geographical effects such as tectonic or tidal deformations. The ITRF is based on data from four different techniques namely geodetic VLBI, Satellite Laser Ranging (SLR), Global Positioning System (GPS), and Doppler Orbitography and Radiopositioning Integrated by Satellite (DORIS). Geodetic VLBI observations of reference sources are used for the VLBI component and also provide the scale of the ITRF. The present realization of the ITRF, ITRF2014 consists of positions and velocities of 1499 stations located in 975 cities ([Altamimi et al., 2016](#)). The ITRF is used in high precision positioning applications such as GPS and measuring continental and inter-continental tectonic plate movements.

- **EOP**

The Earth's precession and nutation (changes in the Earth's tilt relative to its orbit), Earth's rotation (changes in the universal time (UT), UT1, with respect to

high precision atomic clock time), and polar motion (movements of Earth's celestial poles) are referred to as EOP. Geodetic VLBI observations of radio reference sources allow the monitoring of the full set of EOP and are unique in its ability to measure UT1 (e.g. [Schuh & Behrend, 2012](#)). The orientation of the Earth in inertial space is important in determining satellite orbits accurately and is crucial for positioning and navigation on Earth and in space. The IVS coordinates geodetic VLBI observations of reference sources through sessions designed specifically for the monitoring of EOP.

2.4 ICRF

For decades the CRFs have been used for navigation, and for studying the dynamics of the Solar System. Before the 1980s, optical reference frames were used for such purposes with an accuracy roughly of 0.1 arcsec ([Ma et al., 1998](#)). Optical reference frames are time-dependent as stars show detectable motions and for astrometric purposes, such frames must specify the positions, an epoch and predicted stellar motions. On the other hand, extragalactic radio sources being very distant objects, show very little or non-detectable motion on the sky. The International Astronomical Union (IAU) in its 1991 recommendations on reference systems decided to use extragalactic radio sources as the basis of its new International Celestial Reference System (ICRS; [Bergeron, 1992](#); [Guinot, 1979](#); [Kovalevsky & Feissel, 1996](#); [Gontier et al., 2006](#)). The ICRF was adopted by the IAU and became the fundamental CRF as of 1 January 1998, replacing the FK5 optical frame ([Ma et al., 1998](#)). The ICRF is defined by radio positions of extragalactic radio reference sources and uses the VLBI technique to maintain and improve its accuracy.

Geodetic and astrometric VLBI observations at S-band (2.3 GHz) and X-band (8.4 GHz) are used for the realization of the ICRF and have been conducted since mid-1979. Since 1999 these observations have been coordinated by the IVS ([Fey et al., 2015](#)). The dual-frequency S/X-band observations are used to calibrate the frequency-dependent propagation delay caused by the ionosphere. To define the first realisation of the ICRF (ICRF-1), geodetic and astrometric VLBI data between August 1979 and July 1995 were used and the frame contained 608 radio source positions ([Ma et al., 1998](#)). In the ICRF-Ext.1 ([Gontier et al., 2002](#)) and ICRF-Ext.2 ([Fey et al., 2004](#)) a total of 109 sources were added using new VLBI data including the first series of the Very Long Baseline Array (VLBA) Calibrator Survey (VCS) ([Beasley et al., 2002](#)) that increased the number of radio sources to 717. The ICRF-1 had an estimated noise floor of $250 \mu\text{as}$ and an axis stability of $\sim 20 \mu\text{as}$ ([Fey et al., 2015](#)). The second realization of the ICRF,

the ICRF-2 (Fey et al., 2015) was constructed by using nearly 30 years of geodetic and astrometric VLBI data between August 1979 and March 2009. The number of sources was increased by a factor 5 compared to the ICRF-1. The ICRF-2 contained radio source positions of 3,414 extragalactic radio sources, and it had an estimated noise floor and axis stability of $40 \mu\text{as}$ and $\sim 10 \mu\text{as}$ respectively (Fey et al., 2015). In 2018, the IAU adopted the third realization of the ICRF and as of 1 January 2019, the ICRF-3 (Jacobs et al., 2018) became the official fundamental CRF. The addition of more than 1,000 extragalactic radio sources increased the number of sources in the ICRF-3 to 4,536. Geodetic and astrometric VLBI observations used in the ICRF-3 have been conducted between August 1979 and December 2017. The ICRF-3 has an estimated noise floor of $\sim 30 \mu\text{as}$ and estimated axis stability of $\leq 10 \mu\text{as}$ (Gordon, 2019). The ICRF-3 is also unique in providing catalogues at higher radio frequencies for the first time. The 24 GHz (K-band, de Witt et al., 2019b) VLBI observations between 2002 and 2017 and the 43 GHz (Ka-band) VLBI observations between 2012 and 2017 were used to extend the ICRF-3 to higher radio frequencies.

Since 1998, the ICRF has been elaborated by including more radio sources in order to densify the frame. The main objectives of the extensions of the ICRF are:

- To provide positions of extragalactic radio sources that are being observed since July 1995.
- To improve the positions of the candidate sources using observations.
- To monitor sources to analyse their suitability for the ICRF use.
- To improve the data analysis.

The radio reference sources in the ICRF catalogues are divided into three categories:

- The most compact sources with accurate and reliable positions are called *defining* sources. These sources are used to orient the axis of the frame (Ma et al., 1998).
- Compact sources whose positions are likely to be improved using more observations (Gontier et al., 2006) are called *candidate* sources.
- Sources that are less appropriate for astrometric uses are called *other* sources (Gontier et al., 2006).

In Table 2.2, I list all the ICRF, S/X-band catalogues and its extensions with the total number of sources and number of *defining* sources. The present realization of the frame,

TABLE 2.2: The ICRF catalogues and its extensions, listing the total numbers of reference sources as well as the number of *defining* sources in each frame.

Catalogue name	Total number of sources	Number of <i>defining</i> sources
ICRF-1	608	212
ICRF-Ext.1	667	212
ICRF-Ext.2	717	212
ICRF-2	3,414	295
ICRF-3	4,536	303

the ICRF-3 sees a major improvement in terms of the total source numbers as well as the number of *defining* sources.

The radio source positions in the ICRF are used in applications that include astronomy, geodesy, spacecraft navigation and satellite tracking, to name but a few. It is desirable to have an even distribution of the ICRF sources across the sky to achieve the mas level accuracies needed for these applications. The sessions and networks that have been used to construct the ICRF are diverse and range from as little as 2 telescopes to as large as 20 telescopes, with telescope sizes ranging from 3 meters up to 100 meters. The distribution of telescopes across the globe is also uneven and out of the ~ 53 telescopes which were used over 50 years of the ICRF, only 10 telescopes were from the Southern Hemisphere. At present, there are ~ 34 telescopes that participate in geodetic and astrometric sessions (including both regular or occasional participation) with only seven of these from the Southern Hemisphere (de Witt et al., 2018). Due to this lack of telescopes in the south, the density of sources quickly drops at declinations below -30° . In Figure 2.5, the sky distribution of the ICRF-2 and ICRF-3 sources is shown using a

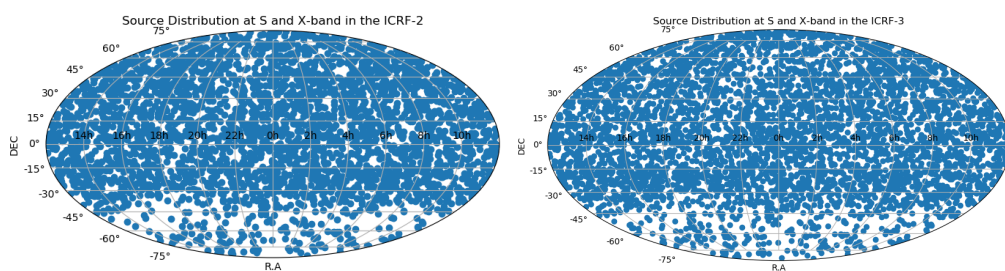


FIGURE 2.5: Hammer-Aitoff projection of source distribution in the ICRF-2 (*left panel*) and the ICRF-3 (*right panel*). Declinations below -30° are less populated with reference sources.

Hammer-Aitoff projection. In the corresponding Table 2.3, the number of the sources in the ICRF-2 and ICRF-3 are listed according to different declination ranges. Despite many efforts to increase the density and distribution of sources in the ICRF-3, the south remains weak. In comparing the declination range from $+30^\circ$ to $+90^\circ$, it can be seen that in the ICRF-3, there are twice as many sources in the North than in the South.

The ICRF sources in the North are mostly observed using the VLBA, while there is no VLBA-equivalent instrument in the South. Although the VLBA can reach down to -45° south, the formal positional errors in declinations for southern sources observed with the VLBA can be more than a factor of two higher than that observed for the right ascensions (Johnson et al., 2019). It shows that the Southern Hemisphere sky is still not well observed and more work is needed to overcome the disparity. We need both more southern observations to improve the density and accuracy of the ICRF in the South, as well as more north-south baselines observations to improve the accuracy of the frame in those areas that are hard to reach with the VLBA.

TABLE 2.3: A comparison between the ICRF-2 and ICRF-3 showing the number of the sources in the sky based on source declination range.

Catalogue	$[+90^\circ, +30^\circ]$	$[+30^\circ, +0^\circ]$	$[+0^\circ, -30^\circ]$	$[-30^\circ, -90^\circ]$
ICRF-2	1053	978	966	417
ICRF-3	1328	1287	1299	622

The ICRF-3 working group along with the IVS, schedule regular astrometric VLBI experiments specifically to strengthen the density of the ICRF sources in the South. Ojha et al. (2004a, 2005) have carried out extensive VLBI observations at X-band using the Australian Long Baseline Array (LBA), including radio telescopes in South Africa, Hawaii and Japan, to observe 111 ICRF sources in the Southern Hemisphere to study their suitability as reference frame sources through imaging. The LBA Calibrator Survey (LCS; Petrov et al., 2011) with six telescopes from Australia along with a telescope from South Africa was focused on improving source positions and analysing source structure in the Southern Hemisphere compact sources in the declination zone $[-30^\circ, -90^\circ]$. As a part of the LCS, Petrov et al. (2019) presented a second catalogue of accurate positions and flux densities of 1100 compact sources. The result sees an improvement of source positions increased by a factor of 6. The VLBI Southern Astrometry Project (SOAP) is an ongoing programme to improve the source positions below -30° by a factor of five to the level of 0.3 mas (Boehm et al., 2017). The Radio Fundamental Catalogue (RFC) provides positions and images of compact radio sources observed in all available VLBI sessions under geodesy and astrometry programmes in the Northern and Southern Hemisphere. The current version of the RFC, rfc_2019c² contains positions of 16,446 compact radio sources observed from 11 April 1980 to 29 September 2019 at multiple wavelengths in 6,971 observing sessions. However, in the rfc_2019c there are radio sources below -30° which have never been imaged at mas resolution before the imaging work presented in this thesis.

²The catalogue is available on http://astrogeo.org/vlbi/solutions/rfc_2019c/rfc_2019c.cat.html

2.5 AGN as ICRF sources

The extragalactic radio sources making up the ICRF are mainly quasars, a class of AGN. AGN are galaxies with supermassive black holes in the central regions (Kormendy & Richstone, 1995; Magorrian et al., 1998; Kormendy et al., 2009). Due to the strong gravity, interstellar gas flowing inward loses substantial potential energy that can be converted to radiation. When most of the material ends up in the black hole, a small fraction of particles get accelerated to a speed almost equivalent to the speed of light and expelled in two jets along the axis of rotation of the black hole. Among the AGN, quasars are the most luminous celestial objects in the Universe. Because of their very high luminosity, quasars are visible at extremely large distances. Because of their large distances, these celestial objects appear as fixed point sources with almost undetectable proper motions. For this reason, they are selected to define the ICRF. Blazars are AGN with highly relativistic jets that align to the observer's line-of-sight and therefore appear as point-sources. Lanyi et al. (2010) mentioned that a typical extragalactic radio source has a core with flat radio spectrum and extended emission with multiple steep spectrum jet components moving away from the core with superluminal motion. It should be noted that the peak brightness part or the flat-spectrum part in AGN is called the "core".

2.6 Importance of imaging and monitoring the intrinsic structure of ICRF sources

Extragalactic radio sources, including those making up the ICRF, may exhibit intrinsic source structure on mas scales that can vary with time, frequency and baseline projection. Fey et al. (1996), showed that intrinsic source structure can affect the estimation of the source positions. It was thought that for geodesy and astrometry observations, source structure effects can be minimised by observing only the most compact radio sources. However, from the analysis of images produced from real astrometric VLBI data, Charlot (1990b) showed that the intrinsic source structure and flux variability in ICRF sources have serious effects on geodetic and astrometric VLBI observations. Fey et al. (1996) and Fey & Charlot (1997) showed that almost all extragalactic radio sources exhibit source structure, with a core-jet morphology at some level.

In Figure 2.6, X-band VLBI images of three ICRF sources, J0006-0623, J0017+8135 and J0042+2320 from the work by Charlot et al. (2008) are presented. The source J0017+8135 shows relatively compact structure while the other two sources J0006-0623 and J0042+2320 show extended structures. In the same work, it is reported that only 40% of the *defining* sources in the ICRF-Ext.2 showed compact structure. In Figure 2.7,

the X-band VLBI images of two ICRF sources J1751+0939 and J0927+3902 are shown at two different epochs from the work by [Charlot \(2002\)](#). The source J1751+0939 was core-dominated, and the structure had evolved little between the two epochs. The source J0927+3902 on the other hand, changed from a triple structure to a single component with weak structure to the west of the peak brightness point. [Charlot \(2002\)](#) reported that the brightest component at the second epoch corresponds to the extended component on the left-hand side in the earlier epoch image. Using X-band geodetic and astrometric VLBI observations of a source, spanning more than three decades, [Fey et al. \(1997, 2008\)](#) showed that intrinsic source structure can introduce position offsets which can then appear as proper motion on the sky. Such sources should be avoided for defining the axis stability of the ICRF.

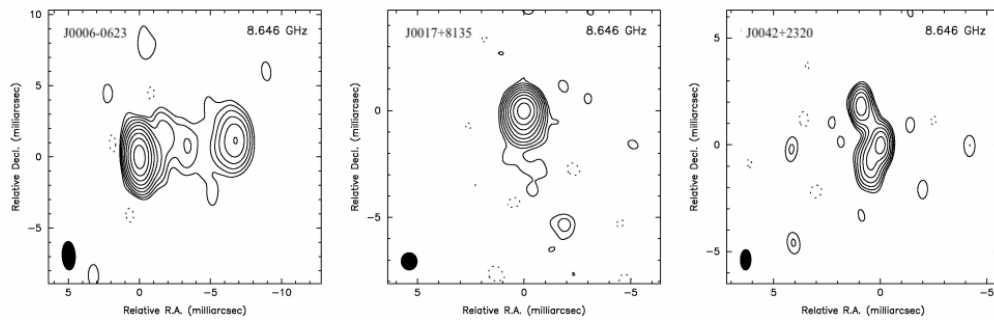


FIGURE 2.6: VLBI images of three ICRF sources: J0006-0623, J0017+8135 and J0042+2320 at X-band. The Research and Development VLBI (RDV) session on 17 December 2003 was used for imaging. North is up and East is to the left. Images are taken from [Charlot et al. \(2008\)](#).

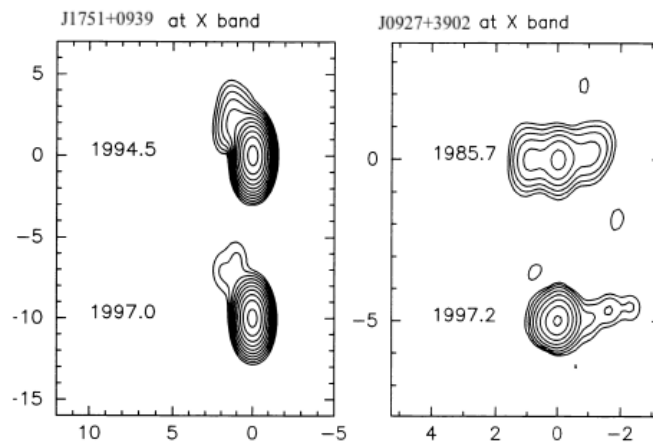


FIGURE 2.7: X-band VLBI images of the ICRF sources J1751+0939 in the *first panel* and J0927+3902 in the *second panel*. The epoch of observation is shown next to each image. Both images are aligned vertically according to their peak brightness. The scale is in mas. North is up and East is to the left. Image credit: [Charlot \(2002\)](#).

Figure [2.8](#) shows an example of the evolution of the radio structure in the ICRF source J2202+4216. The VLBI images are from ten successive epochs (1997.1 to 1998.6)

at X-band. This source shows a fast-varying structure with two components. The northern component is usually strong, except in the seventh and eighth epoch maps, where it appears to be much weaker. In the source position estimation, this source showed

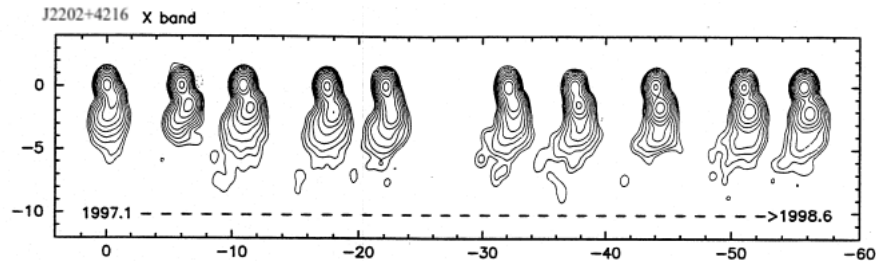


FIGURE 2.8: Multi-epoch VLBI images of the ICRF source J2202+4216 at X-band at 10 successive epochs from 1997.1 to 1998.6. The scale is in mas. North is up and East is to the left. Image credit: [Charlot \(2002\)](#).

a large position scatter in declination due to the fact that the estimated position was determined from the brightest component, which was the southern component during epoch seven and eight. The remainder of the epochs shows a much smaller position scatter between them, since the brightest component for all of these was the northern component.

The examples discussed above show that routine VLBI imaging is crucial (1) for monitoring source structure evolution, and (2) for modelling of radio source structure of sources with extended structures.

2.6.1 VLBI imaging using geodetic and astrometric observations

To maintain the accuracy of the ICRF with sub-mas precision, it is important to monitor radio source structure at S- and X-band. VLBI imaging using geodetic and astrometric observations was thought to be difficult as the (u,v) -coverage is sparse and calibration information, such as system temperature, for example, is often incomplete. However, geodetic and astrometric sessions are conducted regularly using various VLBI networks consisting of up to ten telescopes. Sources are observed simultaneously at S- and X-band in 24-hour sessions. This provides regular multi-epoch observations of all ICRF sources. [Guoqiang et al. \(1987\)](#); [Shaffer et al. \(1987\)](#); [Schalinski et al. \(1988a,b\)](#); [Charlot et al. \(1988, 1989\)](#) showed that geodetic and astrometric observations can also be used for VLBI imaging. [Charlot \(1990b\)](#), using the Crustal Dynamics Project (CDP) of geodetic and astrometric VLBI sessions, imaged fourteen sources at both S- and X-band, of which five sources were imaged for the very first time. In Figure 2.9, dual-frequency VLBI images of the ICRF source J0217+7349 are shown. In the S-band image, the source shows three jet components (B, C, D) in addition to the core (A). However, in the X-band image, the source appears to be compact. At this particular epoch of

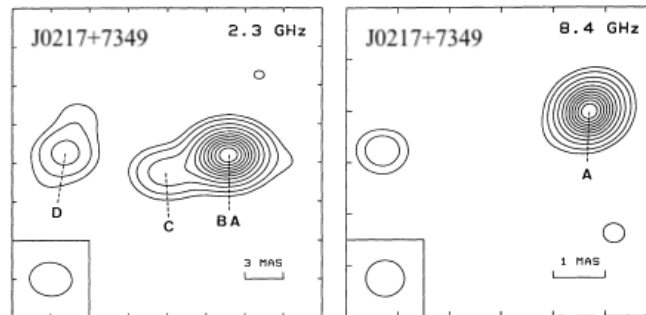


FIGURE 2.9: Dual-frequency S- and X-band VLBI images of an ICRF source J0217+7349 at epoch 1985.37. The scale of each map is indicated in the lower right-hand corner. The beam size is shown in the lower left-hand corner. Image credit: [Charlot \(1990b\)](#).

observation, this source was a good reference source at X-band but a bad candidate as a reference source at S-band where it shows extended source structure. For astrophysical purposes, some ICRF sources have been imaged extensively (e.g. J0927+3902), but others in the ICRF catalogue have never been imaged at any frequency. Therefore, a systematic programme is needed where all the ICRF sources will be imaged routinely using geodetic and astrometric observations.

In the Northern Hemisphere, ICRF sources with declination $> -30^\circ$ have been imaged regularly using various geodetic and astrometric observing programmes. The RDV sessions are carried out by the United States Naval Observatory (USNO) in collaboration with National Aeronautics and Space Administration (NASA), the Laboratoire d'Astrophysique (LAB) and the National Radio Astronomy Observatory (NRAO³) to observe radio sources on a regular basis to study the source morphology. The RDV sessions include the VLBA stations and other geodetic stations around the world. The VLBI images from this program are available on the USNO's Radio Reference Frame Image Database (RRFID⁴) and LAB's Bordeaux VLBI Image Database (BVID⁵) ([Fey et al., 1996](#); [Fey & Charlot, 1997, 2000](#); [Collioud & Charlot, 2009](#)). The first VCS (VCS1; [Beasley et al., 2002](#)) and its successors (VCS2; [Fomalont et al., 2003](#), VCS3; [Petrov et al., 2005](#), VCS4; [Petrov et al., 2006](#), VCS5; [Kovalev et al., 2007](#) and VCS6; [Petrov et al., 2008](#)) are the largest ongoing survey that provides VLBI images of radio sources with high angular resolution.

In the Southern Hemisphere, there are geodetic and astrometric VLBI observations which are yet to be used for VLBI imaging. A large number of ICRF sources below -30° have not been imaged at either S- or X-bands. The Celestial Reference Frame Deep South

³The National Radio Astronomy Observatory is a facility of the National Science Foundation (NSF) operated under cooperative agreement by Associated Universities, Inc. in USA.

⁴Images can be found at <http://rorf.usno.navy.mil/rrfid/shtml>

⁵Information about BVID is available at <http://www.obs.u-bordeaux1.fr/BVID/>

(CRDS) geodetic and astrometric VLBI experiment was identified for multi-epoch and dual-frequency imaging of the ICRF sources below -30° (Basu et al., 2014). CRDS sessions are conducted by the IVS at S- and X-band to strengthen the reference frame source density in the Southern Hemisphere.

2.7 Source structure in VLBI

At some level, almost all of the quasar sources that make up the ICRF exhibit spatially extended intrinsic structures on VLBI scales (e.g. Lister et al., 2009; Shabala et al., 2014b). It is also a well known fact that the effect of source structure on astrometric VLBI positions can be significant and that structure and flux density variability are directly related to the precision of geodetic solutions (Shabala et al., 2012). For example, a quasar with two components with equal brightness and separated by $60 \mu\text{s}$ can result in a position shift of 1.5 mm on a 10,000 km baseline (Shabala et al., 2014b). Xu et al. (2017) using a three-component model of the source J1806+6949, showed that the impact of the source structure can be up to 1.4 mm on station positions and up to $4.4 \mu\text{s}$ on the EOP. It is therefore essential to map the structures of these sources on a regular basis.

The emission structures in these quasars may also change with observing frequency and can evolve significantly over timescales of months to years. The "core" or base of quasar jets are typically optically thick because of frequency-dependent opacity effects such as synchrotron self-absorption, while the jets are optically thin. For this reason, quasar sources generally appear more compact at higher radio frequencies than at lower radio frequencies. On the other hand, going to lower radio frequencies, the resolution of the observations decreases and the effects due to intrinsic source structure disappear. Therefore, extragalactic sources for astrometric use should be evaluated independently at different frequencies, such as the traditional S- and X-bands. In addition, there is also the possibility of the structure evolving over time due to a sudden flaring event for example. For this reason, source structure should be regularly monitored over time.

Charlot (1990a) discussed the effects of source structure on geodetic and astrometric observations in great detail. From Figure 2.1, if a source with extended structure is observed, then the complex visibility function V of the source is

$$V(\vec{b}, \omega, t) = \int_{\Omega_s} I(s, \omega, t) \exp\left(-\frac{i\omega}{c} \vec{b} \cdot \hat{s}\right) d\Omega, \quad (2.10)$$

where $I(s, \omega, t)$ is the brightness distribution of the source of solid angle Ω_s , which depends on the direction, \hat{s} , of the source on the sky. If a reference point s_0 is selected

within the source then \hat{s} becomes $\hat{s} = \hat{s}_0 + \hat{\sigma}$, where $\hat{\sigma}$ is in the sky plane. Equation 2.10 then becomes

$$V(\vec{b}, \omega, t) = \exp\left(-\frac{i\omega\vec{b}\cdot\hat{s}_0}{c}\right) \times \int_{\Omega_s} I(\hat{s}_0 + \hat{\sigma}, \omega, t) \exp\left(-\frac{i\omega\vec{b}\cdot\hat{\sigma}}{c}\right) d\Omega. \quad (2.11)$$

Equation 2.11 can be written as

$$V = A \exp[i(\phi_g + \phi_s)], \quad (2.12)$$

where A is the amplitude of the source measured by the interferometer, ϕ_g is geometric phase of the reference point s_0 ,

$$\phi_g = -\frac{\omega\vec{b}\cdot\hat{s}_0}{c} \quad (2.13)$$

and ϕ_s is additional structural phase of the source

$$\phi_s = \arg\left[\int_{\Omega_s} I(\hat{s}_0 + \hat{\sigma}, \omega, t) \exp\left(-\frac{i\omega\vec{b}\cdot\hat{\sigma}}{c}\right) d\Omega\right]. \quad (2.14)$$

The amplitude of the source is

$$A = \left|\int_{\Omega_s} I(\hat{s}_0 + \hat{\sigma}, \omega, t) \exp\left(-\frac{i\omega\vec{b}\cdot\hat{\sigma}}{c}\right) d\Omega\right|. \quad (2.15)$$

In geodetic and astrometric VLBI observations, the delay observable τ is the partial derivative of the total phase ϕ_t with respect to ω . The total phase is the sum of ϕ_g and ϕ_s and is written as,

$$\tau = \frac{\partial\phi_g}{\partial\omega} + \frac{\partial\phi_s}{\partial\omega} = -\frac{1}{c}\vec{b}\cdot\hat{s}_0 + \tau_s \quad (2.16)$$

The delay rate observable is the partial derivative of the total phase with respect to ω , where

$$\dot{\tau} = \frac{1}{\omega} \left(\frac{\partial\phi_g}{\partial t} + \frac{\partial\phi_s}{\partial t} \right) = -\frac{1}{c} \frac{d}{dt} (\vec{b}\cdot\hat{s}_0) + \dot{\tau}_s. \quad (2.17)$$

The first term in Equation 2.16, $\frac{1}{c}(\vec{b}\cdot\hat{s}_0)$ is the geometric delay due to the reference point, and the second term τ_s is due to the additional delay caused by the brightness distribution of the source.

For geodetic and astrometric purposes, the most compact sources are selected, in order to reduce the ambiguity in the source position selection. Given that, to select compact sources, it would be useful to have a measure of the magnitude of source structure, compactness of the source and how extended the source is. Since astrometric VLBI observations are typically done at dual-frequency S/X-band, these source structure indicators must be determined separately for each band.

2.7.1 Source structure indicators in VLBI

2.7.1.1 Source structure index

VLBI images are produced using the hybrid mapping procedure described by [Readhead & Wilkinson \(1978\)](#). This procedure uses a finite number of CLEAN (as discussed in section 2.1.3.1) components such that,

$$I(s) = \sum_{i=1}^k [I_i \delta(o\vec{s} - o\vec{s}_i)], \quad (2.18)$$

where $(o\vec{s}_i, I_i)$ are the position and intensity of the i -th CLEAN component. Each of these CLEAN components has a position and intensity. The CLEAN components are generally convolved with a Gaussian beam when restored to the map. In Equation 2.18, o is an arbitrary origin near the source, such that $s_0\vec{s} = o\vec{s} - o\vec{s}_0$. The structure effects depend on the positions and intensities of these components. To calculate the effect of the structure, each pixel is replaced by a delta-function (CLEAN component) with a flux density equal to that of the pixel. [Charlot \(1990a\)](#), adopting the mathematical form used by [Thomas \(1979\)](#), showed that the structure delay τ_s depends on the (u, v) -coordinates of the baseline \vec{b} .

The structure delay corrections are calculated as the slope of a straight line fitted to the individual structure phases for each frequency channel in an observation. In

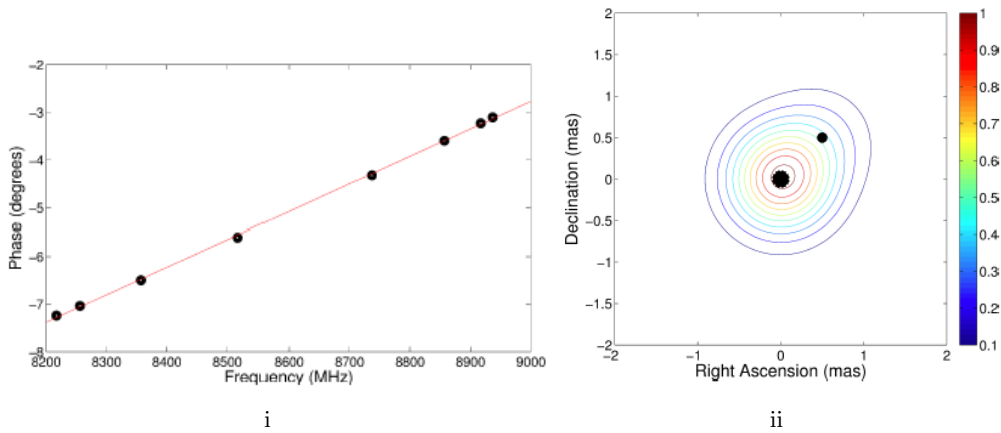


FIGURE 2.10: The plot shows (i) the change in the structure phase over each frequency channel for a simulated two-component source, shown in (ii). The baseline length is 9,280 km. The slope represents the source structure contribution to the delay. The eight sub-bands of the X-band observations are represented by black points. In the simulated model (ii), each component is modeled as δ function and convolved with a beam size of 1 mas. Flux density is represented by different colours. Image credit: [Shabala et al. \(2014a\)](#).

Figure 2.10, the structure delay corrections of a two-component source model are shown.

Fey & Charlot (1997) defined a structure index (SI) to assess the astrometric quality of extragalactic radio sources. To estimate an overall magnitude of intrinsic source structure, τ_s is calculated for all pixels in a 512×512 (u, v)-grid within a circle with a radius equivalent to the diameter of the Earth. Then the mean, root mean square (RMS) and median values of the structure corrections are calculated over the relevant resolution area. The structure corrections are done separately for S- and X-band.

The calculation of τ_s for any source requires the choice of a reference point s_0 within the source brightness distribution. The position of s_0 for any source is unknown with respect to the CRF. A least-square procedure by Fey & Charlot (1997) is used, where s_0 is automatically selected minimising the delay RMS for that source. The choice of s_0 is made in such a way that any other choice of the reference point would produce a larger RMS delay. Furthermore, it was shown that the position of s_0 is “located at or near the peak of the brightness distributions (and not at the centroid of the brightness distributions, as one would expect)” as mentioned by Fey & Charlot (1997). The SI is calculated using the median of the calculated structure corrections, $\tau_{\text{median}} \equiv \tau_s(\text{median})$ as

$$\text{SI} = 1 + 2 \log(\tau_{\text{median}}). \quad (2.19)$$

Equation 2.19 is used for astrometric quality assessment of extragalactic radio sources. The τ_{median} is calculated in picoseconds (ps) and SI values are always positive by considering $\text{SI} = 0$ when $\log(\tau_{\text{median}}) < -0.5$ ps. The SI ranges from 1 to 4 with $\text{SI} = 1$, if $0 \text{ ps} \leq \tau_{\text{median}} < 3 \text{ ps}$; $\text{SI} = 2$, if $3 \text{ ps} \leq \tau_{\text{median}} < 10 \text{ ps}$; $\text{SI} = 3$, if $10 \text{ ps} \leq \tau_{\text{median}} < 30 \text{ ps}$ and $\text{SI} = 4$, if $30 \text{ ps} \leq \tau_{\text{median}} < \infty$. As the brightness distribution of the source is a function of time, the time-dependent temporal evolution of the brightness distribution affects the SI (Charlot, 2008). Sources with an SI of 1 or 2 are considered as the best candidates for both astrometric and geodetic purposes. Sources with an SI of 3 or more are not recommended for geodetic and astrometric purposes (Ma et al., 2009). A careful selection of sources prior to any geodetic and astrometric VLBI sessions is necessary to minimise errors in the observables.

Figure 2.11 shows as example, a VLBI contour map and source structure correction map for the ICRF source J0538-4405 at X-band. The panel (i) shows the VLBI contour map of the source and panel (ii) shows the effect of the intrinsic source structure on VLBI delay measurements over the (u, v)-plane. The median group delay is 9.8 ps, which is equivalent to an SI of 2. The source is a good candidate to be used as a reference source. Fey & Charlot (2000) determined the SI of 225 ICRF sources to analyse their astrometric quality. They reported that sources with higher SI, and thus extended structure, showed larger position uncertainties.

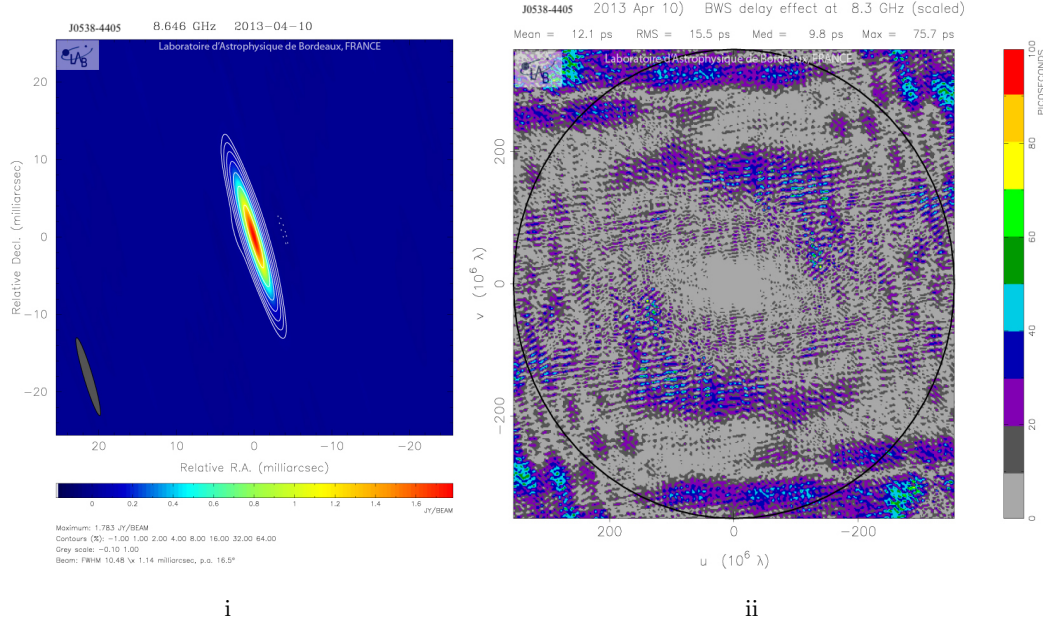


FIGURE 2.11: The VLBI image and median group delay due to source structure in the ICRF source J0538-4405 at X-band. (i) The VLBI image is at the epoch 10 April 2013. The beam size is shown in the bottom left corner. The source has a compact core and shows no extended structure. The delay distribution map shows no delay. The source has an SI of 2. The circle in the panel (ii) represents the baseline equivalent to the diameter of the Earth (Charlot, 2008). North is up and East is to the left. The VLBI image and the structure correction map are taken from the BVID.

2.7.1.2 Source compactness

The other metric that is used to assess the astrometric quality of reference sources is source compactness (SC). To calculate the compactness of a source, the SC was introduced by Ojha et al. (2004b), and is given by,

$$SC = \frac{S_{cc}}{S_{total}}, \quad (2.20)$$

where S_{cc} is the sum of flux densities of CLEAN components within one synthesized beam of the brightest pixel and S_{total} is the sum of flux densities of all CLEAN components. The SC can be greater than 1 if negative CLEAN components are included.

2.7.1.3 Radial extent

Another metric that is used to measure the compactness is the flux-weighted radial extent (Ojha et al., 2004b). The flux-weighted radial extent (R_w) is defined as

$$R_w = \frac{\sum_i S_i r_i}{\sum_i S_i}, \quad (2.21)$$

where r_i is the radius where the i -th CLEAN component has S_i flux density. The R_w is in units of mas.

To measure how extended a source is, the unweighted radial extent ($R_{95\%}$) is calculated,

$$R_{95\%} = \frac{\sum_i (S_i)_\theta}{\sum_i S_i}. \quad (2.22)$$

From Equation 2.22, $(S_i)_\theta$ is the flux density within an area of angular radius $0 \leq \theta < \infty$. The angular radius θ (in mas) contains 95% of the total CLEAN flux density. Here, $R_{95\%}$ is in units of mas.

2.7.1.4 Modulation index

In radio sources, flare amplitude is an indicator of the relative brightness of the core and jet components. A higher amplitude is an indicator of a brighter jet component relative to the core. The modulation index (μ) (Shabala et al., 2014b) is

$$\mu = \frac{\sigma_s}{\bar{s}}, \quad (2.23)$$

where \bar{s} is the mean flux density and σ_s is the RMS of \bar{s} . A higher value of μ indicates the launching of a bright new jet component thus the evolution of a potential source structure.

The above metrics have all been employed to assess the astrometric quality of the sources imaged in this study.

Chapter 3

Observations and Data Reduction

In order to assess and monitor the astrometric quality of reference sources in the South, I started a campaign in 2013 to map the structure of such sources observed through routine geodetic observations in the South.

This chapter describes the selection process I followed in choosing astrometric and geodetic VLBI observations in the South that would be suitable for imaging. This chapter also describes the observational setup of these chosen sessions and the data reduction process that I followed. Before selecting a particular experiment, the following basic criteria were set for the experiment:

- The VLBI network had to include telescopes in the Southern Hemisphere only. This criterion was set so that all the telescopes in the network can have access to sources in the declination range $[-30^\circ, -90^\circ]$.
- No subnetting, i.e. only sessions where all telescopes observe the same source at the same time, were considered. This is to avoid two and three station scans that are common in geodetic observations, but not suitable for imaging purposes.
- A minimum number of four telescopes are required for imaging. Another factor that was considered was on source scan time. A scan time of ~ 4 -5 minutes is considered to be good for imaging.
- Preference was given to the sessions where sources were observed in more than one scan spread throughout the 24-hour observing session, for maximum (u, v) -coverage.

Below is a list and description of all the regular southern IVS programmes that were considered for imaging. Table 3.1 provides some statistics on the observing programmes that were used for my assessment.

- **The AUSTRal sessions:** The purpose of these geodetic observations is to provide high precision station coordinates, source coordinates and EOP in the South (Plank et al., 2017). In the AUSTRal sessions, telescopes from South Africa, Australia and New Zealand are included. These sessions make use of sub-netting.
- **The CRDS sessions:** The CRDS geodetic and astrometric sessions were coordinated by the U.S. Naval Observatory. However, since 2018 the sessions are being coordinated by Dr Aletha de Witt at HartRAO. The CRDS sessions are used to strengthen the ICRF in the deep south, below -30° declination. Only telescopes from the Southern Hemisphere are used, and these sessions include four to six participating telescopes. Since the majority of the scans in these sessions are observed with at least four telescopes and no sub-netting, the CRDS sessions were considered for imaging.
- **The CRF sessions:** The CRF sessions are also coordinated by the U.S. Naval Observatory. The CRF geodetic and astrometric sessions are conducted to strengthen the ICRF in the Southern Hemisphere. For most of the 2013 sessions, observations were done using only three telescopes, which is not suitable for imaging.
- **The OHIG sessions:** The purpose of the IVS-OHIG (Southern Terrestrial Reference Frame) sessions is to tie the sites in the Southern Hemisphere and to provide a very accurate TRF around the South Pole. These sessions make use of sub-netting and the majority of the scans are observed with less than four telescopes.

TABLE 3.1: Observing statistics for all the regular observed southern IVS programmes, for all sessions observed between January 2013 and December 2013. The table lists the programme name, number of sessions, the number of participating telescopes per session, the average number of scans per session observed with four or more telescopes and the average number of scans per session observed with less than four telescopes.

Programme name	Number of sessions in 2013	Number of telescopes per session	Average number of scans from ≥ 4 telescopes per session	Average number of scans from < 4 telescopes per session
AUST	24	3-5	118.0	183.0
CRDS	6	4-6	130.0	2.66
CRF	6	3-6	43.66	106.55
OHIG	6	5-8	45.83	284.0

After my assessment of all the Southern Hemisphere geodetic VLBI programmes, the CRDS sessions were selected. The CRDS sessions meet all the criteria that have been set. All the participating telescopes are located in the Southern Hemisphere. In addition, ICRF-2 *defining* sources at a declination range $[-30^\circ, -90^\circ]$ are observed.

In every session, 38 sources are observed in 5-6 scans each, with no sub-netting. The number of observing sessions are 5 or 6 per year, with each source being observed at least three times per year, which provides the opportunity for multi-epoch mapping of the same source. The number of participating telescopes are between 4 and 6 providing a decent (u,v) -coverage that can be used for imaging. In Figure 3.1 the locations of telescopes in CRDS sessions are shown. Telescopes in South Africa, Australia and New Zealand are used in the observations.



FIGURE 3.1: Locations of the telescopes used in the CRDS sessions. The Geoscience Australia (GA) is IVS analysis centre in the Southern Hemisphere and is located in Canberra, Australia. The figure courtesy: International VLBI Service for Geodesy & Astrometry.

Prior to selecting the first or pilot session for imaging, the available CRDS sessions at the time, were all investigated. All CRDS sessions before 2012 were discarded as they had only two or three participating telescopes. The remainder of the sessions included CRDS-57 to CRDS-63 that were correlated and available for analysis at the time. After careful investigation of the correlator reports and observation log files, a number of these sessions were discarded for the following reasons:

- Only 3 telescopes participated in the CRDS-57, -58 and -59 sessions.
- In CRDS-60, among the four participating telescopes, very few scans were recorded at X-band for one of the telescopes and on another telescope, channels had to be removed from the fringe fitting.
- In CRDS-61, among the five participating telescopes, one baseline displayed a large clock drift during the last five hours of observation. A low phase-cal amplitude was detected throughout the entire session.
- The CRDS-62 session had some issues related to the configuration of the Digital Baseband Converters (DBBC) for two of the telescopes (among the five telescopes that were scheduled), and one telescope did not participate.

The CRDS-63 session showed the best performance and it was chosen as the pilot session. The results of the data reduction and imaging of CRDS-63 were presented in [Basu et al. \(2014\)](#).

Following the successful analysis and imaging of the CRDS-63 session, a request to increase the observing bandwidth from 4 to 8 MHz was submitted to the IVS. This request was approved, and the bandwidth was increased to 8 MHz, starting from CRDS-66. The CRDS-66 and -68 sessions were selected for further analysis, as these sessions observed the same source list, and thus provided multi-epoch analysis of source structure. After CRDS-68, correlation of CRDS sessions became very slow, due to an upgrade at the Washington correlator, and no further sessions were available for analysis. At this point and after the successful imaging of the CRDS-66 and -68 sessions, selected members from the IAU, ICRF-3 working group, requested a re-assessment of the scheduling, setup, data rates and source selection of the CRDS sessions. This was done in an effort to improve the CRF in the south towards the realisation of the next generation ICRF. This request was successful, and details of the efforts to improve these sessions are reported in [de Witt et al. \(2019a,b\)](#). As a result, from CRDS-93 onward the data rate for all CRDS sessions was increased from 256 Mbps to 1 Gbps. A special request from the ICRF-3 working group to obtain maps of potential *defining* sources for the ICRF-3 in the south was submitted, and these were observed in the CRDS-94 session. Due to the urgency in obtaining these results before the final submission of the ICRF-3, special preference was given to the correlation of this session, despite the backlog at the Washington correlator (WACO). The data analysis and imaging results from the CRDS-94 session are presented in this thesis.

In Table 3.2, I list all the CRDS sessions that were used for imaging and presented in this thesis, along with the observation date, participating telescopes, number of sources and the number of scans per source. The telescopes that participated in CRDS sessions are: HartRAO 26 m (Hh) and HartRAO 15 m (Ht) in South Africa, Hobart 26 m (Ho), Hobart 12 m (Hb), Katherine 12 m (Ke) and Yarragadee 12 m (Yg) in Australia and Warkworth 12 m (Ww) in New Zealand. The number of sources was increased from 38 in CRDS-66 to 51 in the CRDS-94, and the number of scans was increased from 3 to 4 scans per source in CRDS-66 to 5 to 7 scans per source in CRDS-94. Section 3.1 provides more detail on each individual session.

3.1 Sources observed in the CRDS sessions

In the earlier CRDS sessions up to CRDS-92, which was conducted on 23 November 2017, only ICRF-2 *defining* sources were observed. Prior to the release of the ICRF-3

TABLE 3.2: List of the CRDS sessions with observation date, telescopes, number of sources, number of scans per source, and data rate of each session. The observation dates are in dd mm yyyy format. It should be noted that the same set of sources have been observed in the CRDS-66 and 68 sessions.

Session name	Observation date	Telescope codes	Number of sources	Scans per source	Data rate per session
CRDS-63	14 01 2013	Hh-Ho-Ke-Yg-Hb-Ww	38	3-4	256 Mbps
CRDS-66	30 07 2013	Hb-Hh-Ho-Ke-Ww	38	4-6	256 Mbps
CRDS-68	27 11 2013	Hb-Hh-Ho-Ke-Ww-Yg	38	4-6	256 Mbps
CRDS-94	21 03 2018	Hh-Ht-Ke-Ww-Yg-Ho	51	5-7	1 Gbps

in January 2018, ICRF-2 non-defining sources were also added to the CRDS sessions. The CRDS-94 session was a special request to observe potential *defining* sources from the list of ICRF-3 sources. A total of 103 individual sources was observed in the four CRDS sessions that were selected for imaging and that is presented in this work. Source coordinates and physical properties of the 103 sources which were observed in the four CRDS sessions are listed in Table 3.3.

TABLE 3.3: List of sources observed in the CRDS-63, -66, -68 and -94 sessions at S- and X-band. Type of Objects: Q = quasar, G=galaxy, R = radio source, A = active galactic nucleus, V = optical source, L = BL Lac type object. Optical identification, type of object, redshift, and visual magnitude of the sources are obtained from the NASA/IPAC Extragalactic Database (NED) operated by the Jet Propulsion Laboratory, California Institute of Technology. The right ascension (R.A.) and declinations (Dec.) have been obtained from the ICRF-3 catalogue available on the [International Earth Rotation and Reference System Service \(IERS\) ICRS Center web page](#).

Note: (Source name)^a = Source with existing image(s), (Source name)^b = Source with first-ever image(s).

Source name (J2000 name)	R.A. (hh mm ss)	Dec. (deg mm ss)	Type of object	Redshift z	Visual mag.
J0004-4736 ^a	00 04 35.65548526	-47 36 19.6040054	A	–	19.0
J0040-5903 ^b	00 40 07.84912229	-59 03 52.7641561	R	–	–
J0051-4226 ^a	00 51 09.50182132	-42 26 33.2933576	Q	1.749	18.8
J0106-4034 ^a	01 06 45.10796439	-40 34 19.9603733	Q	0.584	19.0
J0109-6049 ^a	01 09 15.47519907	-60 49 48.4601187	G	–	21.4
J0133-5200 ^b	01 33 05.76250002	-52 00 03.9454078	G	0.020	20.3
J0229-7847 ^b	02 29 34.94659694	-78 47 45.6017623	Q	1.070	18.6
J0236-6136 ^a	02 36 53.24574011	-61 36 15.1835463	A	–	17.8
J0253-5441 ^b	02 53 29.18040456	-54 41 51.4360977	Q	0.539	16.7
J0303-6211 ^b	03 03 50.63135648	-62 11 25.5500344	A	–	19.1
J0309-6058 ^b	03 09 56.09914475	-60 58 39.0564095	A	–	18.6
J0334-4008 ^a	03 34 13.65448823	-40 08 25.3979928	L	1.445	18.5
J0335-5430 ^a	03 35 53.92483282	-54 30 25.1149291	A	–	20.4

Continued on next page

Table 3.3 – *Continued from previous page*

J0403-3605 ^a	04 03	53.74990003	-36 05	01.9131880	Q	1.417	17.2
J0406-3826 ^a	04 06	59.03533781	-38 26	28.0423651	Q	1.285	17.5
J0408-6545 ^b	04 08	20.37820341	-65 45	09.0796788	Q	0.962	20.2
J0439-4522 ^a	04 39	00.85466368	-45 22	22.5631875	V	–	20.5
J0450-8101 ^a	04 50	05.44021015	-81 01	02.2314265	G	0.444	19.6
J0506-6109 ^b	05 06	43.98874900	-61 09	40.9939787	Q	1.093	16.9
J0516-6207 ^b	05 16	44.92617055	-62 07	05.3894029	A	–	21.0
J0522-6107 ^b	05 22	34.42547703	-61 07	57.1337711	Q	1.400	18.1
J0525-4557 ^a	05 25	31.40016020	-45 57	54.6851720	Q	1.479	17.3
J0526-4830 ^b	05 26	16.67131784	-48 30	36.7919695	V	–	–
J0534-6106 ^b	05 34	35.77249760	-61 06	07.0732746	A	–	18.8
J0536-3401 ^a	05 36	28.43236164	-34 01	11.4684065	R	0.683	–
J0538-4405 ^a	05 38	50.36155950	-44 05	08.9390233	Q	0.894	15.5
J0550-5732 ^b	05 50	09.58019747	-57 32	24.3965358	A	–	19.5
J0922-3959 ^a	09 22	46.41826886	-39 59	35.0682386	Q	0.591	18.8
J0930-8533 ^b	09 30	32.56883295	-85 33	59.6951729	R	–	–
J1006-5018 ^a	10 06	14.00931655	-50 18	13.4707354	R	–	–
J1014-4508 ^a	10 14	50.35496789	-45 08	41.1545323	R	–	–
J1023-6646 ^a	10 23	43.53319662	-66 46	48.7176018	R	–	–
J1036-3744 ^a	10 36	53.43960110	-37 44	15.0658359	Q	1.821	19.5
J1041-4740 ^a	10 41	44.64995750	-47 40	00.0662184	R	–	–
J1047-6217 ^b	10 47	42.95229991	-62 17	14.6339246	R	–	–
J1103-5357 ^b	11 03	52.22168463	-53 57	00.6966389	A	–	16.2
J1112-5703 ^b	11 12	07.26964892	-57 03	39.7485632	R	–	–
J1118-4638 ^b	11 18	26.95766041	-46 34	15.0014696	Q	0.713	17.0
J1131-5818 ^a	11 31	43.28800354	-58 18	53.4433715	R	–	–
J1145-6954 ^a	11 45	53.62418068	-69 54	01.7975812	A	–	17.7
J1147-3812 ^a	11 47	01.37071212	-38 12	11.0235229	Q	1.048	16.2
J1151-6728 ^a	11 51	13.42652510	-67 28	11.0937870	Q	–	–
J1159-6635 ^b	11 59	18.30545044	-66 35	39.4270701	R	–	–
J1254-7138 ^b	12 54	59.92148599	-71 38	18.4366378	A	–	20.5
J1316-3338 ^a	13 16	07.98594757	-33 38	59.1726741	Q	1.210	20.0
J1326-5256 ^b	13 26	49.22911822	-52 56	23.6331968	R	–	–
J1329-5608 ^b	13 29	01.14491196	-56 08	02.6655453	R	–	–
J1337-6509 ^b	13 37	52.44505888	-65 09	24.8967038	R	–	–
J1346-6024 ^b	13 46	49.04248361	-60 24	29.3553900	R	0.012	15.7
J1352-4412 ^a	13 52	56.53494646	-44 12	40.3876155	L	0.050	18.0

Continued on next page

Table 3.3 – *Continued from previous page*

J1355-6326 ^b	13 55	46.61196956	-63 26	42.5731446	R	–	–
J1424-6807 ^b	14 24	55.55739084	-68 07	58.0945831	A	–	22.2
J1427-4206 ^a	14 27	56.29756617	-42 06	19.4376238	Q	1.522	17.7
J1452-6502 ^a	14 52	39.67918743	-65 02	03.4332326	G	–	22.0
J1454-4012 ^a	14 54	32.91237565	-40 12	32.5143755	Q	1.810	18.5
J1514-4748 ^b	15 14	40.02460253	-47 48	29.8576501	R	–	17.2
J1538-6525 ^b	15 38	11.91524402	-65 25	51.1960789	R	–	–
J1558-6432 ^a	15 58	50.28435260	-64 32	29.6372793	G	0.080	17.0
J1607-3331 ^a	16 07	34.76234762	-33 31	08.9134699	V	–	–
J1616-7108 ^b	16 16	30.64150379	-71 08	31.4541912	A	–	20.7
J1624-6809 ^a	16 24	18.43700381	-68 09	12.4965744	Q	1.354	18.0
J1628-6152 ^a	16 28	54.68980334	-61 52	36.3980187	R	–	–
J1642-8108 ^b	16 42	57.34556496	-81 08	35.0702204	A	–	18.0
J1650-5044 ^b	16 50	16.62710806	-50 44	48.2106956	R	–	–
J1701-5621 ^b	17 01	44.85812893	-56 21	55.9026861	R	–	–
J1703-6212 ^b	17 03	36.54121471	-62 12	40.0085591	V	–	–
J1733-7935 ^b	17 33	40.70024557	-79 35	55.7165873	A	–	19.7
J1744-5144 ^b	17 44	25.45488279	-51 44	43.7403710	G	0.630	20.8
J1803-6507 ^b	18 03	23.49665086	-65 07	36.7613089	V	–	20.6
J1809-4552 ^a	18 09	57.87174351	-45 52	41.0141114	G	0.070	15.7
J1819-5521 ^a	18 19	45.39951531	-55 21	20.7453837	A	–	18.9
J1829-5813 ^b	18 29	12.40235306	-58 13	55.1618061	R	–	–
J1835-7149 ^b	18 35	37.20374085	-71 49	58.2188048	R	–	–
J1837-7108 ^a	18 37	28.71496089	-71 08	43.5546170	Q	1.356	17.5
J1857-5325 ^b	18 57	00.45230781	-53 25	00.3799176	Q	0.777	–
J1930-6056 ^a	19 30	06.16008387	-60 56	09.1841871	A	–	20.3
J1932-4536 ^a	19 32	44.88774432	-45 36	37.9289309	Q	0.652	17.1
J1933-6942 ^b	19 33	31.15992348	-69 42	58.9145557	Q	1.480	20.6
J1937-3958 ^a	19 37	16.21735889	-39 58	01.5531167	Q	0.965	18.0
J1940-6907 ^a	19 40	25.52815148	-69 07	56.9717355	Q	3.100	17.3
J1941-6211 ^b	19 41	21.76858343	-62 11	21.0567014	Q	–	–
J1955-6115 ^b	19 55	10.77063819	-61 15	19.1368409	Q	–	–
J1957-3845 ^a	19 57	59.81927491	-38 45	06.3558881	Q	0.630	17.1
J2005-3723 ^a	20 05	55.07089847	-37 23	41.4779107	R	–	–
J2035-6846 ^a	20 35	48.87649820	-68 46	33.8406140	Q	1.084	19.4
J2056-4714 ^a	20 56	16.35980507	-47 14	47.6277179	Q	1.474	19.1
J2109-4110 ^a	21 09	33.18859274	-41 10	20.6054240	Q	1.060	21.0

Continued on next page

Table 3.3 – *Continued from previous page*

J2126-4605 ^a	21	26	30.70426552	-46	05	47.8920927	Q	1.670	18.0
J2147-7536 ^a	21	47	12.73063669	-75	36	13.2249063	Q	1.139	17.3
J2207-5346 ^a	22	07	43.73329058	-53	46	33.8199643	Q	1.206	18.0
J2223-3455 ^a	22	23	05.93055963	-34	55	47.1778251	G	0.298	–
J2235-4835 ^a	22	35	13.23657823	-48	35	58.7945202	Q	0.510	17.2
J2239-5701 ^a	22	39	12.07589936	-57	01	00.8395331	V	–	18.5
J2247-3657 ^a	22	47	03.91732859	-36	57	46.3041035	Q	2.252	19.0
J2248-3235 ^a	22	48	38.68573790	-32	35	52.1881477	Q	2.268	18.6
J2303-6807 ^a	23	03	43.56459610	-68	07	37.4431119	Q	0.510	16.4
J2329-4730 ^a	23	29	17.70434484	-47	30	19.1148088	Q	1.299	16.8
J2336-4115 ^a	23	36	33.98507717	-41	15	21.9840535	A	1.406	20.0
J2336-5236 ^b	23	36	12.14453637	-52	36	21.9510844	Q	–	–
J2347-5110 ^a	23	47	19.86408334	-51	10	36.0653515	A	2.670	20.1
J2356-6820 ^a	23	56	00.68142337	-68	20	03.4720105	A	1.716	17.0
J2357-5311 ^b	23	57	53.26605016	-53	11	13.6895021	Q	1.006	17.8
J2359-3133 ^a	23	59	35.49153939	-31	33	43.8246834	Q	0.990	17.6

3.2 Selected CRDS sessions

In this section, I present detailed information about the CRDS sessions which were used for imaging. As a part of the description of each session, start and end times (in UT) of each session, day of year (DOY) when the session started and ended, number of sources observed, total number of scans, average scan time and telescopes which participated in the session are presented.

3.2.1 The CRDS-63 session

The CRDS-63 was the first session used for imaging and was the first CRDS session from 2013. The CRDS-63 session started at 08:00 UT on 14 January 2013 (DOY 14) and ended at 8:00 UT on 15 January 2013 (DOY 15). A total of 38 ICRF-2 *defining* sources were observed during the 24-hour observation. The total number of scans was 121 with 3 to 5 scans per source. The average scan time was 9 minutes. The four telescopes that participated in the session were Hh, Hb, Ke and Yg. The (u, v) -coverage of two randomly selected sources J1837-7108 and J1427-4206 are presented in Figure 3.2.

Source J1837-7108 was observed in three scans and source J1427-4206 was observed in four scans. The limited number of telescopes and the small number of scans per source resulted in a very sparse (u,v) -coverage, which made imaging challenging.

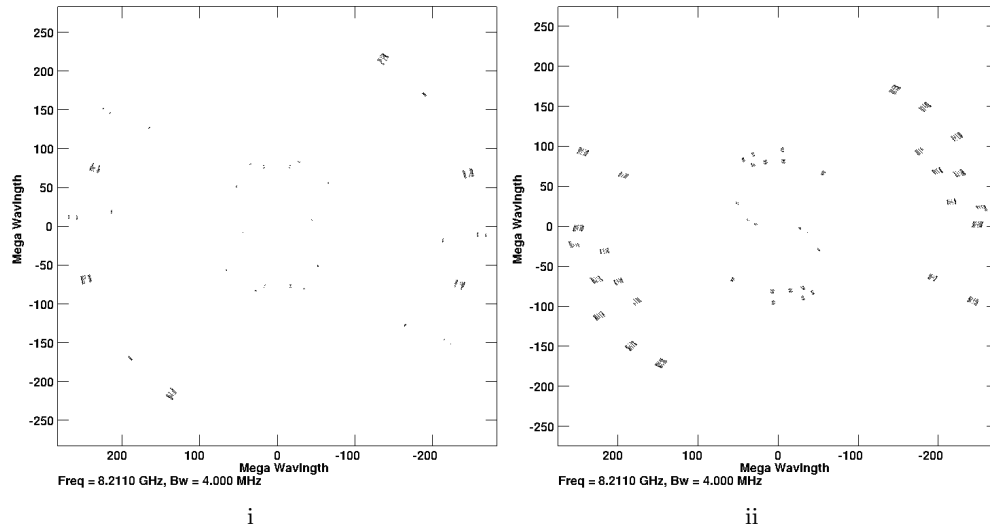


FIGURE 3.2: The (u,v) -coverage of two sources (i) J1837-7108 and (ii) J1427-4206 at X-band from the CRDS-63 session. North is up indicating v and East is to left indicating u . The baseline length is given in mega wavelength ($M\lambda$) units. The gap between the inner and outer shell is due to the absence of telescopes between Australia and South Africa.

In the CRDS-63 session, a bandwidth of 4 MHz was used and the data were recorded in Right Circular Polarization (RCP) with 6 intermediate frequencies (IFs) at S-band and 8 IFs at X-band. The data were correlated using the Mark IV correlator at the WACO.

The CRDS-63 session was used as a pilot session to determine whether any geodetic VLBI sessions in the Southern Hemisphere will be suitable for imaging purposes. After successful imaging of sources from the CRDS-63 session, it was decided to continue analysing additional CRDS sessions.

Note: Preliminary VLBI imaging results from CRDS-63 were presented in [Basu et al. \(2014\)](#).

3.2.2 The CRDS-66 session

The CRDS-66 session was observed on 30 July 2013, and was the fourth CRDS session of the year, following CRDS-63, -64 and -65. The five telescopes that participated were Hh, Hb, Ho, Ke, and Yg. The CRDS-66 session started at 17:30 UT on 30 July (DOY 211), 2013 and ended at 17:24 UT on 31 July 2013 (DOY 212).

The total number of observations and the total number of recorded scans were 1245 and 145, respectively, with 3 to 5 scans per source. A total 38 ICRF-2 *defining* sources were observed in this session with an average scan time of 7 minutes. Data were recorded in RCP, with 6 IFs at S-band and 8 IFs at X-band, and a bandwidth of 8 MHz was used. The data were correlated at the WACO using the Mark IV VLBI correlator. No fringes were detected for the Hobart 12 m telescope for the first six hours of observation.

3.2.3 The CRDS-68 session

The CRDS-68 was the last CRDS session of 2013. The session started at 19:00 UT on 27 November (DOY 331) and ended at 18:51 UT on 28 November (DOY 332). There were six participating telescopes which were Hh, Ho, Hb, Ke, Yg and Ww. The same 38 ICRF-2 *defining* sources as in the CRDS-66 session was observed. The total number of recorded scans and total number of observations were 144 and 1846, respectively, with 3 to 5 scans per source and an average scan time of 7 minutes. Data were recorded in RCP, with 6 IFs at S-band and 8 IFs at X-band. Data were correlated at the WACO using the Mark IV VLBI correlator. All the data from the Warkworth telescope were lost due to errors during correlation and were not recoverable. Due to technical issues, the S-band data were lost. Therefore, no S-band images of the sources are available.

3.2.4 The CRDS-94 session

The CRDS-94 session started at 18:00 UT on 21 March 2018 (DOY 80) and ended at 18:00 UT on 22 March 2018 (DOY 81). The number of sources in the CRDS-94 schedule was 51 with 20 new sources being added. Telescopes participating were Hh, Ht, Ke, Yg, and Ww. The number of scans per source was 5 to 7 with an average scan time of 7 minutes. The data were recorded in RCP, with 6 IFs at S-band and 10 IFs at X-band and an observing bandwidth of 16 MHz. The data were correlated at the Shanghai Astronomical Observatory (SHAO) using the Mark IV correlator.

Several problems were detected in the session, which are mentioned below:

- A total of 141 scans were missed on the Ht due to failure of the telescope controller.
- Ho did not participate due to major brake failure.
- A total of 76 scans were not recorded on Ke due to various errors.

Improved (u,v) -coverage

The increase in both the number of participating telescopes and also the number of scans per source, in the CRDS-66 and CRDS-68 sessions, provided a huge improvement in the (u,v) -coverage compared to the CRDS-63 session.

The number of participating telescopes in CRDS-66 and onwards were increased to either 5 or 6 telescopes, and the bandwidth was increased to 8 MHz. Also, the average number of scans per source from CRDS-66 onwards was increased to ~ 5 with an on-source scan time of ~ 6 minutes. The (u,v) -coverage for one of the sources from the CRDS-66 session, J0450-8101, is presented in Figure 3.3. The figure shows the improvement in the (u,v) -coverage, compared to that from the CRDS-63 session (see Figure 3.2).

3.3 Conversion of the data to FITS file

The older correlated CRDS data sets (including CRDS-63, -66, and -68), were only available in Mark IV format, intended for further geodetic analysis. For imaging analysis, these data sets had to be converted to Flexible Image Transport System (FITS) format (post correlation), in order to be analysed using astronomical VLBI software. The raw MarkIV correlated data were received from the correlator in four different file types:

- The ROOT file is an ASCII file. One ROOT file has one scan.
- The correlated data file is a binary file. One file per baseline.
- The Fringe-fitted data file is a binary file. One file per baseline and frequency. These files are created by the Haystack Observatory Post-correlation System (HOPS) and HOPS-FOURFIT program (Cappallo, 2017).
- The Station data file is a binary file and contains phase-cal information.

The raw MarkIV correlated data are complex numbers in delay space, while for astronomical VLBI analysis, the NRAO's Astronomical Image Processing System (AIPS; Fomalont, 1981) expects the data in the cross-spectral domain. In order to export the raw Mark IV correlator data into AIPS, the data are first fringe-fitted in FOURFIT (Cappallo, 2017). The cross-spectra output produced by FOURFIT is then read into AIPS using an interface program, called MK4IN (Alef & Graham, 2002), which is a direct Mark IV to AIPS interface. The MK4IN interface then reads the cross-spectra data, the FOURFIT solutions and the correlator model into AIPS and estimates the

antenna-based residuals from the baseline-based fringe fit results from FOURFIT. The data are then reformatted and written to a (u,v) -file. Finally, using the AIPS task FITAB, a FITS file is created.

3.4 Data reduction

Once the multi-source FITS file was loaded into AIPS, it was indexed and ordered into time baseline (TB) order. For the calibration, information such as observing frequency, participating stations as well as the observed source list and scan times were extracted from the AIPS multi-source file using suitable tasks. It should be noted that

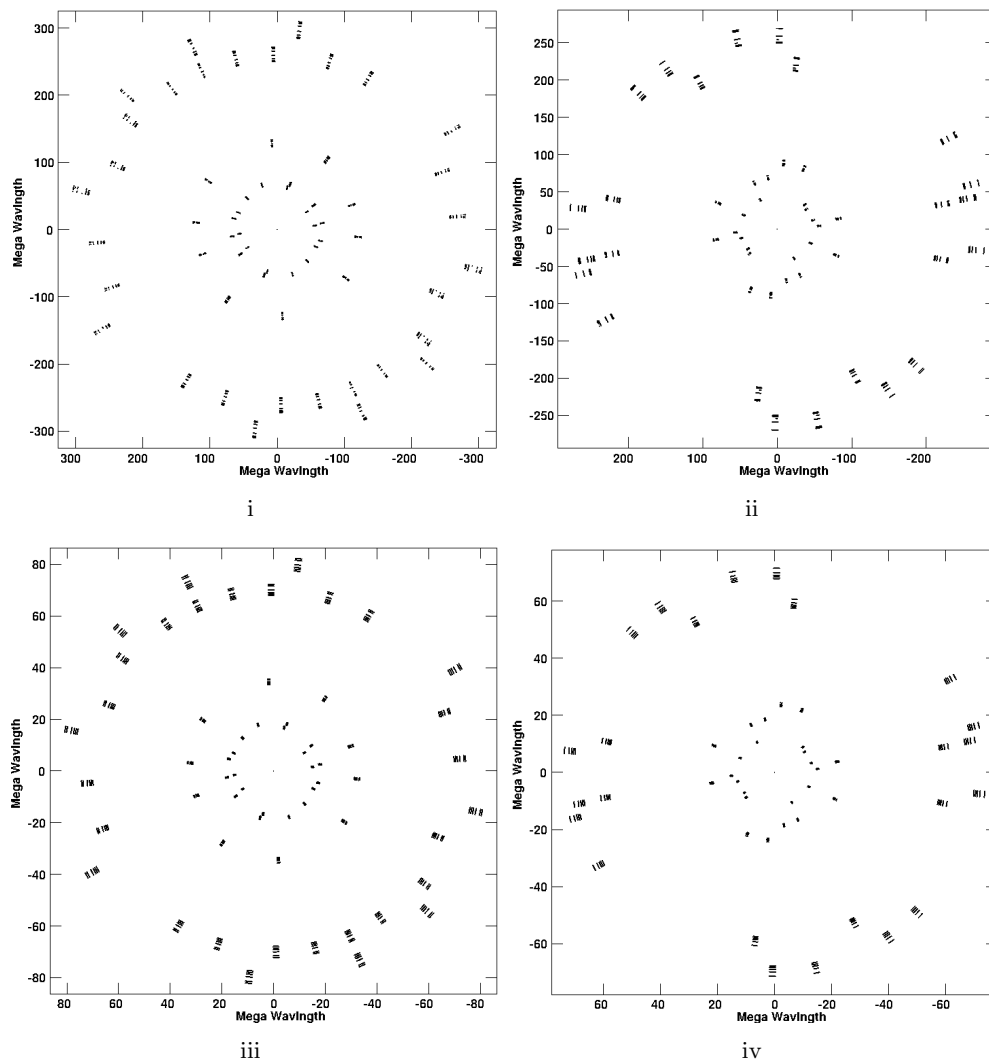


FIGURE 3.3: The (u,v) -coverage of source J0450-8101 from (i) CRDS-66, (ii) CRDS-68 at X-band and (iii) CRDS-66, (iv) CRDS-68 at S-band. The (u,v) -distance is in units of megalambda ($M\lambda$). The gap between the inner and outer shell is due to the absence of telescope between Australia and South Africa. In each plot, North is up indicating v and East is to the left indicating u .

the data reduction steps have been done by using respective tasks which are described in Chapter 9 of the AIPS Cookbook¹.

The data were examined for any sub-arraying problems, where one telescope points to source one and another telescope points to source two, at the same time. In order to correct the ionospheric dispersive delay, a global ionospheric model from GPS measurements was applied (Diamond et al., 2017). Such ionospheric models are available in the Crustal Dynamics Data Information System (CDDIS) archive. Tables with telescope system temperatures (T_{sys}) and antenna gain curves were generated and used to correct the visibility amplitudes. The T_{sys} values of each telescope were extracted from their corresponding log files to make a T_{sys} table. Time variable amplitude gains calculated from the system temperature and gain curve information, contained in the log files, were then applied to the visibility dataset to produce amplitude calibrated data. Unfortunately, T_{sys} measurements were not available for all the telescopes, in part because not all telescopes are capable of measuring T_{sys} - in such cases a nominal value for the T_{sys} or System Equivalent Flux Density (SEFD) was used instead.

The SEFD is a ratio of telescope system temperature (T_{sys}) to Degree Per Flux Unit (DPFU),

$$\text{SEFD} = \frac{T_{\text{sys}}}{\text{DPFU}}. \quad (3.1)$$

The DPFU is equal to $A_{\text{eff}}/2k$, where A_{eff} is the sensitivity of the telescope and k is the Boltzmann's constant (1.38×10^{-23} Jy K⁻¹) (Marr et al., 2016).

The nominal T_{sys} (K) and the SEFD (Jy) for each of the participating telescopes in the CRDS sessions, are listed in Table 3.4.

TABLE 3.4: The SEFD and T_{sys} values of the participating telescopes at S- and X-band in the CRDS sessions. The SEFD values are in Jy and T_{sys} values are in K. It should be noted that T_{sys} are not recorded for Warkworth, and a nominal SEFD was used (private communication with Dr Jamie McCallum, University of Tasmania).

Telescope name	Diameter (m)	SEFD (S-band)	T_{sys} (S-band)	SEFD (X-band)	T_{sys} (X-band)
HartRAO	26	1190	70	849	50
HartRAO	15	1050	55	1400	60
Hobart	26	640	95	560	75
Hobart	12	5000	120	4500	90
Katherine	12	5000	75	4000	80
Warkworth	12	5000	–	5000	–
Yarragadee	12	3500	120	3500	60

¹ <ftp://ftp.aoc.nrao.edu/pub/software/aips/TEXT/PUBL/COOKBOOK.PDF>

3.4.1 Fringe fitting: delay, rate and phase calibration

Fringe-fitting was used to determine the phase slopes, residual delays, and fringe rates in both time and frequency. The global fringe-fitting technique (AIPS task FRING), as described by Schwab & Cotton (1983), was used. Global fringe-fitting uses all baselines to jointly estimate the telescope phase, delay and rate relative to a reference telescope. The reference antenna should preferably be one that is there on all the scans, where the T_{sys} is well-behaved and which is sensitive and near centre of the array. Delay, rate and phase residuals for the reference telescope are set to zero. The delay, rate and phase residuals are stored in an AIPS table.

As a first step, fringe-fitting was used to calculate the relative delay between IFs, caused by different electronics in the different IFs. A good scan from the most compact and strongest source in the list was used for manual single-band calibration, to extract the relative delay between the IFs. At this stage, I did not solve for the rates, as the rates are usually independent of IF. The offsets in phase and delay between the IFs are assumed to be instrumental and remain constant over the observing run, and are therefore not dependent on the source being observed.

After the single-band delay calibration, fringe-fitting was used to solve for the multi-band delay or the time-variable part of the delay as well as the rate, which are IF independent. These time-dependent phase gradients are due to inaccuracies in the time delays that the correlator calculated for incoming wavefronts to each of the participating telescopes. Inaccuracies in the time delays are a result of propagation effects through the troposphere and ionosphere (at low frequencies), as well as the Earth's geometry. The multi-band delay solutions were smoothed in time and used to calibrate the visibilities. At this stage, editing of the visibility data was done using the approximate calibration from the multi-band delay fringe-fitting run. Finally, the multi-band delay fringe-fitting was run once more using the edited data to refine the delay and rate calibration. Since the fringe solutions are derived from the visibilities themselves, the visibility data for each source was in effect phase self-calibrated.

After the multi-band delay fringe-fitting, the visibility data were inspected to determine whether further amplitude and phase calibration were needed. To further improve the overall amplitude gains, two strong sources were selected and using the CLEAN images of each source as a model, antenna gains were determined that would make the visibility data for the selected sources as close as possible to a point source. At this point, the final calibrations were applied to the visibility data and the multi-source file was split into individual source files.

3.4.2 Imaging

A VLBI image is a representation of the brightness distribution of a source. The image construction of interferometric data makes use of the Fourier transform of the complex amplitude and phase in the (u,v) -plane.

The Difmap programme (Shepherd, 1997) which implements the hybrid mapping as described by Readhead & Wilkinson (1978); Cotton (1979), was employed. Difmap uses the CLEAN algorithm that starts by detecting the brightest point in the “dirty map”, shifting the “dirty beam” to this point, and scaling and subtracting the “dirty beam” from the visibility data through a number of iterations. At each step, the flux and position of the subtracted component are stored, until the residual map consists of noise only. Then the subtracted fluxes are convolved with the restoring beam and added back into the field of noise to produce a CLEAN image. Each source was phase self-calibrated using the CLEAN image as a model. Since there is no a priori phase calibration (as oppose to amplitude) and the raw phases are intrinsically ambiguous, the phase self-calibration is done first. The phase self-calibration was repeated until the process converged, and the derived gain corrections and the image did not change significantly between iterations. The amplitude self-calibration was then done to correct for amplitude errors, in this case specifically due to the use of nominal T_{sys} values for some of the telescopes. The advantage of self-calibration is that it reduces any false feature in the image and improves the image quality. During the CLEANing, the off-source RMS noise level was measured over the same region each time, as it can vary across the image. The off-source RMS noise level is an important quantity for determining the quality of a CLEAN image. The off-source RMS noise can be compared to the expected theoretical thermal noise and the image dynamic range (ratio of peak flux density to image RMS noise), and can be used to compare the CLEAN images before and after calibration. The CLEAN images of the sources from the CRDS sessions are presented in Chapter 4.

3.4.3 Model fitting

In addition to imaging, the AIPS task UVFIT was used to calculate the source position (x,y) , flux density and source full width half maximum (FWHM) size by fitting a circular Gaussian model by least-square fitting to the visibility data.

A circular Gaussian model was selected, as the limited (u,v) -coverage allows for only a small number of parameters to be calculated reliably. The reason behind this selection was to get a basic idea of the FWHM size, or the scale of the source structure.

Calculating measurement errors for the parameters of the model fitted VLBI data is a difficult task. There are, however, several ways in which to estimate the uncertainty for the FWHM size. There is the statistical uncertainty, which is calculated from the diagonal of the χ^2 covariance matrix from the model fitting, used under the assumption that the errors in the visibilities are independent and Gaussian-distributed and that the visibilities are perfectly calibrated. The assumption is generally not true, and the fit is expected to have telescope-based calibration errors. The fitted FWHM size can, therefore, be correlated with the telescope amplitude gain. Another approach is to estimate the FWHM uncertainties by re-running the model fitting (using UVFIT), but this time with the antenna amplitude gains as free parameters. This way, the uncertainty in the FWHM size is estimated considering the correlation between the telescope gain and the fitted FWHM size. The estimated statistical uncertainties from the model fitting were $\sim 10 - 15\%$ larger after adding the telescope gains as free parameters.

Source sizes smaller than the resolution can not be determined reliably. The minimum estimated source size depends on the SNR ratio of the observations. The minimum detectable source size in the visibility plane is given by Lovell et al. (2000) and is

$$a < \frac{2.4\sqrt{n/S}}{b}, \quad (3.2)$$

where a is the minimum source size (in mas) that can be measured, n is the integrated RMS noise of the observations, S is the flux density, and b is the maximum projected baseline length in units of $M\lambda$. Equation 3.2 becomes

$$a < 1.8\sqrt{n/S} \times \theta_{\text{beam}}, \quad (3.3)$$

when expressed using a uniformly weighted beam size $\theta_{\text{beam}} \approx 1.34 \times 10^8 \lambda/b$ mas.

To get a more realistic estimation of uncertainties, a Monte Carlo simulation was done as described in Petrov et al. (2019). In this simulation, the telescope gains were varied for a number of trials to fit the FWHM size. From these trials, a distribution of the fitted FWHM size was obtained. The estimated uncertainty of the fitted FWHM size was based on an assumption of 10% uncertainty in the telescope gains. For each of the sessions, the simulations were carried out for ten sources and ten trials per source. For this purpose, sources common to all sessions were selected. In each trial, the telescope gain was varied by a random number, with the mean of the telescope gain variation 0 and the standard deviation being 10%.

From the uncertainty estimations described above, the estimated uncertainties in the FWHM size from the Monte Carlo simulations were always $\leq a$ and a maximum uncertainty $\leq 1/4$ of the beam size was always obtained. Therefore, $1/4$ of the beam

size was used very conservatively as an estimation of uncertainty in source size for all the sources.

As the CRDS observations had poor (u,v) -coverage, the measurement of beam size is not always reliable for calculating the source size a . Therefore, the beam size was calculated as a geometric mean of the major and minor axes of the CLEAN beam.

Chapter 4

Results and Discussion

In this chapter, I present contour maps from the VLBI imaging as well as results from the astrometric quality assessment for all the sources, from all the selected CRDS sessions as presented in Chapter 3. Results from the data reduction and astrometric analysis for each of the sessions are presented first, followed by the tabulated results for each of the sources at both S- and X-band. The S- and X-band VLBI contour maps for each of the sources are then presented, and the chapter concludes with individual notes on each of the sources.

4.1 Astrometric quality assessment of the sources

In this section, I present the overall session-based results for all the CRDS sessions that were analysed. I present both the mean and median values for all the astrometric quality indicators: SI (Equation 2.19), SC (Equation 2.20), and the radial extents (Equation 2.21 and 2.22). The mean and median values for each session provide only an overall view of the sample of the sources observed in each session. The results for each source, and for all the selected CRDS sessions it was observed in, are presented individually in the table at the end of this section.

4.1.1 The CRDS-63 session

In the CRDS-63 session, a total of 38 ICRF-2 defining sources was observed, of which 22 sources were imaged at S-band and 33 sources were imaged at X-band. Due to poor (u, v) -coverage, from observations that included only two or three telescopes, it was not possible to image the remainder of the sources in this session. The mean and

median values of the SI, SC, and the R_w and $R_{95\%}$ of the sources are presented in Table 4.1.

TABLE 4.1: Mean and median of the SI, SC, R_w and $R_{95\%}$ of the sources at S- and X-band for CRDS-63.

	SI	SC	R_w	$R_{95\%}$
Mean (S-band)	1.29	0.82	2.78	5.50
Mean (X-band)	1.85	0.83	1.78	6.35
Median (S-band)	1.20	0.84	2.72	4.18
Median (X-band)	1.75	0.84	1.61	6.83

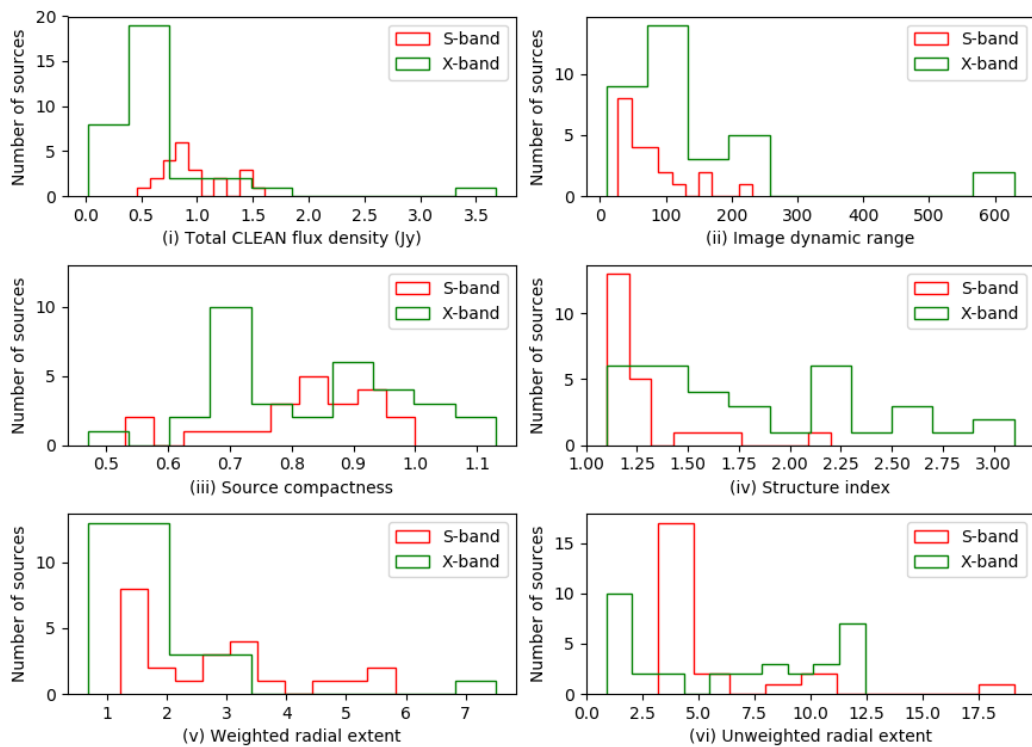


FIGURE 4.1: Distribution of the CRDS-63 sources imaged at S- and X-band using (i) total CLEAN flux density, (ii) image dynamic range, (iii) SC, (iv) SI, (v) R_w , and (vi) $R_{95\%}$. The S-band is indicated by red and X-band is indicated by green colour.

Histograms of the total CLEAN flux density, image dynamic range, SC, SI, and the R_w and $R_{95\%}$ of the sources at S- and X-band are presented in Figure 4.1. The mean of the image RMS at S- and X-band are $15.34 \text{ mJy beam}^{-1}$ and $6.55 \text{ mJy beam}^{-1}$ respectively, and the median of the image RMS are $14.12 \text{ mJy beam}^{-1}$ and $5.18 \text{ mJy beam}^{-1}$ respectively. At S-band, the mean and median of the image dynamic range are 77 and 64 respectively, and at X-band, they are 139 and 96 respectively. The results for each individual source are presented in Table 4.5.

4.1.2 The CRDS-66 session

A total of 38 ICRF-2 defining sources was observed. A total of 16 sources from the S-band and 13 sources from the X-band data were imaged. Imaging for the remainder of the sources was not possible, due to the fact that data from only two or three telescopes were recorded.

The mean and median values of the SI, SC, and the R_w and $R_{95\%}$ of the sources are presented in Table 4.2. Histograms of the total CLEAN flux density, image dynamic range, SC, SI, R_w and $R_{95\%}$ of the sources at S- and X-band are presented in Figure 4.2.

TABLE 4.2: Mean and median of the SI, SC, R_w and $R_{95\%}$ of the sources at S- and X-band, for the CRDS-66 session.

	SI	SC	R_w	$R_{95\%}$
Mean (S-band)	1.94	0.61	1.87	4.76
Mean (X-band)	1.52	0.88	1.14	3.57
Median (S-band)	1.40	0.64	1.62	4.05
Median (X-band)	1.30	0.95	1.08	1.89

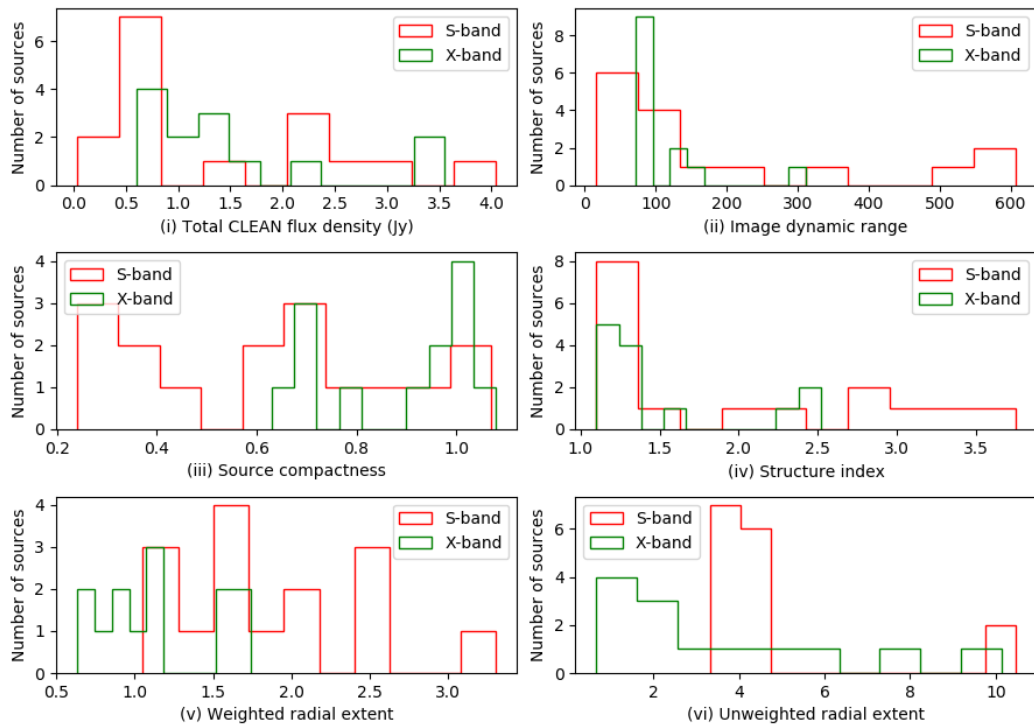


FIGURE 4.2: Distribution of the CRDS-66 sources imaged at S- and X-band using (i) total CLEAN flux density, (ii) image dynamic range, (iii) SC, (iv) SI, (v) R_w , and (vi) $R_{95\%}$. The S-band is indicated by red and X-band is indicated by green colour.

At S-band, the mean and median values of the image RMS are $11.54 \text{ mJy beam}^{-1}$, and $8.23 \text{ mJy beam}^{-1}$ respectively. The mean and median of the image dynamic range are 184 and 103, respectively. The mean and median of the image RMS at X-band are $14.17 \text{ mJy beam}^{-1}$ and $13.27 \text{ mJy beam}^{-1}$ respectively. The mean and median of the image dynamic range at X-band are 113 and 87 respectively. In Table 4.5, imaging results are presented in detail.

4.1.3 The CRDS-68 session

In the CRDS-68 session at X-band, out of the 38 observed sources, 37 sources were imaged. It should be noted that the same set of sources was observed in both CRDS-66 and CRDS-68. The mean and median of the SI, SC, and the R_w and $R_{95\%}$ are presented in Table 4.3.

TABLE 4.3: The mean and median of SI, SC, the R_w and $R_{95\%}$ at X-band, for the CRDS-68 session.

	SI	SC	R_w	$R_{95\%}$
Mean	1.79	0.74	1.94	7.06
Median	1.40	0.75	1.65	7.25

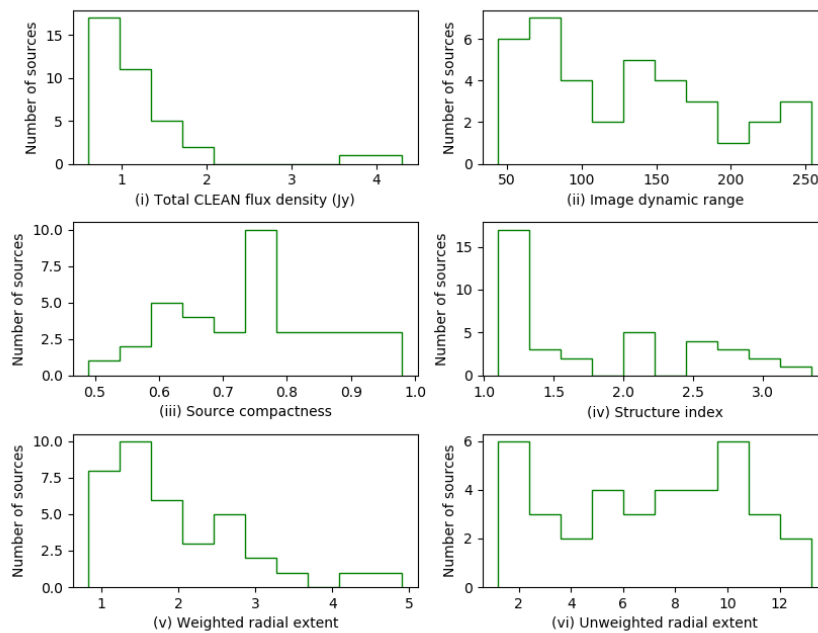


FIGURE 4.3: Distribution of the CRDS-68 sources using (i) total CLEAN flux density, (ii) image dynamic range, (iii) SC, (iv) SI, (v) R_w , and (vi) $R_{95\%}$.

The mean and the median of the image RMS and image dynamic range are 11.42 mJy beam⁻¹, and 9.68 mJy beam⁻¹ and 128 and 125, respectively. The distribution of the sources with total CLEAN flux density, image dynamic range, SC and SI is presented in Figure 4.3 using histogram plots. Imaging parameters for individual sources are listed in Table 4.5.

4.1.4 The CRDS-94 session

In the CRDS-94 session, the number of observed sources is 51. New sources were included in the schedule, and analysis from this session were used in selecting defining sources in the ICRF-3.

A total of 36 sources was imaged at S-band and a total of 20 sources were imaged at X-band. The remainder of the sources had data from only two or three telescopes, and imaging was not possible. The mean and median values of SI, SC, and the R_w and $R_{95\%}$ of the sources at S- and X-band are presented in Table 4.4.

TABLE 4.4: Mean and median values of the SI, SC, R_w and $R_{95\%}$ of the sources which were imaged at S- and X-band in the CRDS-94 session.

	SI	SC	R_w	$R_{95\%}$
Mean (S-band)	1.64	0.92	3.36	8.14
Mean (X-band)	2.13	0.89	1.28	2.96
Median (S-band)	1.60	0.92	3.13	4.36
Median (X-band)	2.15	0.93	0.97	2.05

The mean and median values of image RMS are 11.20 mJy beam⁻¹, and 10.61 mJy beam⁻¹ and 12.34 mJy beam⁻¹, and 12.17 mJy beam⁻¹ at S- and X-band respectively. At S-band, the mean image dynamic range is 122 and at X-band, it is 166. The median values of image dynamic range at S- and X-band are 100 and 147 respectively. It is evident that the image dynamic range was improved in the CRDS-94 compared to the previous CRDS sessions. The distribution of total CLEAN flux density, image dynamic range, SC, SI, and R_w and $R_{95\%}$ of the sources are presented in Figure 4.4. The imaging parameters of the sources are presented in Table 4.5.

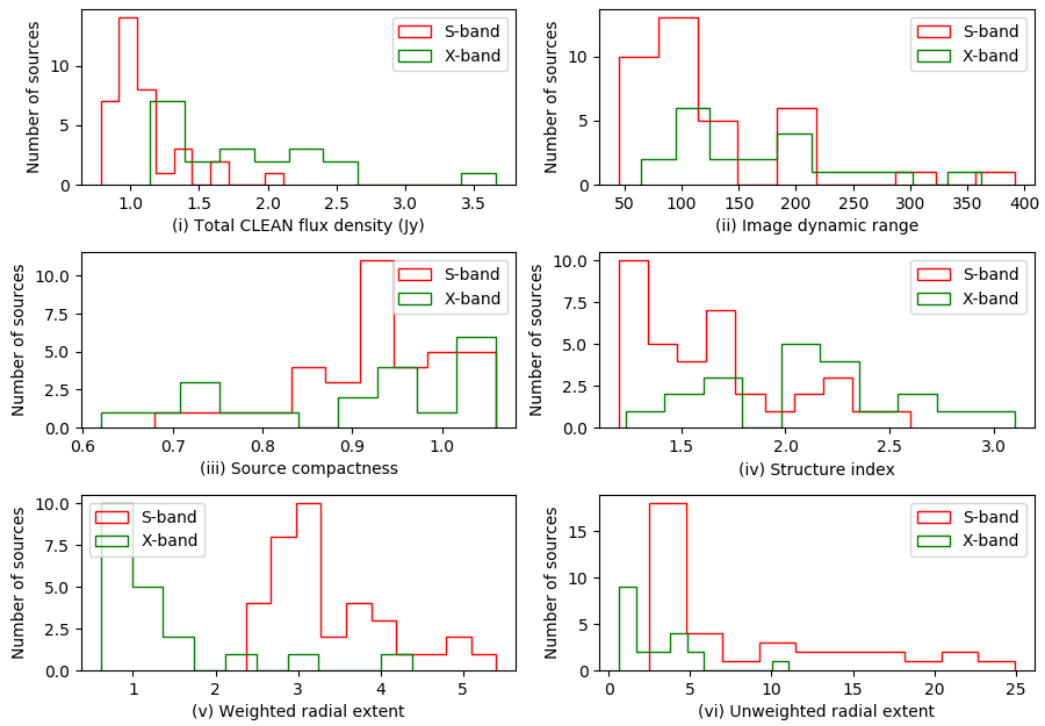


FIGURE 4.4: Distribution of the sources in the CRDS-94 session using (i) total CLEAN flux density, (ii) image dynamic range, (iii) SC, (iv) SI, (v) R_w , and (vi) $R_{95\%}$.

TABLE 4.5: Results of estimated total CLEAN flux density, S_{cc} , image RMS, S_{core} (flux density from the circular Gaussian fit), FWHM size, SC, SI, R_w and $R_{95\%}$ from CRDS S- and X-band observations. The source names are in J2000 coordinates. The estimated uncertainties on the flux densities are 10%. Fitted FWHM sizes are given with either 1σ uncertainty, or the 3σ upper limit. It should be noted that the column ‘‘Observing band’’ indicates S- and X-band along with the CRDS session number, for example, 68 (X) indicates X-band observations in the CRDS-68 session and 94 (S) indicates S-band observations in the CRDS-94 session.

Source name	Observing band	Total CLEAN flux (Jy)	S_{cc} (Jy beam $^{-1}$)	Image RMS (mJy beam $^{-1}$)	S_{core} (Jy)	FWHM size (mas)	SC	SI	R_w (mas)	$R_{95\%}$ (mas)
J0004-4736	68 (X)	0.853	0.635	6.09	0.650	6.89 \pm 2.98	0.74	3.10	1.41	9.41
J0040-5903	94 (S)	0.986	0.917	8.25	0.901	11.89 \pm 3.45	0.93	1.75	3.74	11.39
J0051-4226	63 (S)	0.826	0.817	13.06	0.748	13.56 \pm 3.45	0.98	1.75	2.49	3.37
	63 (X)	0.400	0.336	7.40	0.356	3.54 \pm 1.65	0.84	2.10	2.29	11.57
J0106-4034	68 (X)	1.097	0.920	5.16	1.097	9.03 \pm 2.10	0.83	2.65	1.20	1.71
J0109-6049	63 (X)	0.339	0.250	4.41	0.298	4.65 \pm 1.50	0.73	2.30	1.29	1.89
J0133-5200	66 (X)	0.602	0.656	8.35	0.602	2.89 \pm 1.34	1.08	1.25	0.67	0.85
	68 (X)	1.151	0.775	6.31	1.151	10.67 \pm 3.20	0.67	2.20	2.49	7.97
J0229-7847	63 (S)	0.929	0.700	12.15	0.929	11.43 \pm 4.31	0.75	1.60	1.22	3.21
	63 (X)	0.527	0.374	4.66	0.527	4.55 \pm 1.05	0.70	1.75	1.61	7.77
J0236-6136	68 (X)	0.606	0.598	9.68	0.600	8.56 \pm 2.57	0.98	1.65	1.00	1.76
J0253-5441	94 (S)	1.645	1.442	7.92	1.645	13.67 \pm 4.67	0.87	1.30	3.28	3.97
J0303-6211	63 (S)	1.437	0.954	13.79	1.572	20.5 \pm 3.48	0.66	1.20	3.82	3.94
	63 (X)	0.637	0.420	7.95	0.503	5.78 \pm 1.78	0.65	1.95	2.02	11.20

Continued on next page

Table 4.5 – Continued from previous page

J0309-6058	66 (S)	1.61	1.455	11.64	1.455	13.65 ± 3.89	0.90	1.30	2.31	6.41
	68 (X)	1.305	0.824	27.45	1.305	7.93 ± 3.81	0.63	1.23	2.46	7.09
J0334-4008	63 (S)	1.419	1.269	12.49	1.419	34.78 ± 3.7	0.89	1.20	1.91	3.61
	63 (X)	1.525	1.491	20.22	1.525	7.89 ± 1.45	0.97	1.23	1.08	3.50
J0335-5430	94 (S)	0.917	0.906	10.54	0.863	10.55 ± 3.78	0.98	1.75	3.04	3.14
	66 (X)	0.686	0.529	4.59	0.706	3.41 ± 1.78	0.77	1.60	1.74	10.13
	68 (X)	0.881	0.855	13.36	0.400	3.78 ± 2.36	0.97	1.20	1.31	1.83
J0403-3605	63 (S)	0.786	0.671	10.76	0.786	10.2 ± 2.89	0.85	1.30	5.82	19.06
	63 (X)	1.317	1.299	5.18	1.317	4.24 ± 1.60	0.98	2.20	1.56	5.90
J0406-3826	66 (X)	1.376	0.941	11.07	1.116	8.91 ± 1.33	0.68	2.35	1.57	4.05
	68 (X)	1.591	1.088	6.26	0.891	5.82 ± 2.89	0.68	3.35	1.65	4.90
J0439-4522	63 (X)	0.673	0.497	4.13	0.551	6.09 ± 1.34	0.73	2.35	2.01	5.78
J0450-8101	66 (S)	2.239	0.963	10.92	2.269	12.89 ± 3.91	0.43	1.35	1.17	4.25
	66 (X)	1.577	1.587	17.11	1.570	3.21 ± 1.37	1.00	1.32	0.63	0.67
	68 (X)	1.397	1.340	20.59	1.329	8.93 ± 2.1	0.95	1.23	0.93	1.20
J0506-6109	63 (S)	0.639	0.528	8.78	0.638	19.51 ± 3.40	0.82	1.21	5.42	10.31
	63 (X)	0.422	0.310	5.23	0.422	8.90 ± 1.45	0.73	1.45	2.77	12.41
J0516-6207	66 (S)	2.737	0.668	4.51	2.725	18.01 ± 4.90	0.24	2.75	2.17	4.55
	66 (X)	1.343	1.371	15.79	1.340	7.61 ± 1.45	1.02	1.10	0.77	0.90

Continued on next page

Table 4.5 – Continued from previous page

J0525-4557	68 (X)	0.710	0.573	9.32	0.650	3.67± 2.34	0.80	2.75	0.83	1.40
J0526-4830	63 (S)	0.781	0.607	25.12	0.781	21.76± 3.59	0.77	1.10	1.27	4.21
	63 (X)	0.428	0.381	4.42	0.428	7.39± 1.50	0.89	1.60	2.01	10.06
J0534-6106	68 (X)	0.861	0.619	13.19	0.397	4.76± 2.01	0.71	1.10	2.03	8.77
J0536-3401	63 (X)	0.309	0.326	5.77	0.309	5.43± 1.40	1.05	1.40	1.41	3.80
J0538-4405	66 (S)	4.045	2.578	35.78	3.693	14.32± 8.91	0.63	1.10	1.40	4.20
	66 (X)	3.397	2.430	24.08	3.057	4.61± 1.34	0.71	2.45	0.95	1.56
	68 (X)	0.861	0.619	13.19	0.397	4.76± 2.01	0.71	1.10	2.03	8.77
J0550-5732	63 (S)	0.836	0.456	14.75	0.679	10.43± 2.87	0.54	1.20	1.54	4.23
	94 (S)	1.067	1.014	11.81	0.945	13.87± 3.01	0.95	1.60	2.81	3.49
	63 (X)	0.572	0.380	5.63	0.435	6.34± 1.56	0.66	2.52	2.09	6.83
J0922-3959	66 (X)	1.219	0.863	13.27	1.219	5.89± 1.80	0.70	1.30	1.70	8.13
	68 (X)	1.191	0.916	18.49	1.191	3.56± 1.89	0.76	1.40	1.26	4.11
J0930-8533	94 (S)	1.076	0.996	10.40	1.071	12.67± 3.88	0.92	1.40	3.13	3.85
J1006-5018	63 (X)	0.653	0.623	2.78	0.628	9.45± 3.40	0.95	1.45	1.12	1.16
J1014-4508	94 (S)	1.400	1.257	12.59	1.119	11.22± 3.82	0.89	1.52	4.51	19.56
	94 (X)	1.328	1.202	8.55	1.324	5.89± 1.56	0.90	2.40	1.02	1.44
J1023-6646	94 (S)	0.946	0.908	16.80	0.890	18.78± 7.39	0.95	1.20	4.33	24.92
	66 (X)	0.792	0.747	10.63	0.792	9.03± 1.62	0.94	1.10	1.14	3.38

Continued on next page

Table 4.5 – Continued from previous page

	68 (X)	1.005	0.911	7.27	1.000	4.78± 2.45	0.90	2.10	1.20	7.11
J1036-3744	63 (X)	0.519	0.464	2.53	0.518	3.45± 1.39	0.89	1.52	0.87	1.11
J1041-4740	94 (S)	1.016	0.939	9.63	0.980	10.38± 3.78	0.92	1.30	4.14	16.33
	94 (X)	2.195	1.552	10.97	2.194	4.89± 1.67	0.70	1.75	1.00	1.02
J1047-6217	94 (S)	1.154	1.020	19.32	1.135	14.78± 3.08	0.88	2.95	2.94	4.76
	94 (X)	2.443	1.897	11.33	1.907	3.90± 1.45	0.77	1.23	1.14	5.83
J1103-5357	94 (S)	0.876	0.886	4.47	0.827	11.67± 3.11	1.01	1.60	2.78	2.90
	68 (X)	0.845	0.653	5.96	0.423	6.93± 2.91	0.77	1.60	1.48	5.68
J1118-4638	94 (S)	0.986	0.901	13.38	0.959	11.7± 3.80	0.91	1.20	3.80	12.49
	94 (X)	1.757	1.699	14.70	1.757	8.61± 1.92	0.96	2.10	0.77	1.57
J1131-5818	94 (S)	0.951	0.892	4.96	0.908	12.83± 3.88	0.93	1.30	2.82	3.44
	94 (X)	2.429	1.774	6.71	2.429	3.91± 1.92	0.73	2.60	0.95	4.45
J1145-6954	63 (S)	0.463	0.249	14.46	0.500	12.93± 3.86	0.53	2.20	1.53	5.26
	94 (S)	0.827	0.833	14.22	0.599	11.82± 3.02	1.00	1.60	2.72	3.16
	63 (X)	0.420	0.301	3.39	0.398	2.67 ± 1.51	0.71	1.25	1.88	9.83
J1147-3812	66 (S)	2.842	1.08	8.91	2.929	10.78± 3.88	0.38	1.20	1.59	3.72
	66 (X)	2.309	2.270	29.02	2.182	4.93± 1.82	0.98	1.15	0.99	1.77
	68 (X)	3.876	3.555	16.31	3.637	9.56± 2.34	0.91	2.20	1.01	1.24
J1151-6728	94 (S)	1.375	1.019	14.00	1.364	14.28± 3.22	0.74	1.30	4.85	15.68

Continued on next page

Table 4.5 – *Continued from previous page*

	94 (X)	1.145	1.098	5.73	1.112	4.67± 1.02	0.95	2.10	3.09	3.59
J1254-7138	68 (X)	0.948	0.715	14.72	0.948	8.67± 2.01	0.75	1.10	1.58	7.25
J1316-3338	63 (S)	0.752	0.709	14.67	0.727	8.90± 3.45	0.94	1.20	1.31	4.18
	63 (X)	0.475	0.376	4.22	0.475	2.61± 1.90	0.79	2.30	0.98	1.12
J1326-5256	94 (S)	1.151	1.048	6.00	1.103	11.50± 3.18	0.91	1.70	3.07	4.76
	94 (X)	1.145	1.098	5.73	1.112	4.67± 1.02	0.95	2.10	3.09	3.59
J1329-5608	68 (X)	0.765	0.662	5.07	0.561	5.89± 2.78	0.86	1.23	1.61	5.68
J1352-4412	63 (X)	0.415	0.303	3.65	0.388	3.78± 1.56	0.73	3.10	2.09	10.35
J1424-6807	94 (S)	0.938	0.938	11.31	0.498	9.30± 3.99	1.00	1.35	2.49	3.22
	66 (X)	1.168	1.113	13.36	1.185	7.39± 1.62	0.95	1.20	1.11	5.34
	68 (X)	1.607	0.962	15.85	0.814	9.38± 2.84	0.59	2.60	2.55	11.51
	94 (X)	1.821	1.474	9.76	0.747	3.91± 1.67	0.80	1.75	0.87	3.35
J1427-4206	63 (S)	1.609	1.524	19.72	1.609	28.51± 4.01	0.94	1.20	3.50	4.09
	63 (X)	3.674	3.298	6.24	3.670	9.78± 1.67	0.89	2.70	1.37	7.92
J1452-6502	68 (X)	0.741	0.585	16.86	0.590	5.93± 2.00	0.78	1.10	1.21	4.14
J1454-4012	63 (X)	0.341	0.342	9.07	0.341	7.60± 1.45	1.00	1.60	1.34	2.09
J1514-4748	94 (S)	1.005	1.001	10.40	0.948	11.67± 3.20	0.99	1.25	2.78	3.11
	94 (X)	2.088	2.135	10.43	2.088	8.45± 2.67	1.02	1.60	0.73	0.77

Continued on next page

Table 4.5 – Continued from previous page

J1558-6432	68 (X)	0.984	0.641	6.09	0.640	8.81± 2.34	0.65	1.20	2.53	8.31
J1616-7108	68 (X)	0.924	0.565	3.99	0.500	11.23± 3.56	0.61	2.80	2.97	11.97
J1624-6809	63 (S)	1.183	1.061	26.17	1.271	10.46± 3.6	0.89	1.30	2.94	3.70
	94 (S)	2.111	1.611	14.23	1.232	10.39± 3.29	0.76	1.78	3.13	9.97
	63 (X)	0.458	0.396	14.98	0.420	1.67± 1.12	0.86	1.10	1.19	2.99
	94 (X)	1.411	1.276	15.25	1.410	3.63± 1.83	0.90	2.30	1.69	11.05
J1628-6152	94 (S)	0.948	0.867	11.23	0.910	11.90± 3.78	0.91	1.34	3.91	16.47
	68 (X)	1.226	0.912	8.69	0.693	9.45± 2.54	0.74	1.14	2.62	9.50
	94 (X)	1.411	1.276	15.25	1.410	3.63± 1.83	0.90	2.30	1.69	11.05
J1650-5044	94 (X)	3.663	2.698	14.79	3.500	3.92± 1.10	0.73	2.17	0.84	1.83
J1701-5621	66 (S)	0.725	0.251	6.74	0.700	13.42± 7.81	0.34	3.35	1.05	3.53
	94 (S)	1.668	1.143	8.78	1.536	13.82± 3.88	0.68	2.20	2.91	3.06
	68 (X)	1.279	0.627	10.17	1.307	8.37± 2.77	0.49	1.23	4.91	12.96
	94 (X)	2.137	1.335	16.87	1.204	3.83± 1.02	0.62	2.70	1.51	4.86
J1703-6212	94 (S)	0.982	0.900	13.86	0.433	11.39± 3.27	0.91	1.67	2.37	3.62
	63 (X)	0.485	0.378	4.91	0.497	3.67± 1.67	0.77	1.20	2.76	12.35
	94 (X)	1.644	1.678	14.78	0.961	4.89± 1.89	1.02	2.18	0.61	0.64
J1733-7935	68 (X)	0.903	0.672	4.53	0.506	5.87± 2.32	0.74	2.60	1.84	6.81
J1803-6507	63 (S)	0.807	0.640	22.16	0.806	9.53± 3.40	0.79	1.10	1.34	4.40

Continued on next page

Table 4.5 – Continued from previous page

	63 (X)	0.439	0.425	5.27	0.439	2.78±1.34	0.96	2.10	1.83	10.16
J1809-4552	66 (S)	0.484	0.338	15.4	0.484	9.81± 5.61	0.69	2.10	1.24	10.07
	68 (X)	0.820	0.637	9.52	0.504	6.91±2.72	0.77	1.30	2.05	10.48
J1819-5521	63 (S)	0.841	0.600	22.48	0.840	14.7±3.20	0.71	1.15	1.53	4.74
	94 (S)	0.997	0.920	8.82	0.561	11.45±3.45	0.92	1.45	3.26	4.85
	63 (X)	0.450	0.335	5.76	0.469	2.56±1.76	0.74	1.75	1.79	11.44
J1829-5813	66 (S)	0.419	0.389	7.55	0.419	11.67±7.01	0.92	2.75	3.31	3.61
	68 (X)	0.859	0.732	11.67	0.634	9.47±2.01	0.85	1.30	1.49	9.10
J1837-7108	63 (S)	0.839	0.721	12.68	0.839	11.29±4.50	0.84	1.12	2.72	3.84
	94 (S)	1.103	0.942	13.95	1.068	12.45±3.20	0.85	1.20	5.40	21.57
	63 (X)	0.355	0.333	7.11	0.355	5.68±1.45	0.93	1.60	0.74	0.95
	94 (X)	2.300	2.352	18.90	2.300	3.93±1.79	1.02	2.16	0.62	0.63
J1857-5325	94 (S)	0.883	0.913	7.65	0.629	10.36±2.88	1.03	1.29	3.02	3.16
J1930-6056	66 (S)	0.684	0.455	6.91	0.663	20.75±3.45	0.66	1.45	2.50	10.46
	94 (S)	1.119	1.045	24.75	0.889	11.45±3.40	0.93	1.34	3.64	11.53
	68 (X)	1.113	0.625	6.83	0.858	7.45±2.66	0.56	3.10	2.16	10.51
J1933-6942	94 (S)	0.975	0.957	9.17	0.960	12.34±3.45	0.98	2.23	2.47	2.49
J1937-3958	63 (S)	0.780	0.697	5.07	0.765	10.52±3.61	0.89	1.23	5.34	10.34
	63 (X)	0.816	0.720	4.54	0.816	7.01±1.91	0.88	3.02	1.05	1.42

Continued on next page

Table 4.5 – Continued from previous page

J1940-6907	66 (S)	0.699	0.418	17.33	0.575	19.61±3.44	0.59	2.20	2.56	4.05
	68 (X)	0.980	0.579	12.24	1.000	7.45±3.88	0.59	2.70	2.76	11.94
J1941-6211	94 (S)	1.120	0.960	18.83	1.000	11.34±2.89	0.85	2.10	4.95	22.47
J1955-6115	94 (S)	1.039	0.951	4.79	1.000	13.56±2.50	0.91	1.65	3.37	9.97
J1957-3845	63 (S)	1.182	0.994	5.11	1.088	23.71±3.44	0.84	1.17	3.24	3.97
	63 (X)	0.768	0.548	3.67	0.851	1.09±1.31	0.71	2.65	1.07	1.29
J2005-3723	66 (S)	0.454	0.489	14.37	0.401	17.40±3.46	1.07	1.20	1.81	3.45
	68 (X)	0.874	0.635	5.56	0.503	7.93±2.43	0.72	2.10	1.57	4.91
J2035-6846	94 (S)	0.881	0.925	10.69	0.784	10.38±2.38	1.04	1.67	2.52	2.79
	94 (X)	1.650	1.238	13.34	1.649	4.93±1.43	0.75	2.80	1.01	3.99
J2056-4714	63 (S)	1.388	1.300	9.18	1.388	18.40±4.51	0.93	1.25	3.25	3.40
	63 (X)	1.139	0.834	1.81	1.139	6.78±1.59	0.73	2.10	1.96	11.73
J2109-4110	66 (S)	0.032	0.022	1.96	0.022	13.70±3.01	0.68	1.10	1.56	3.96
	68 (X)	0.874	0.635	5.56	0.503	7.93±2.43	0.72	2.10	1.57	4.91
J2126-4605	94 (S)	0.784	0.836	8.03	0.769	18.45±2.77	1.06	1.70	3.14	3.19
	63 (X)	0.270	0.307	27.82	0.270	9.01±1.78	1.13	1.30	0.78	0.89
J2147-7536	66 (S)	2.164	0.607	3.85	2.150	9.62±2.91	0.28	3.20	1.62	4.40
	66 (X)	3.549	2.254	11.39	2.515	9.03±1.52	0.63	2.52	1.56	5.94
	68 (X)	2.076	1.897	22.93	2.086	3.91±2.88	0.91	1.10	0.93	2.49

Continued on next page

Table 4.5 – Continued from previous page

J2207-5346	63 (S)	0.922	0.763	19.53	0.922	21.4±2.90	0.82	1.15	1.73	4.05
	94 (S)	1.266	1.124	3.97	1.078	11.45±3.56	0.88	2.10	3.08	5.05
	63 (X)	0.740	0.543	5.10	0.740	3.23±1.51	0.73	2.65	1.80	7.86
	94 (X)	1.374	1.285	4.70	1.374	5.80±1.56	0.93	3.10	1.20	4.57
J2223-3455	94 (S)	0.905	0.900	7.75	0.628	10.38±3.76	0.99	2.30	3.26	3.64
	68 (X)	0.794	0.612	5.45	0.500	9.45±2.22	0.77	1.20	1.83	8.04
J2235-4835	63 (S)	0.938	0.945	10.25	0.938	10.83±4.56	1.00	1.27	3.22	3.54
	63 (X)	0.444	0.494	8.03	0.444	4.62±1.67	1.11	1.75	0.68	0.94
J2239-5701	66 (S)	0.510	0.385	28.58	0.330	18.24±4.51	0.75	1.10	2.04	4.20
	94 (S)	0.916	0.952	12.98	0.900	10.48±3.65	1.03	1.23	2.97	3.47
	66 (X)	1.174	1.194	15.66	1.060	8.39±2.01	1.01	1.20	1.08	1.84
	68 (X)	1.389	1.113	13.18	1.118	4.83±2.44	0.80	1.10	1.30	3.25
	94 (X)	1.322	1.412	8.06	1.377	3.09±1.3	1.06	1.75	0.75	0.87
J2247-3657	63 (X)	0.379	0.351	9.40	0.378	5.78±1.7	0.92	1.23	3.05	11.47
J2248-3235	66 (S)	0.506	0.540	6.26	0.409	12.04±6.81	1.06	1.25	2.62	3.33
	66 (X)	0.864	0.881	9.97	0.814	5.89±1.34	1.01	1.34	0.96	1.89
	68 (X)	1.023	0.882	5.89	0.602	7.92±2.86	0.86	1.34	1.71	10.20
J2303-6807	63 (S)	0.814	0.637	29.85	0.787	11.03±1.03	0.78	1.14	1.29	5.84
J2329-4730	66 (S)	2.062	0.609	3.95	2.051	10.28±3.05	0.29	3.75	1.52	3.62

Continued on next page

Table 4.5 – Continued from previous page

	68 (X)	1.693	0.975	6.79	1.693	8.56±2.84	0.57	1.15	4.11	13.23
J2336-4115	63 (X)	0.023	0.011	0.09	0.022	2.01±1.41	0.47	1.40	7.50	7.82
	94 (X)	1.195	1.234	18.45	0.729	4.98±1.48	1.03	1.60	2.12	2.28
J2336-5236	94 (S)	1.442	1.157	11.61	1.442	11.89±3.02	0.81	2.33	3.67	8.08
J2347-5110	94 (S)	1.017	0.872	2.60	0.874	10.39±3.89	0.85	2.60	3.99	14.33
	68 (X)	0.847	0.563	14.16	0.374	6.49±2.03	0.66	1.25	3.42	9.74
J2356-6820	63 (X)	0.623	0.432	6.86	0.610	3.89±1.49	0.69	1.20	1.64	12.03
J2357-5311	94 (S)	1.137	1.173	23.66	1.137	12.67±3.45	1.03	1.80	2.98	3.23
	68 (X)	2.064	1.231	11.83	2.064	7.90±2.45	0.59	2.10	2.88	10.71
	94 (X)	2.380	2.220	21.85	2.380	5.92±2.67	0.93	2.20	0.81	1.24
J2359-3133	63 (S)	0.612	0.574	15.43	0.600	14.81±3.45	0.93	1.45	4.57	9.11
	63 (X)	0.275	0.288	4.07	0.277	8.94±2.30	1.04	1.45	1.11	1.95

4.2 Spectral index distribution

The mechanism of emission from quasars and the role of spectral index in understanding the physical characteristics of a source have been discussed in Chapter 2. In this section, the spectral indices of the sources from the CRDS sessions are presented. The spectral index is defined as α , which is the slope of flux density against frequency in log-log space, and is

$$\alpha = \frac{\log\left(\frac{s_X}{s_S}\right)}{\log\left(\frac{\nu_X}{\nu_S}\right)}, \quad (4.1)$$

where s_X and s_S are the source flux densities at X- and S-band, respectively. In the denominator, ν_X and ν_S are the X- and S-band frequencies. The parameter α was derived from the measured flux densities at S- and X-band. A distribution of α in the range of -0.9 to 0.6 was obtained.

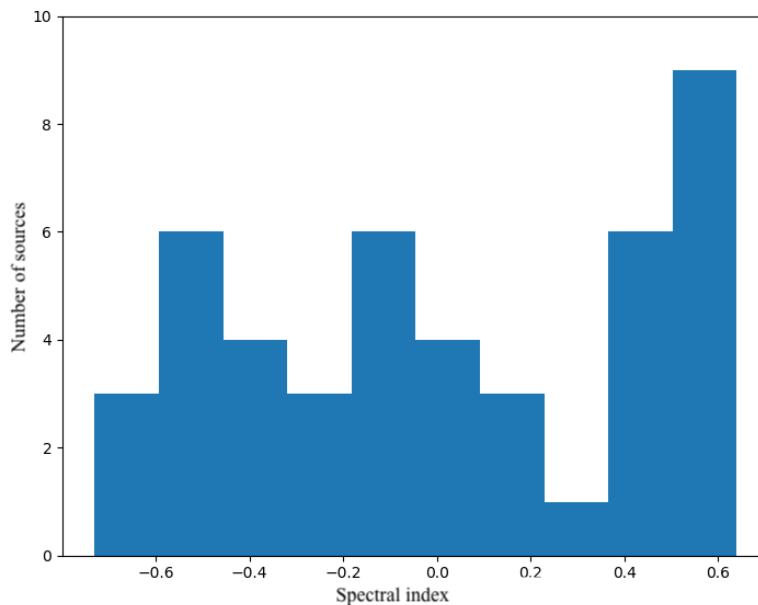


FIGURE 4.5: The distribution of spectral index of the sources from the four CRDS sessions.

4.3 Modulation index

As an indicator of source variability, I also calculated the parameter μ (Equation 2.23) of the sources using the S- and X-band flux densities. A higher value of μ may indicate a possible source evolution and the presence of jet components. Flux densities from the CRDS sessions presented in this work, together with flux densities from the Goddard Space Flight Center (GSFC) server¹ (since 2000), were used to calculate the μ .

¹lupus.gsfc.nasa.gov/sess/sessions/cumulative/source_perf/

The flux densities obtained from the GSFC server were all obtained from IVS sessions. The distribution of S- and X-band sources with μ is presented in Figure 4.6, and the individual S- and X-band indices are presented in Table 4.6.

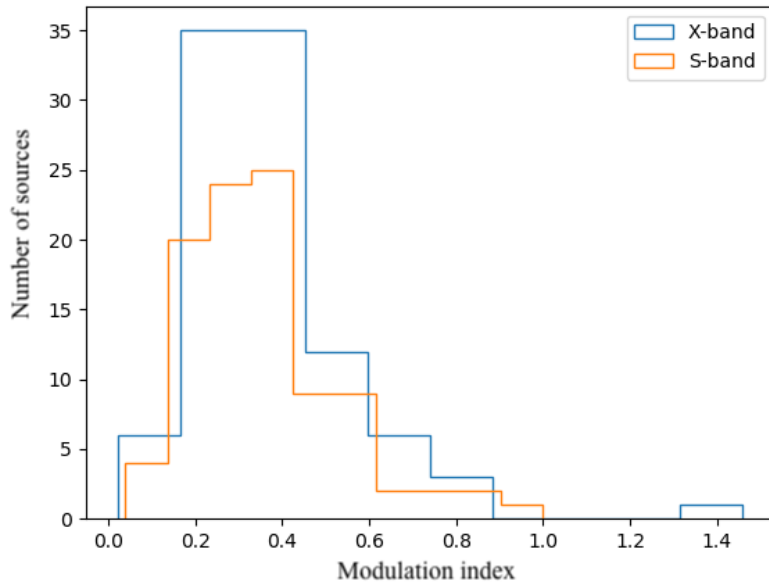


FIGURE 4.6: Distribution of modulation index for the sources observed in CRDS-63, -66, -68 and -94 sessions. Flux densities were obtained from the GSFC server.

TABLE 4.6: Results from the analysis of the μ of 103 sources observed in the CRDS sessions. The table uses data from the GSFC server using all IVS sessions (including CRDS sessions) since 2000. Flux densities are taken from geodetic VLBI sessions conducted by the IVS. In the list, source names are in J2000 coordinates, \bar{s}_S and \bar{s}_X are the mean of total flux densities, σ_S and σ_X are the RMS of the total flux densities and μ_S and μ_X are the modulation indices at S- and X-band, respectively.

Source name	Number of epochs	\bar{s}_X	σ_X	μ_X	\bar{s}_S	σ_S	μ_S
J0004-4736	30	0.32	0.13	0.40	0.30	0.18	0.60
J0040-5903	2	0.12	0.01	0.12	0.29	0.29	0.04
J0051-4226	155	0.51	0.19	0.37	0.51	0.19	0.37
J0106-4034	1268	1.78	0.92	0.51	0.84	0.36	0.42
J0109-6049	26	0.27	0.06	0.24	0.28	0.06	0.22
J0133-5200	252	0.63	0.19	0.30	0.69	0.14	0.20
J0229-7847	46	0.47	0.09	0.20	0.41	0.07	0.17
J0236-6136	23	0.24	0.06	0.27	0.23	0.13	0.59
J0253-5441	4	0.84	0.34	0.40	0.53	0.25	0.47
J0303-6211	51	0.44	0.14	0.32	1.16	0.34	0.29
J0309-6058	713	0.69	0.19	0.27	0.94	0.19	0.21

Continued on next page

Table 4.6 – *Continued from previous page*

J0334-4008	670	1.72	0.58	0.33	1.61	0.36	0.22
J0335-5430	16	0.36	0.07	0.19	0.27	0.06	0.24
J0403-3605	659	1.87	1.52	0.80	0.70	0.28	0.40
J0406-3826	393	1.34	0.90	0.67	0.95	0.36	0.37
J0408-6545	1	n/a	n/a	n/a	n/a	n/a	n/a
J0439-4522	139	0.76	0.32	0.41	0.62	0.21	0.34
J0450-8101	121	1.17	0.32	0.27	0.75	0.26	0.35
J0506-6109	153	0.52	0.14	0.27	0.45	0.20	0.45
J0516-6207	82	0.78	0.25	0.31	0.51	0.12	0.23
J0522-6107	32	0.27	0.40	1.46	0.30	0.22	0.75
J0525-4557	39	0.20	0.12	0.59	0.36	0.32	0.87
J0534-6106	30	0.33	0.09	0.29	0.36	0.07	0.21
J0536-3401	105	0.32	0.18	0.54	0.35	0.14	0.39
J0538-4405	1562	5.99	3.73	0.62	4.86	2.88	0.59
J0550-5732	41	0.59	0.14	0.25	0.42	0.10	0.24
J0922-3959	793	0.75	0.31	0.42	0.79	0.38	0.48
J0930-8533	2	0.23	0.004	0.021	0.16	0.01	0.09
J1006-5018	168	0.55	0.26	0.47	0.29	0.17	0.57
J1014-4508	10	0.58	0.26	0.45	0.49	0.13	0.27
J1023-6646	32	0.48	0.12	0.25	0.34	0.06	0.18
J1036-3744	42	0.39	0.17	0.42	0.32	0.14	0.45
J1041-4740	1	n/a	n/a	n/a	n/a	n/a	n/a
J1047-6217	8	1.27	0.17	0.13	0.50	0.07	0.14
J1103-5357	24	0.32	0.11	0.36	0.33	0.14	0.44
J1112-5703	11	0.29	0.10	0.34	0.37	0.19	0.53
J1118-4638	12	0.25	0.06	0.24	0.26	0.07	0.30
J1131-5818	4	0.61	0.32	0.51	0.48	0.08	0.17
J1145-6954	25	0.45	0.12	0.28	0.31	0.09	0.30
J1147-3812	1334	1.96	0.80	0.40	1.16	0.43	0.37
J1151-6728	4	0.33	0.10	0.29	0.59	0.18	0.30
J1159-6635	21	0.16	0.02	0.14	0.21	0.04	0.19
J1254-7138	30	0.52	0.15	0.29	0.60	0.20	0.33
J1316-3338	152	1.04	0.66	0.63	0.88	0.55	0.62
J1326-5256	6	1.03	0.41	0.39	0.6	0.18	0.31
J1329-5608	33	0.64	0.41	0.65	0.31	0.14	0.46
J1346-6024	10	0.25	0.08	0.34	0.61	0.51	0.84
J1352-4412	43	0.26	0.10	0.38	0.20	0.07	0.34

Continued on next page

Table 4.6 – *Continued from previous page*

J1355-6326	6	0.52	0.22	0.43	0.44	0.13	0.29
J1424-6807	30	0.91	0.25	0.28	0.43	0.10	0.24
J1427-4206	1451	4.67	3.60	0.77	2.37	1.26	0.53
J1452-6502	16	0.22	0.13	0.58	0.32	0.07	0.23
J1454-4012	48	0.27	0.14	0.52	0.38	0.17	0.45
J1514-4748	11	1.01	0.21	0.20	0.98	0.31	0.32
J1538-6525	1	n/a	n/a	n/a	n/a	n/a	n/a
J1558-6432	17	0.22	0.10	0.45	0.30	0.14	0.48
J1607-3331	53	0.17	0.11	0.66	0.17	0.10	0.62
J1616-7108	18	0.23	0.04	0.18	0.27	0.14	0.52
J1624-6809	36	0.48	0.15	0.31	0.92	0.23	0.25
J1628-6152	29	0.46	0.13	0.28	0.49	0.16	0.32
J1642-8108	15	0.22	0.11	0.51	0.29	0.13	0.45
J1650-5044	5	1.03	0.25	0.24	0.25	0.13	0.55
J1701-5621	37	0.46	0.15	0.33	0.62	0.26	0.41
J1703-6212	32	0.70	0.28	0.40	0.43	0.11	0.27
J1733-7935	25	0.40	0.15	0.37	0.25	0.10	0.41
J1744-5144	6	0.24	0.07	0.31	0.93	0.31	0.33
J1803-6507	239	0.48	0.14	0.30	0.47	0.10	0.21
J1809-4552	50	0.42	0.11	0.26	0.27	0.10	0.37
J1819-5521	283	0.66	0.30	0.45	0.73	0.26	0.35
J1829-5813	30	0.53	0.27	0.51	0.27	0.09	0.33
J1835-7149	2	0.17	0.06	0.37	0.20	0.03	0.15
J1837-7108	33	0.65	0.34	0.51	0.64	0.21	0.33
J1857-5325	8	0.14	0.02	0.17	0.26	0.04	0.17
J1930-6056	36	0.36	0.07	0.22	0.57	0.13	0.24
J1932-4536	4	0.18	0.02	0.13	0.21	0.009	0.04
J1933-6942	–	–	–	–	–	–	–
J1937-3958	75	0.74	0.22	0.29	0.51	0.14	0.27
J1940-6907	30	0.34	0.09	0.27	0.39	0.09	0.22
J1941-6211	7	0.29	0.08	0.28	0.49	0.13	0.27
J1955-6115	4	0.23	0.07	0.32	0.45	0.06	0.14
J1957-3845	1070	1.84	0.78	0.42	1.38	0.55	0.39
J2005-3723	42	0.31	0.07	0.24	0.31	0.07	0.23
J2035-6846	7	0.58	0.16	0.28	0.22	0.08	0.37
J2056-4714	1059	3.44	2.41	0.70	1.71	0.63	0.36
J2109-4110	42	0.40	0.33	0.83	0.58	0.33	0.57

Continued on next page

Table 4.6 – *Continued from previous page*

J2126-4605	32	0.24	0.09	0.37	0.23	0.08	0.37
J2147-7536	79	1.25	0.36	0.28	0.73	0.18	0.25
J2207-5346	48	0.60	0.21	0.36	0.64	0.19	0.29
J2223-3455	42	0.20	0.07	0.39	0.21	0.08	0.39
J2235-4835	149	0.82	0.23	0.28	0.82	0.17	0.21
J2239-5701	37	0.85	0.18	0.21	0.45	0.19	0.42
J2247-3657	53	0.42	0.14	0.33	0.29	0.10	0.36
J2248-3235	33	0.42	0.16	0.37	0.37	0.10	0.28
J2303-6807	287	0.43	0.21	0.48	0.50	0.12	0.25
J2329-4730	67	0.71	0.19	0.26	0.56	0.14	0.25
J2336-4115	37	0.28	0.10	0.36	0.26	0.09	0.35
J2336-5236	5	0.48	0.03	0.07	0.98	0.09	0.09
J2347-5110	26	0.27	0.09	0.33	0.30	0.07	0.26
J2356-6820	56	0.62	0.18	0.29	0.35	0.09	0.25
J2357-5311	95	1.29	0.31	0.24	0.72	0.13	0.19
J2359-3133	209	0.35	0.12	0.36	0.56	0.57	1.00

4.4 VLBI contour maps of the sources

4.4.1 Contour maps

In this section, I present the contour maps of the sources imaged using the CRDS sessions. The contour maps of the sources are presented in Figure 4.7 in a similar way as they appeared in Table 3.3 in R.A. order. For each source where both S- and X-band maps are available, S-band contour maps are presented first which are followed by the contour maps at X-band. It should be noted that all the plots are on the same scale of 10×10 mas. The beam size is indicated in the bottom left corner and the epoch of observation is indicated in the right corner of each plot.

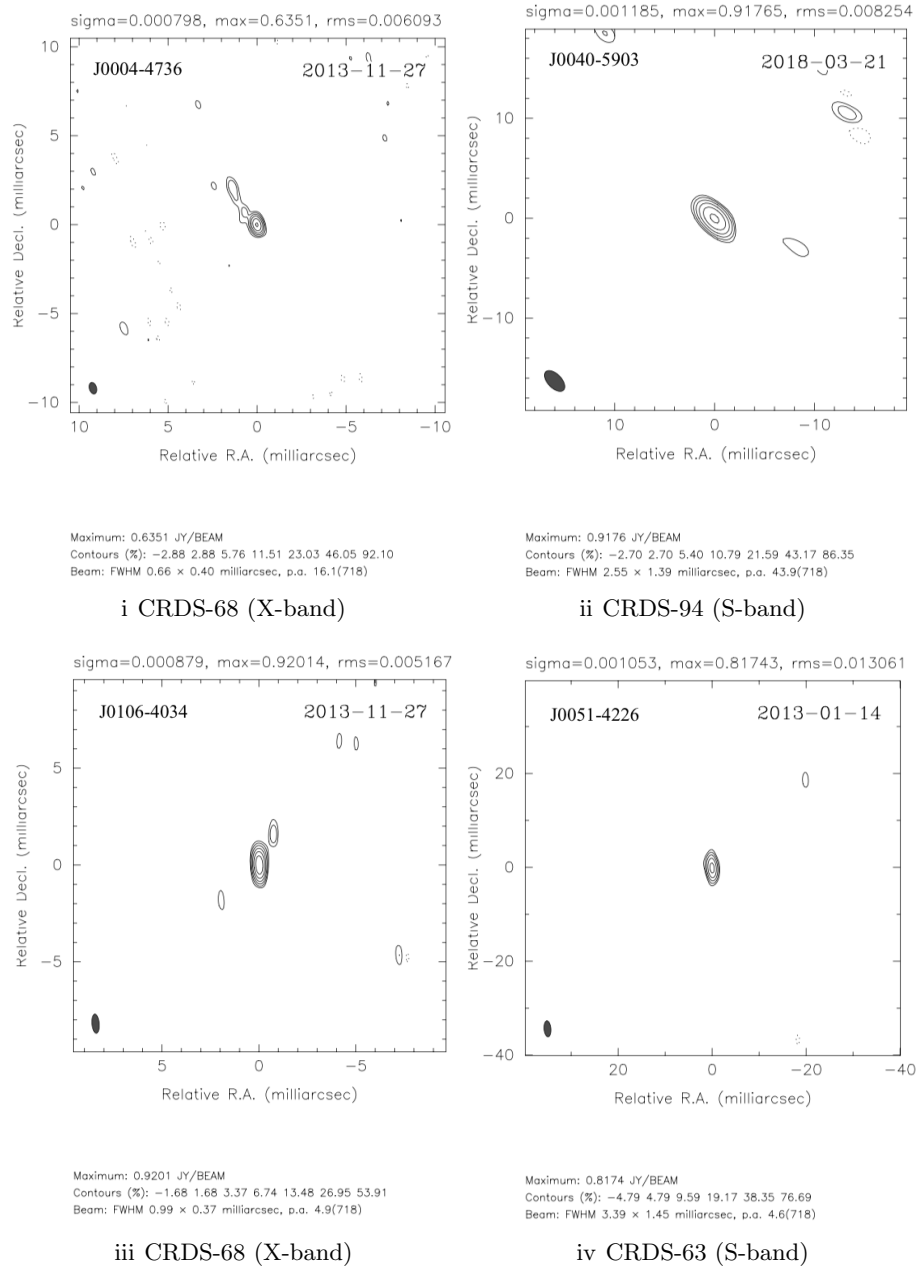


FIGURE 4.7: VLBI contour maps of the sources which were imaged using the four CRDS sessions. The RMS value is given in the top right corner above each map and is in Jy beam^{-1} . Source name and epoch of the observation are given on the left hand side and on the right hand side respectively in each map. In cases where a source was imaged at multi-epoch and at both S- and X-band, the S-band contour maps are presented before the X-band contour maps. Contour levels are at % of peak brightness.

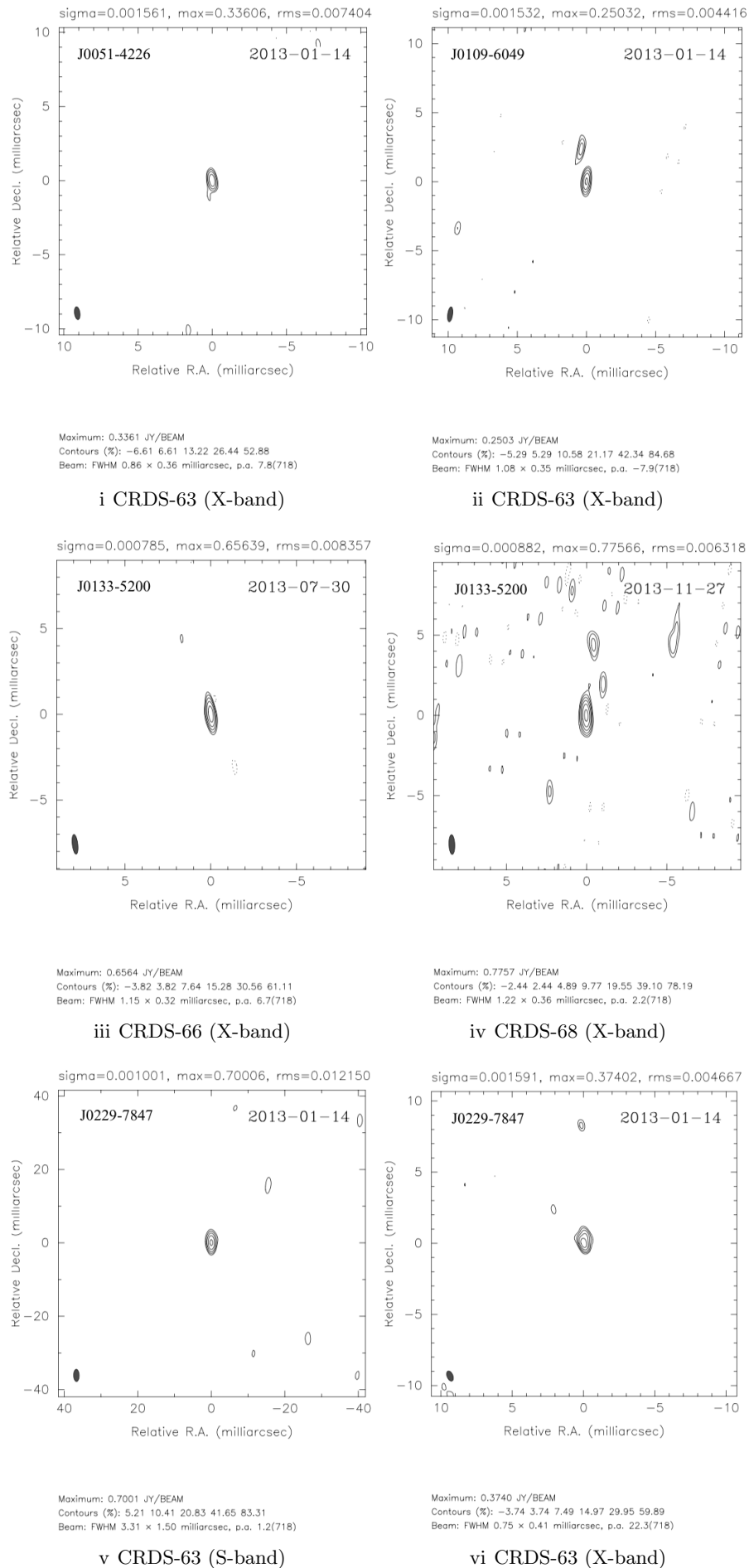


Figure 4.7 - Continued from previous page

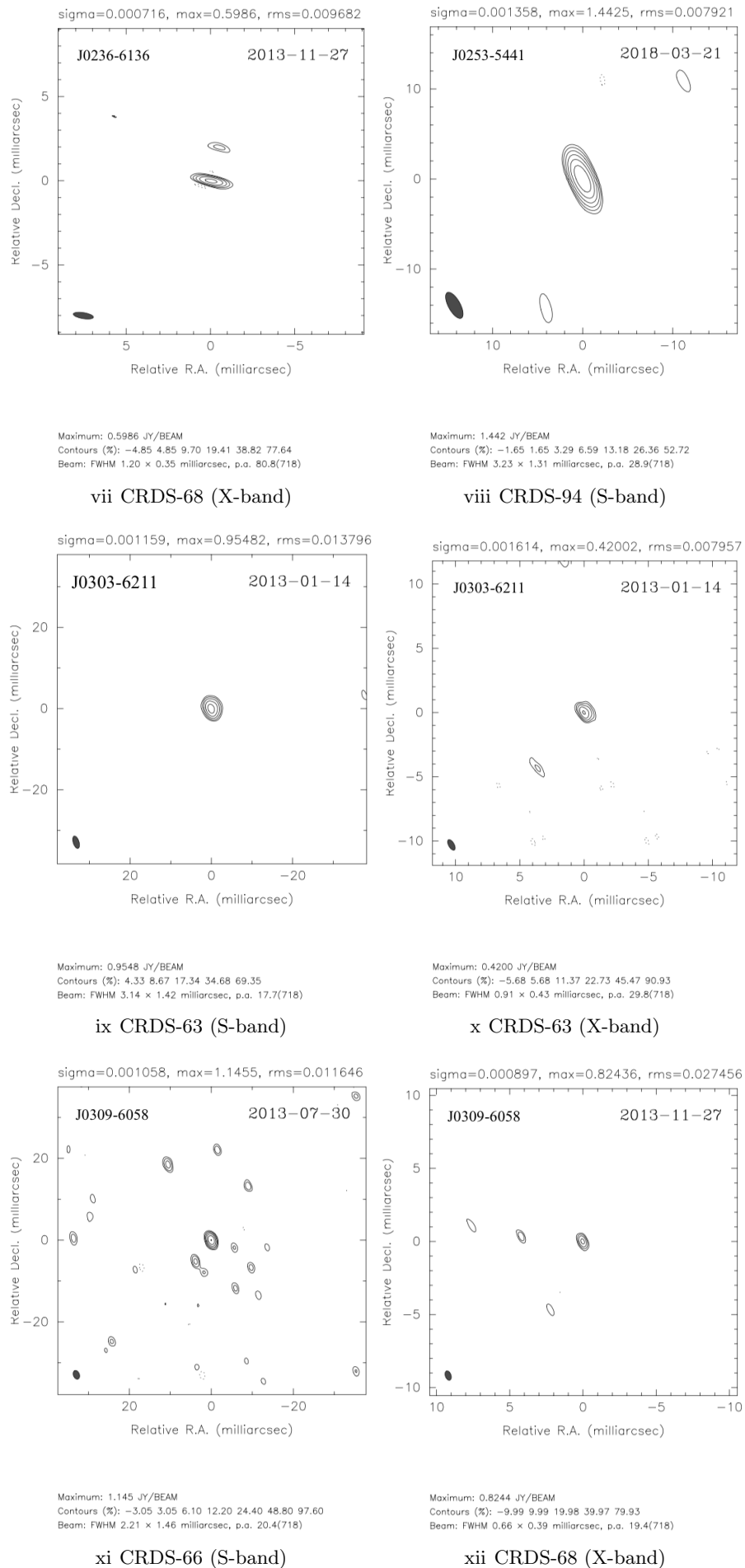


Figure 4.7 - Continued from previous page

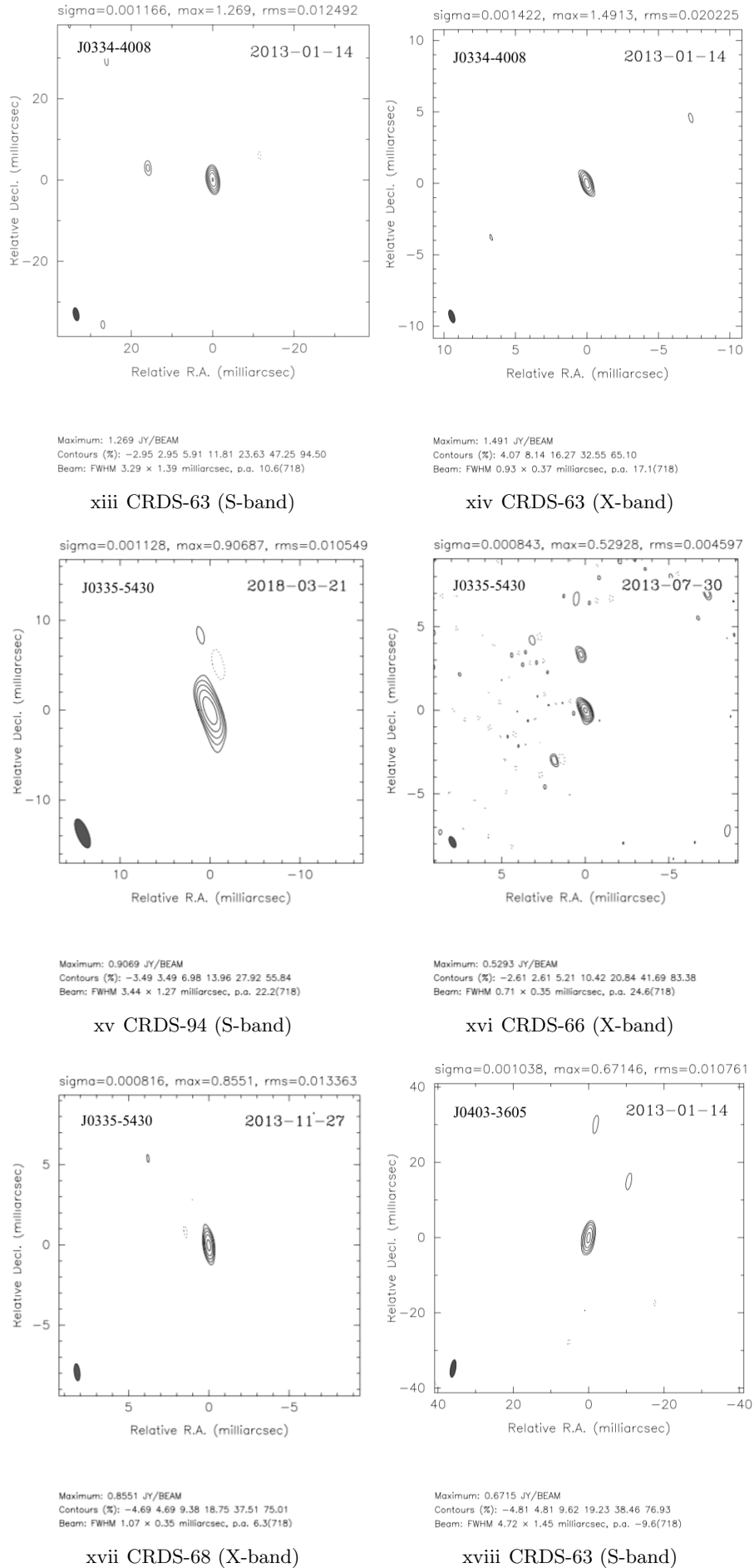


Figure 4.7 - *Continued from previous page*

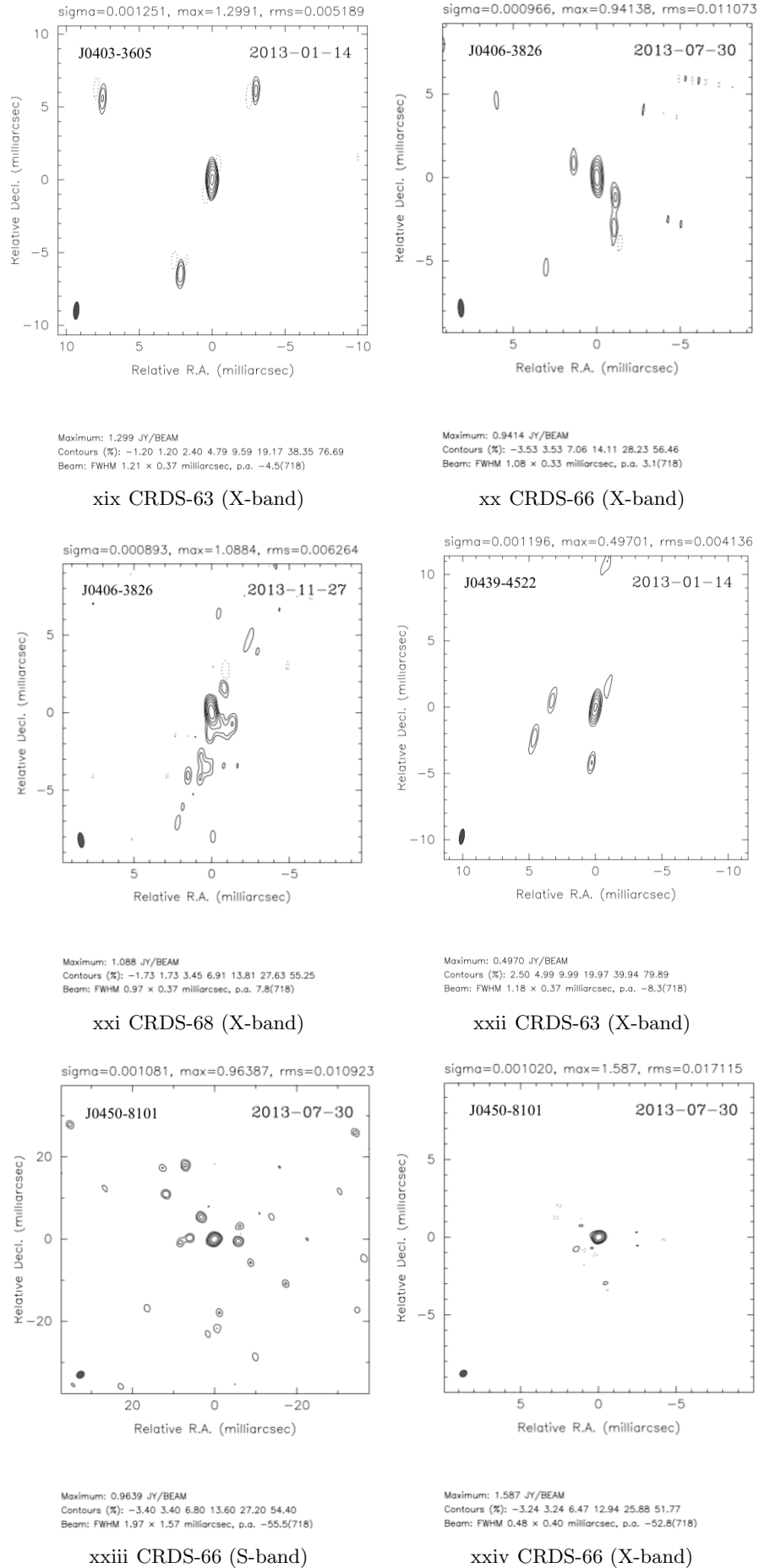


Figure 4.7 - Continued from previous page

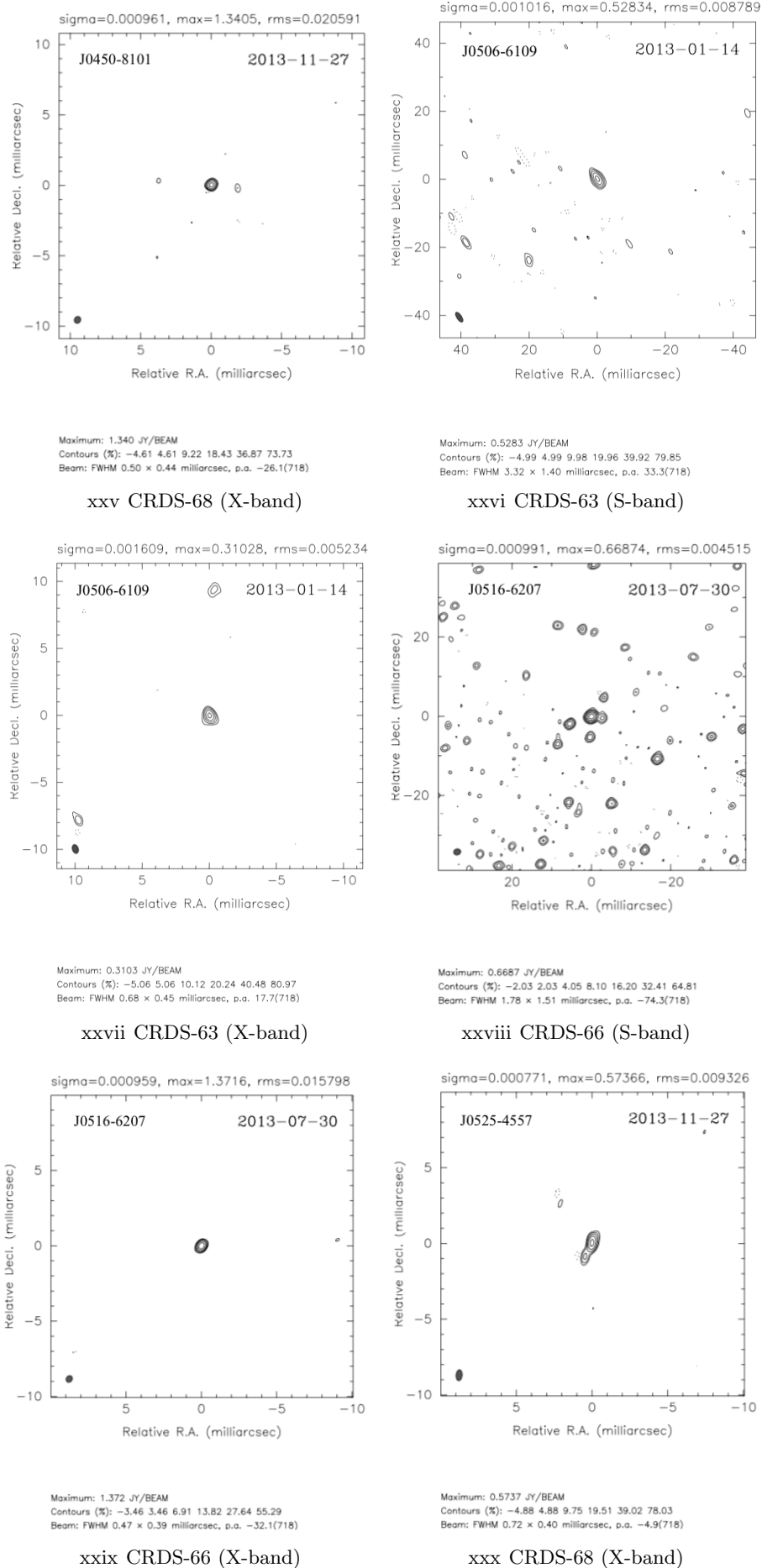


Figure 4.7 - Continued from previous page

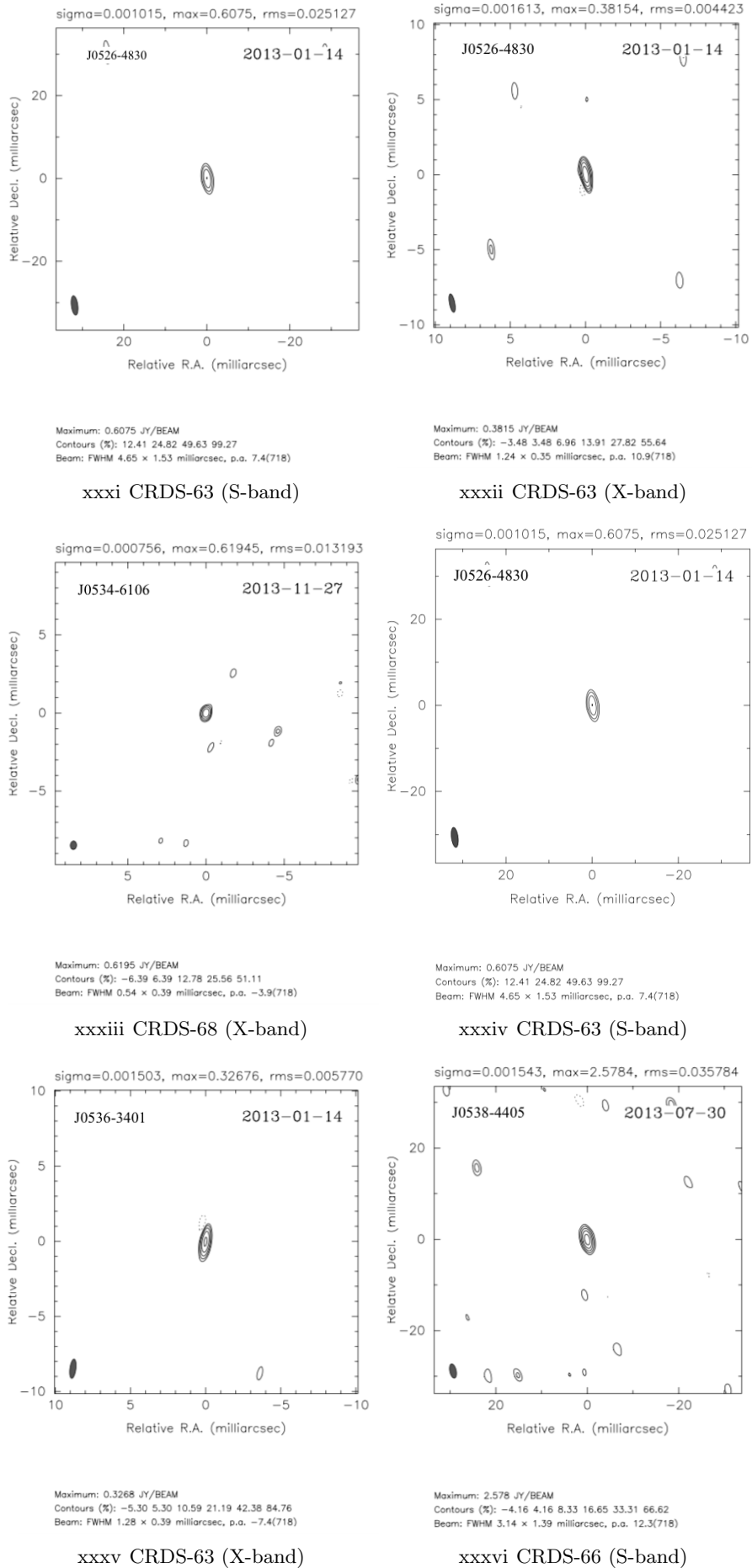
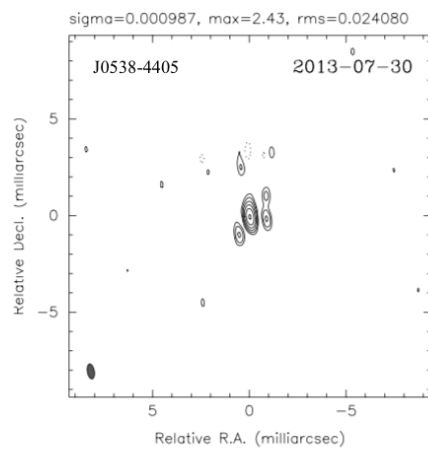
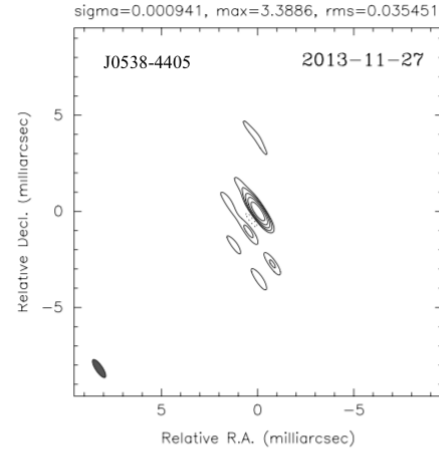


Figure 4.7 - *Continued from previous page*



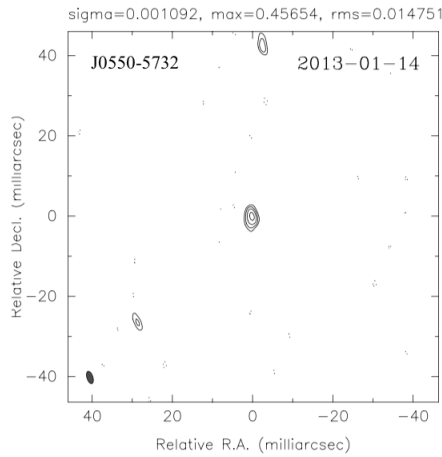
Maximum: 2.430 JY/BEAM
 Contours (%): -2.97 2.97 5.95 11.89 23.78 47.57 95.13
 Beam: FWHM 0.78 x 0.36 milliarcsec, p.a. 9.9(718)

xxxvii CRDS-66 (X-band)



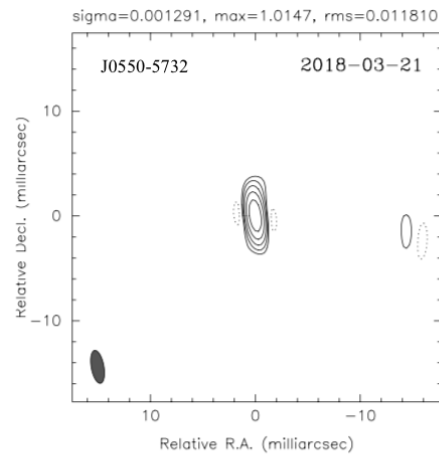
Maximum: 3.389 JY/BEAM
 Contours (%): -3.14 3.14 6.28 12.55 25.11 50.22
 Beam: FWHM 1.11 x 0.36 milliarcsec, p.a. 34.0(718)

xxxviii CRDS-68 (X-band)



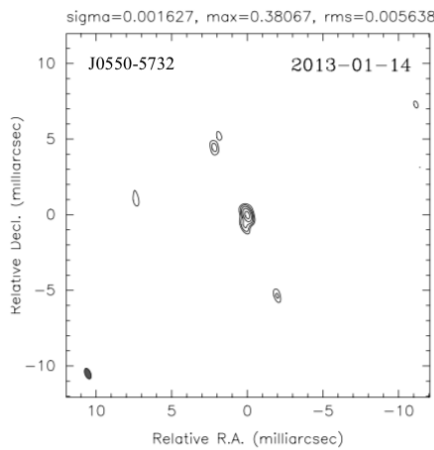
Maximum: 0.4565 JY/BEAM
 Contours (%): -9.69 9.69 19.39 38.77 77.54
 Beam: FWHM 3.17 x 1.49 milliarcsec, p.a. 17.6(718)

xxxix CRDS-63 (S-band)



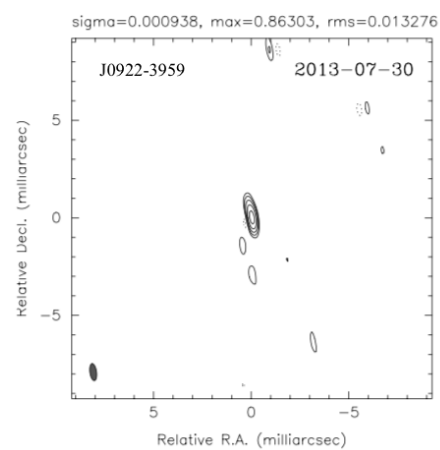
Maximum: 1.015 JY/BEAM
 Contours (%): -3.49 3.49 6.98 13.97 27.93 55.86
 Beam: FWHM 3.18 x 1.20 milliarcsec, p.a. 10.3(718)

xl CRDS-94 (S-band)



Maximum: 0.3807 JY/BEAM
 Contours (%): -4.44 4.44 8.89 17.77 35.55 71.09
 Beam: FWHM 0.74 x 0.38 milliarcsec, p.a. 22.0(718)

xli CRDS-63 (X-band)



Maximum: 0.8630 JY/BEAM
 Contours (%): -4.61 4.61 9.23 18.46 36.92 73.84
 Beam: FWHM 0.88 x 0.34 milliarcsec, p.a. 8.1(718)

xlii CRDS-66 (X-band)

Figure 4.7 - *Continued from previous page*

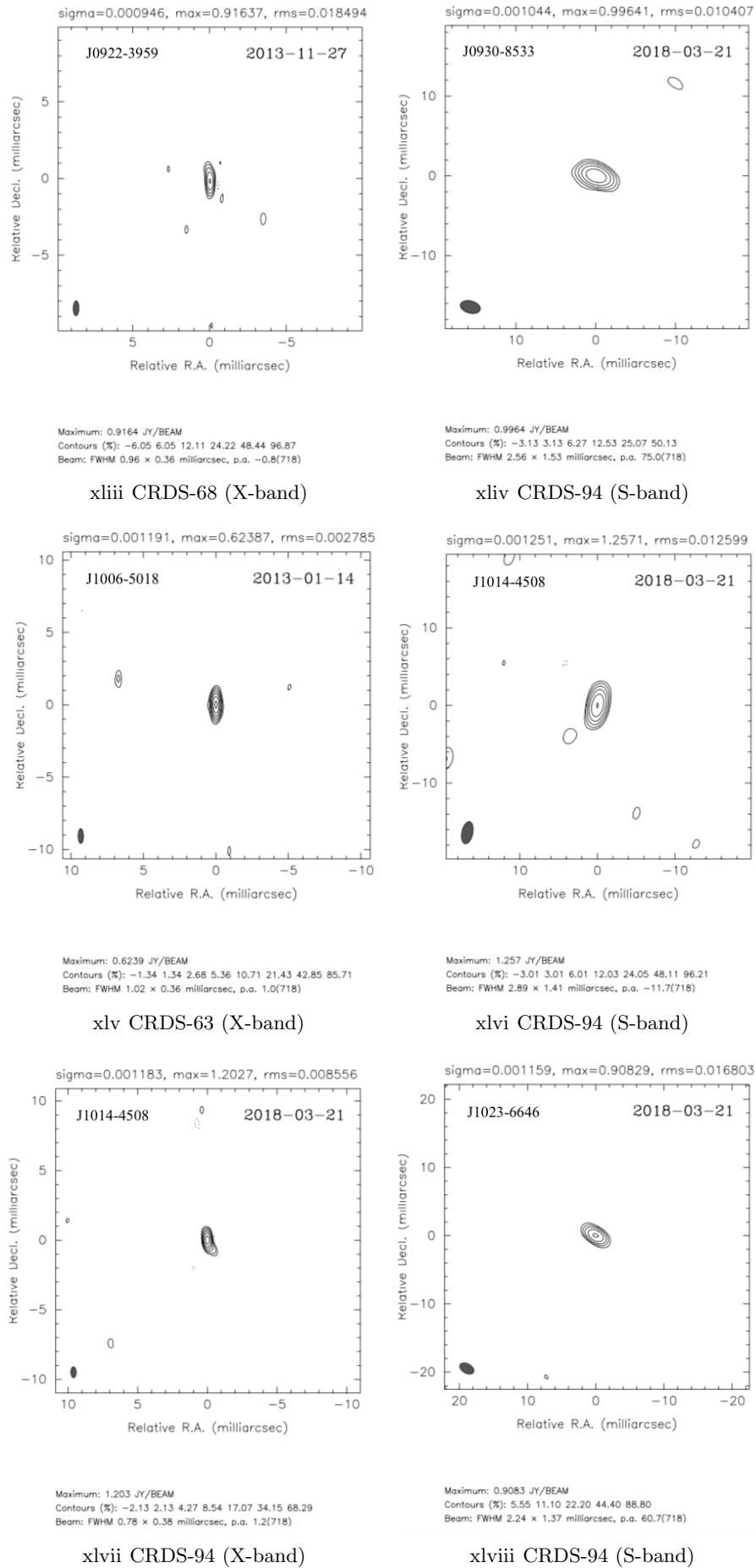


Figure 4.7 - Continued from previous page

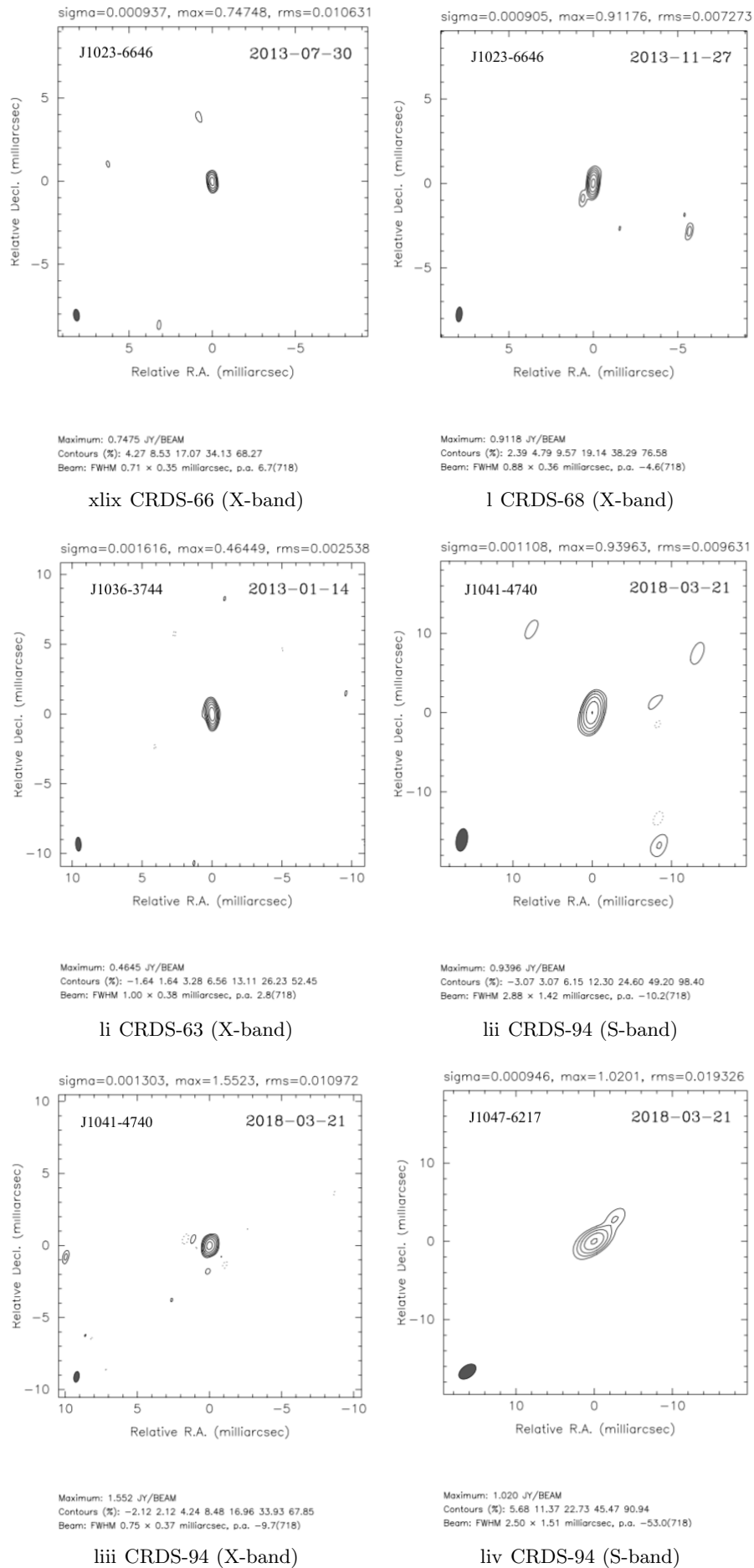
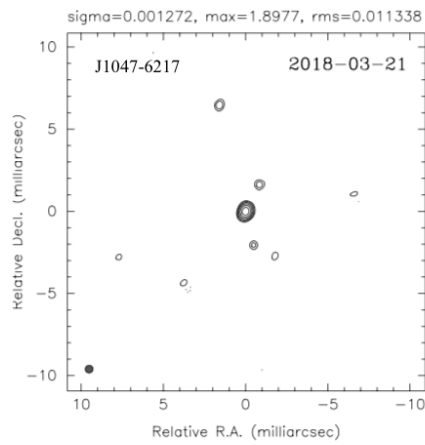
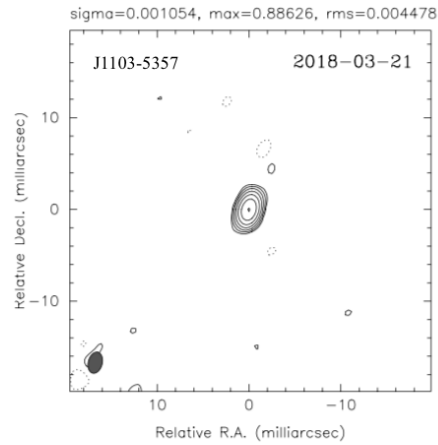


Figure 4.7 - Continued from previous page



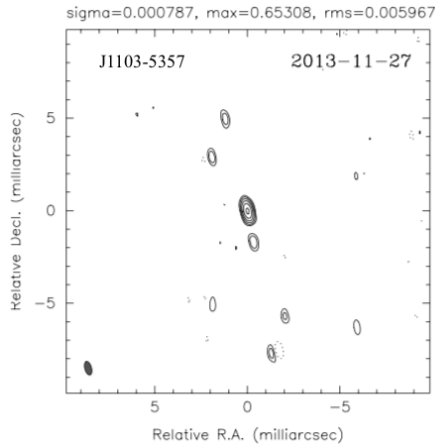
Maximum: 1.898 JY/BEAM
Contours (%): -1.79 1.79 3.58 7.17 14.34 28.68 57.35
Beam: FWHM 0.47 × 0.47 milliarcsec, p.a. -70.2(718)

lv CRDS-94 (X-band)



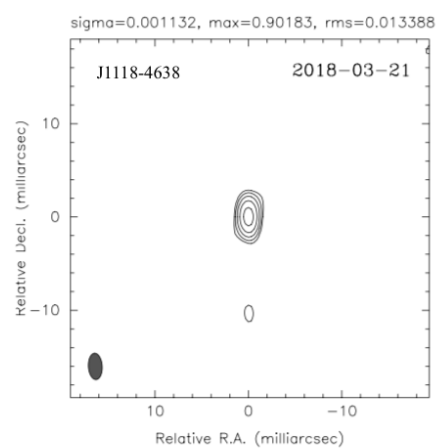
Maximum: 0.8863 JY/BEAM
Contours (%): -1.52 1.52 3.03 6.06 12.13 24.25 48.51 97.01
Beam: FWHM 2.35 × 1.53 milliarcsec, p.a. -14.5(718)

lvi CRDS-94 (S-band)



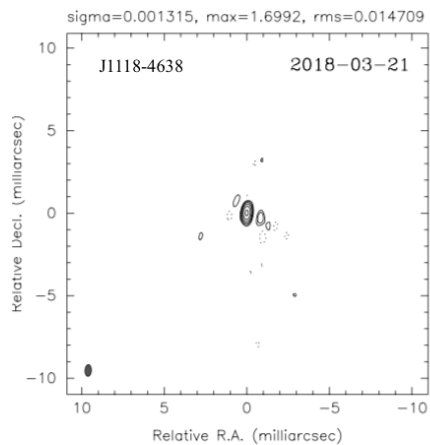
Maximum: 0.6531 JY/BEAM
Contours (%): -2.74 2.74 5.48 10.96 21.93 43.86 87.71
Beam: FWHM 0.75 × 0.36 milliarcsec, p.a. 15.4(718)

lvii CRDS-68 (X-band)



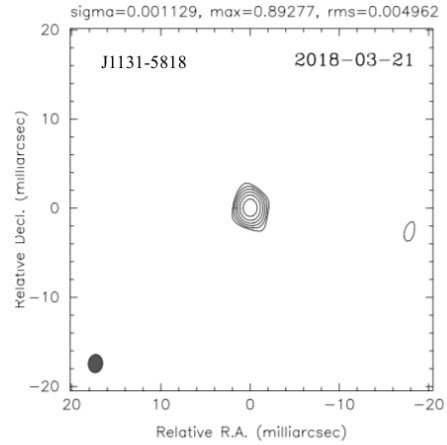
Maximum: 0.9018 JY/BEAM
Contours (%): 4.45 8.91 17.81 35.63 71.26
Beam: FWHM 2.83 × 1.47 milliarcsec, p.a. 3.5(718)

lviii CRDS-94 (S-band)



Maximum: 1.699 JY/BEAM
Contours (%): -2.60 2.60 5.19 10.39 20.78 41.55 83.10
Beam: FWHM 0.71 × 0.38 milliarcsec, p.a. -2.9(718)

lix CRDS-94 (X-band)



Maximum: 0.8928 JY/BEAM
Contours (%): 1.67 3.33 6.67 13.34 26.68 53.36
Beam: FWHM 2.03 × 1.59 milliarcsec, p.a. -4.8(718)

lx CRDS-94 (S-band)

Figure 4.7 - Continued from previous page

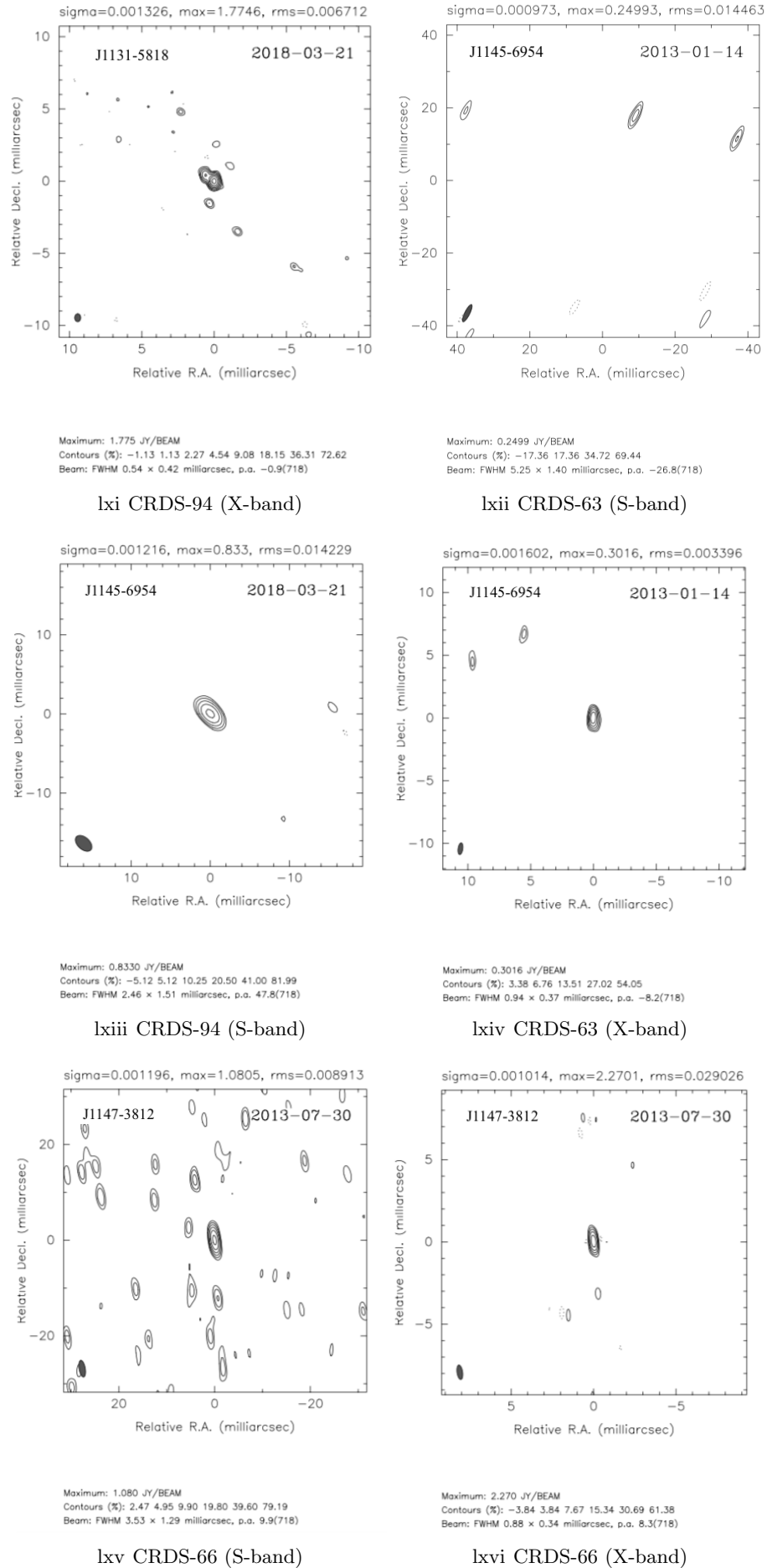


Figure 4.7 - *Continued from previous page*

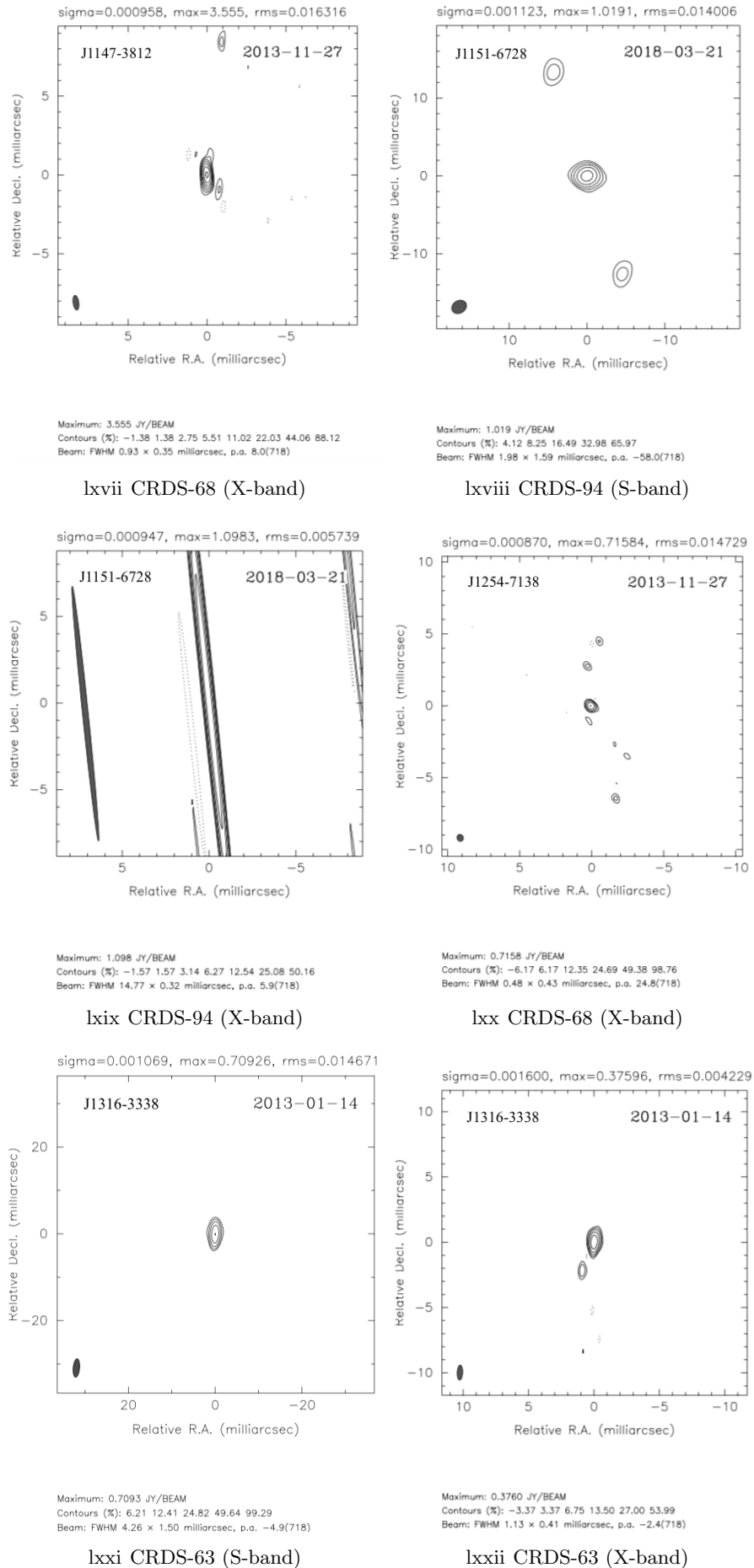


Figure 4.7 - Continued from previous page

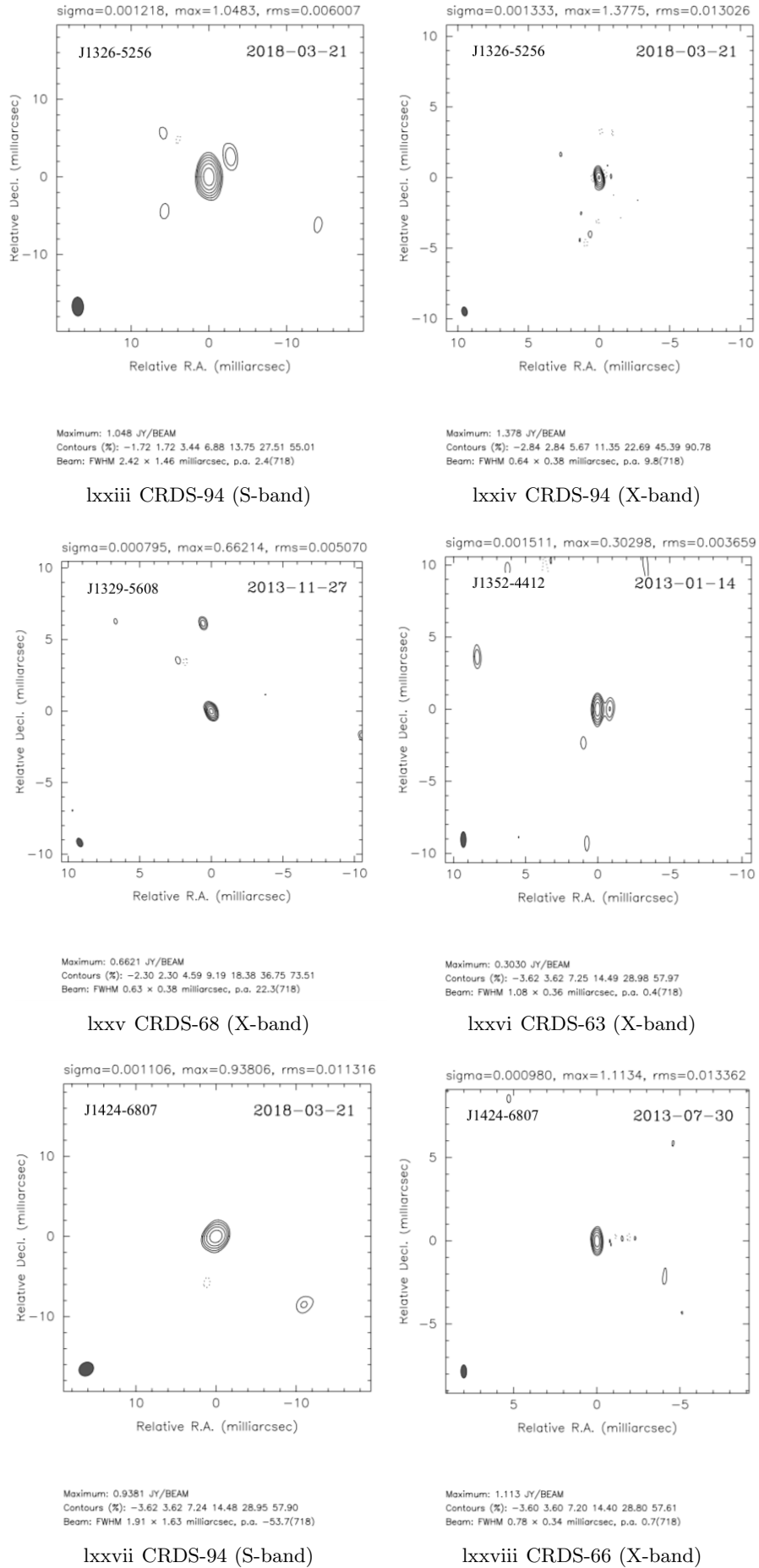


Figure 4.7 - Continued from previous page

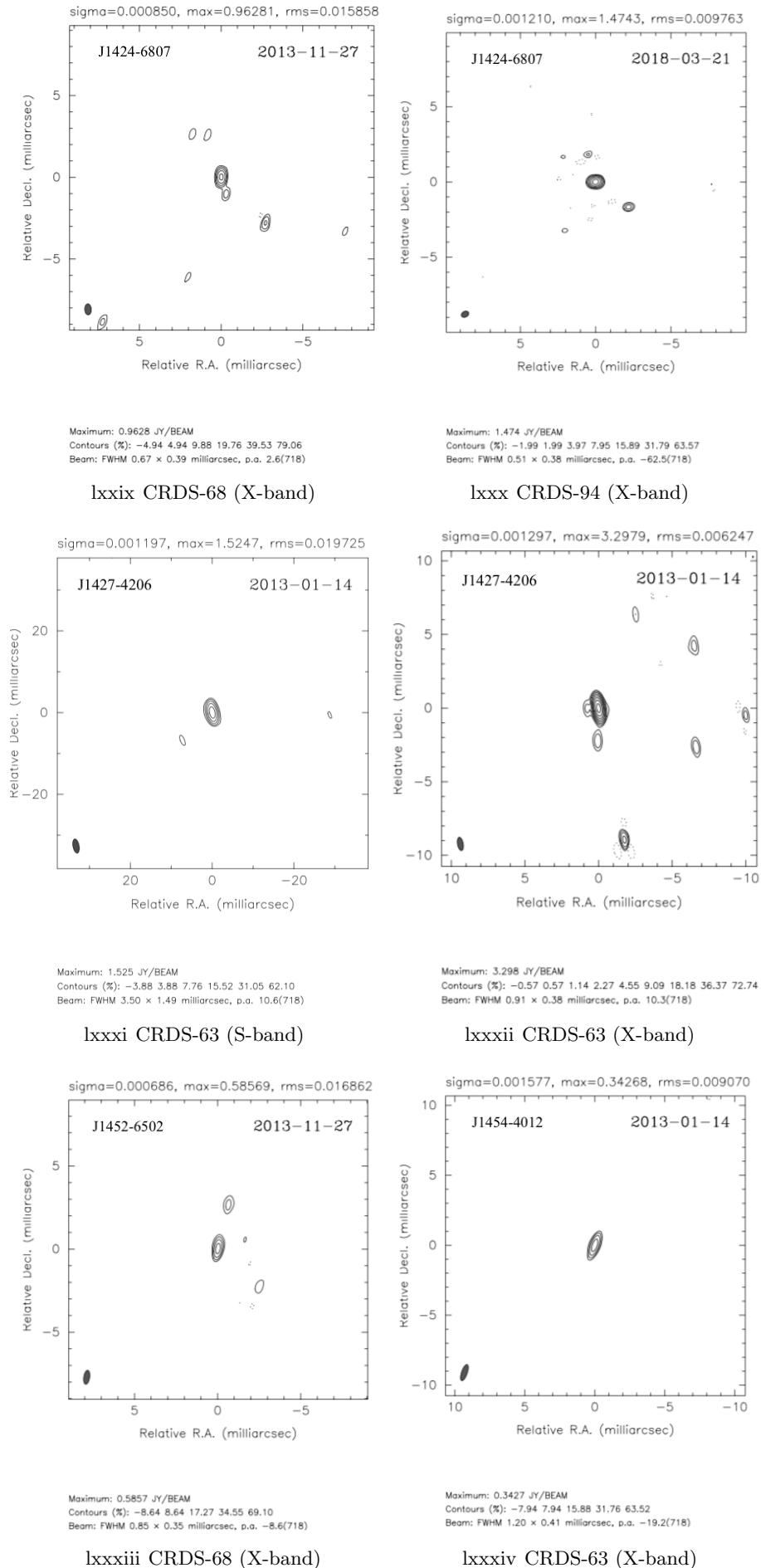


Figure 4.7 - Continued from previous page

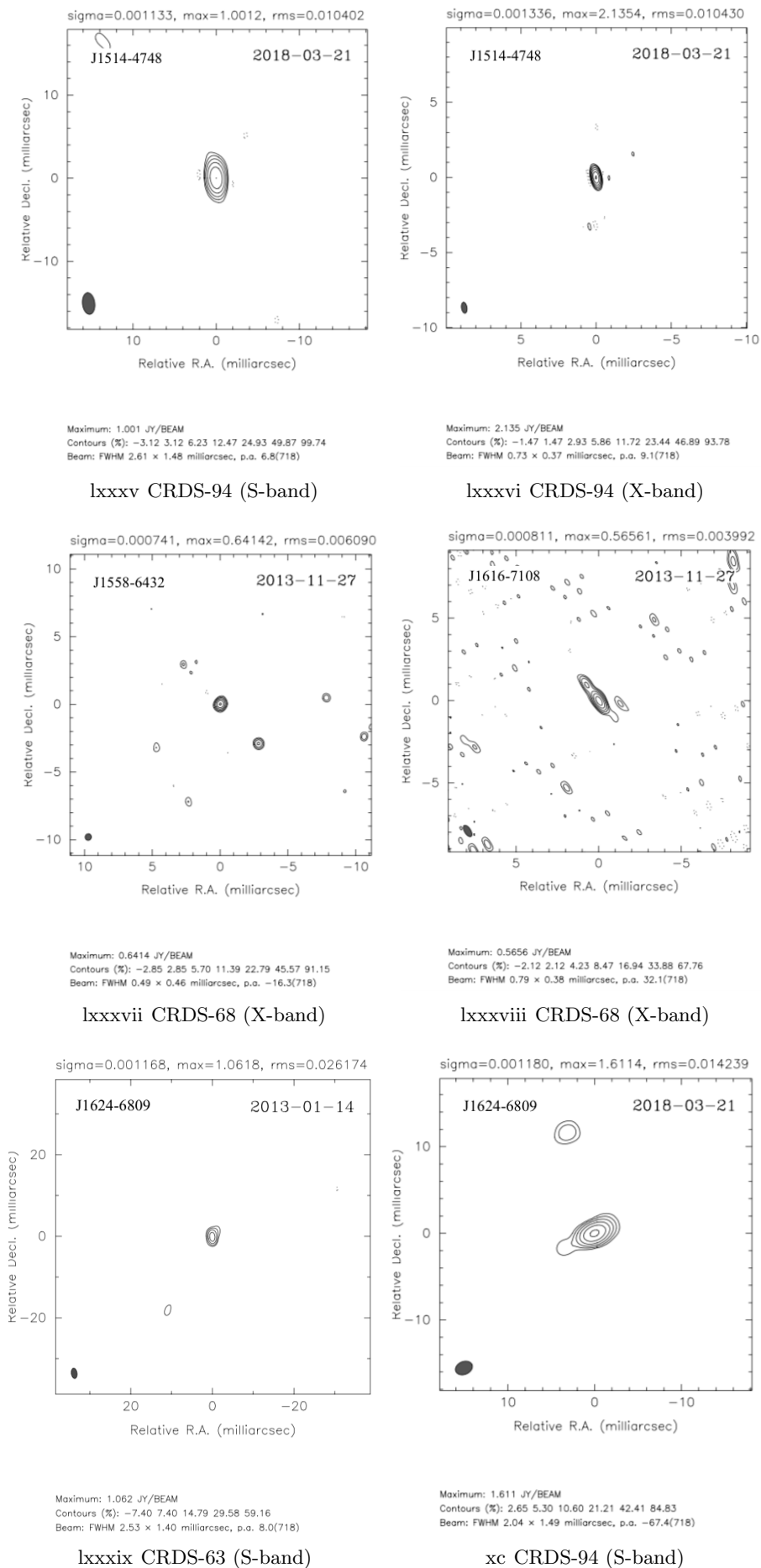


Figure 4.7 - *Continued from previous page*

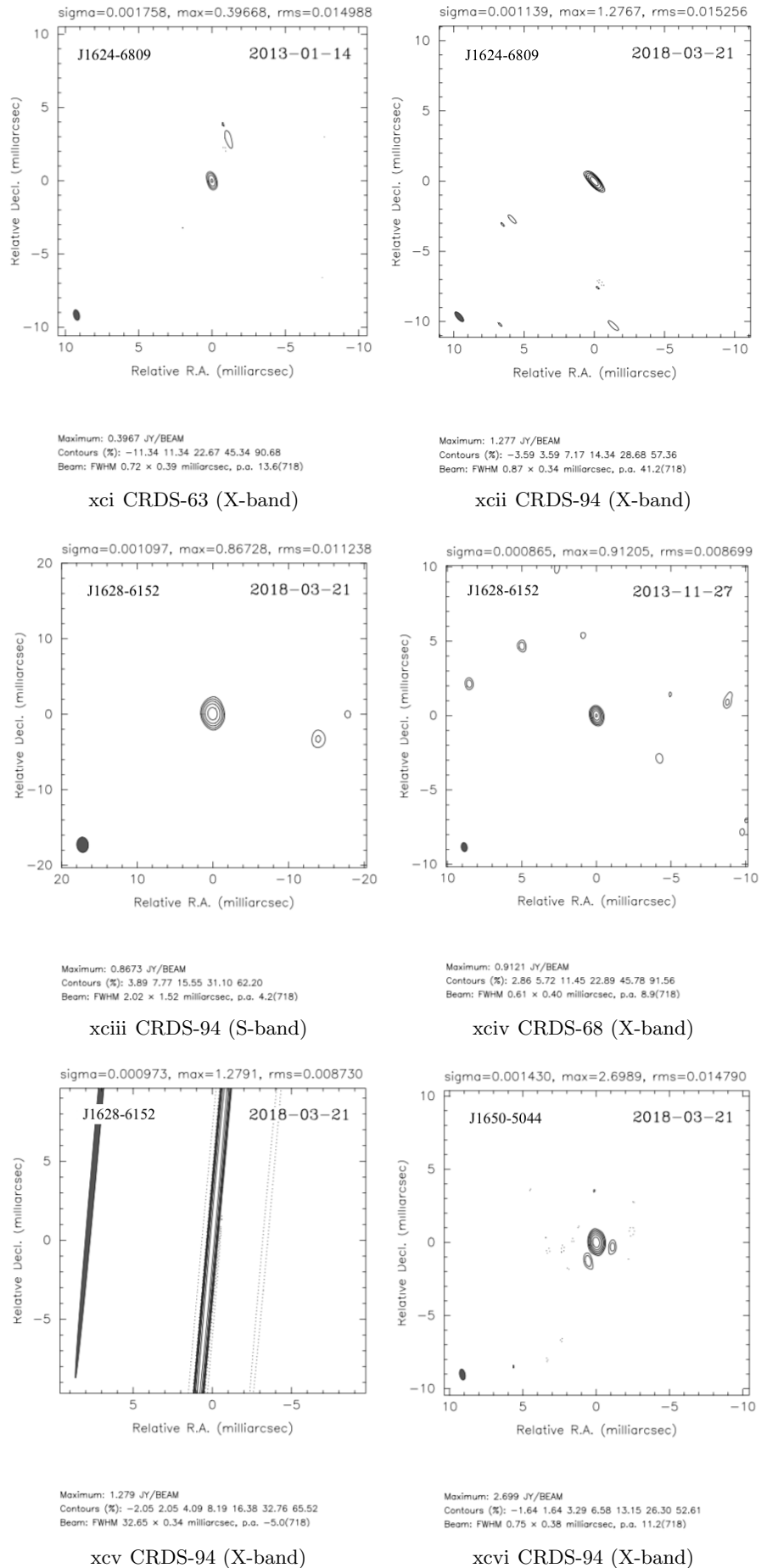
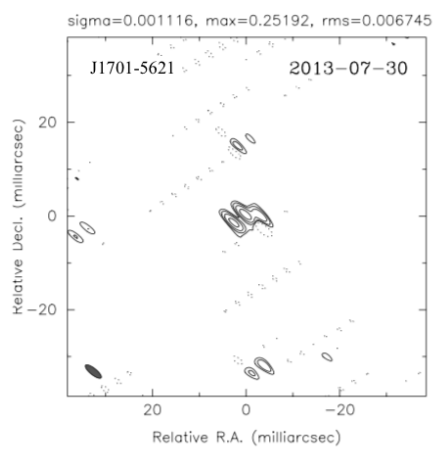
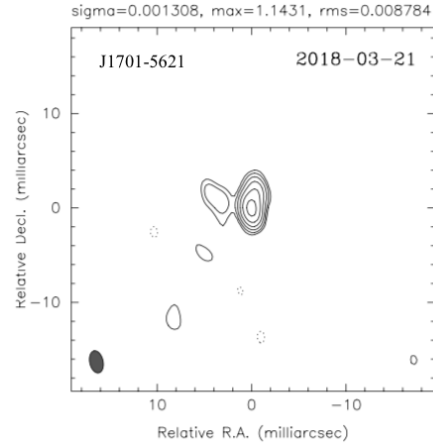


Figure 4.7 - Continued from previous page



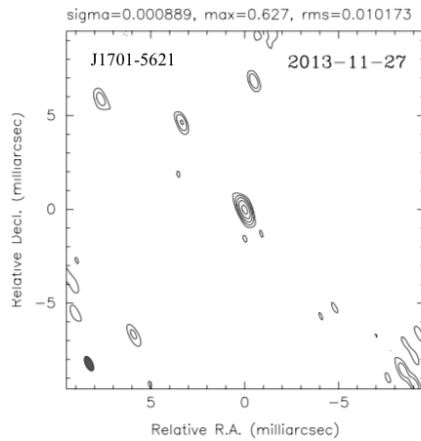
Maximum: 0.2519 JY/BEAM
 Contours (%): -8.03 8.03 16.06 32.13 64.26
 Beam: FWHM 4.23 x 1.39 milliarcsec, p.a. 51.3(718)

xcvii CRDS-66 (S-band)



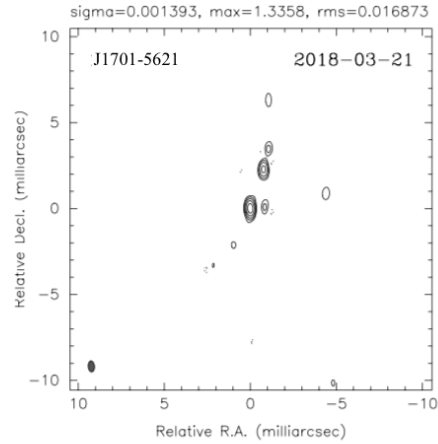
Maximum: 1.143 JY/BEAM
 Contours (%): -2.31 2.31 4.61 9.22 18.44 36.89 73.77
 Beam: FWHM 2.39 x 1.42 milliarcsec, p.a. 12.4(718)

xcviii CRDS-94 (S-band)



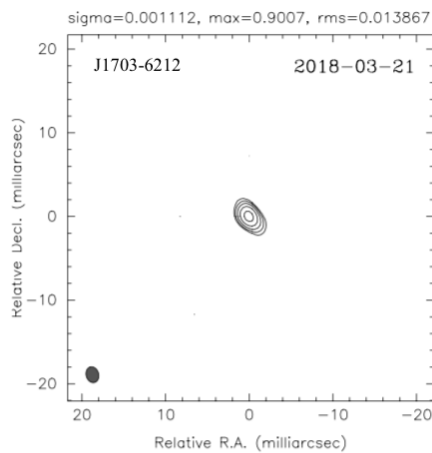
Maximum: 0.6270 JY/BEAM
 Contours (%): -4.87 4.87 9.73 19.47 38.94 77.88
 Beam: FWHM 0.84 x 0.38 milliarcsec, p.a. 25.8(718)

xcix CRDS-68 (X-band)



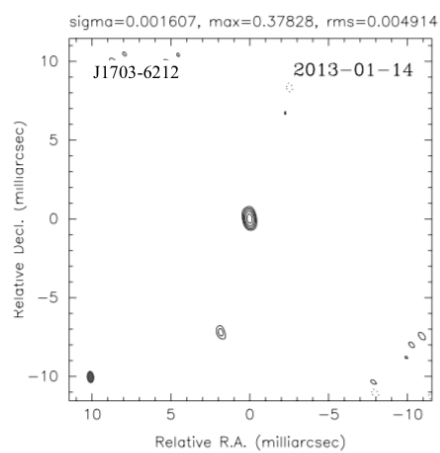
Maximum: 1.336 JY/BEAM
 Contours (%): -3.79 3.79 7.58 15.16 30.31 60.63
 Beam: FWHM 0.64 x 0.36 milliarcsec, p.a. 5.0(718)

c CRDS-94 (X-band)



Maximum: 0.9007 JY/BEAM
 Contours (%): -4.62 4.62 9.24 18.47 36.95 73.90
 Beam: FWHM 1.92 x 1.49 milliarcsec, p.a. 16.2(718)

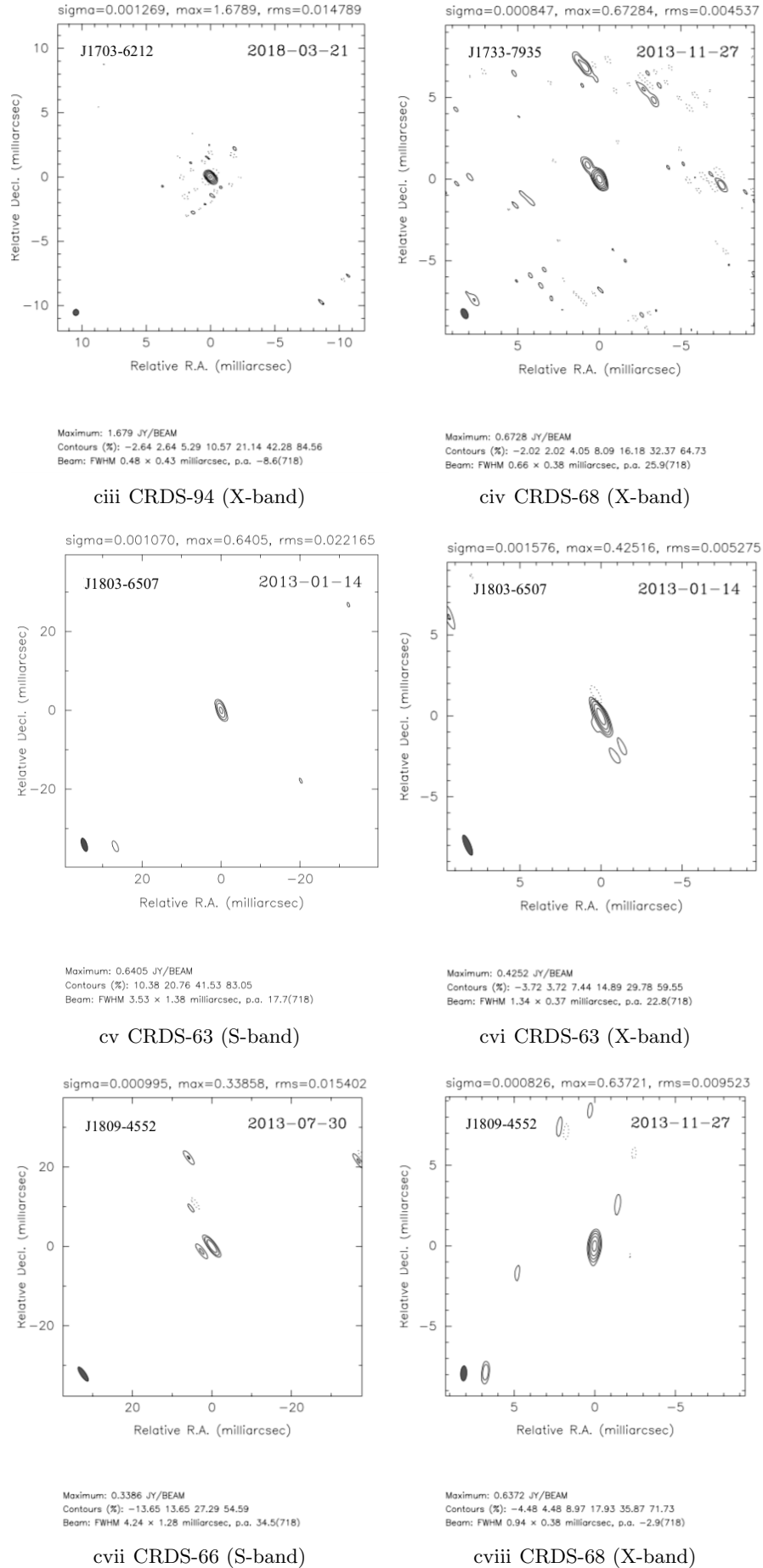
ci CRDS-94 (S-band)



Maximum: 0.3783 JY/BEAM
 Contours (%): -3.90 3.90 7.79 15.59 31.18 62.35
 Beam: FWHM 0.71 x 0.40 milliarcsec, p.a. 5.2(718)

cii CRDS-63 (X-band)

Figure 4.7 - *Continued from previous page*

Figure 4.7 - *Continued from previous page*

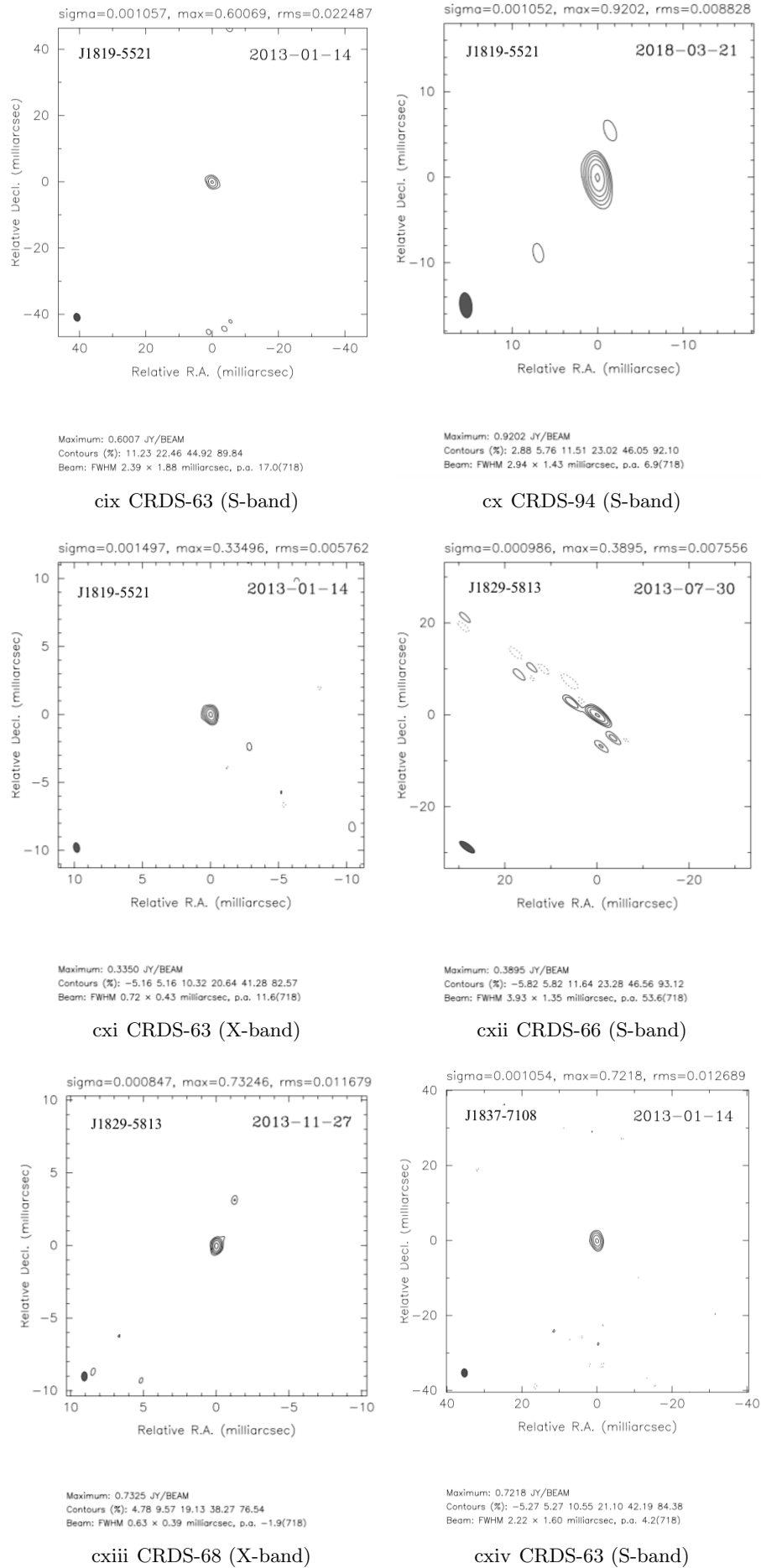


Figure 4.7 - Continued from previous page

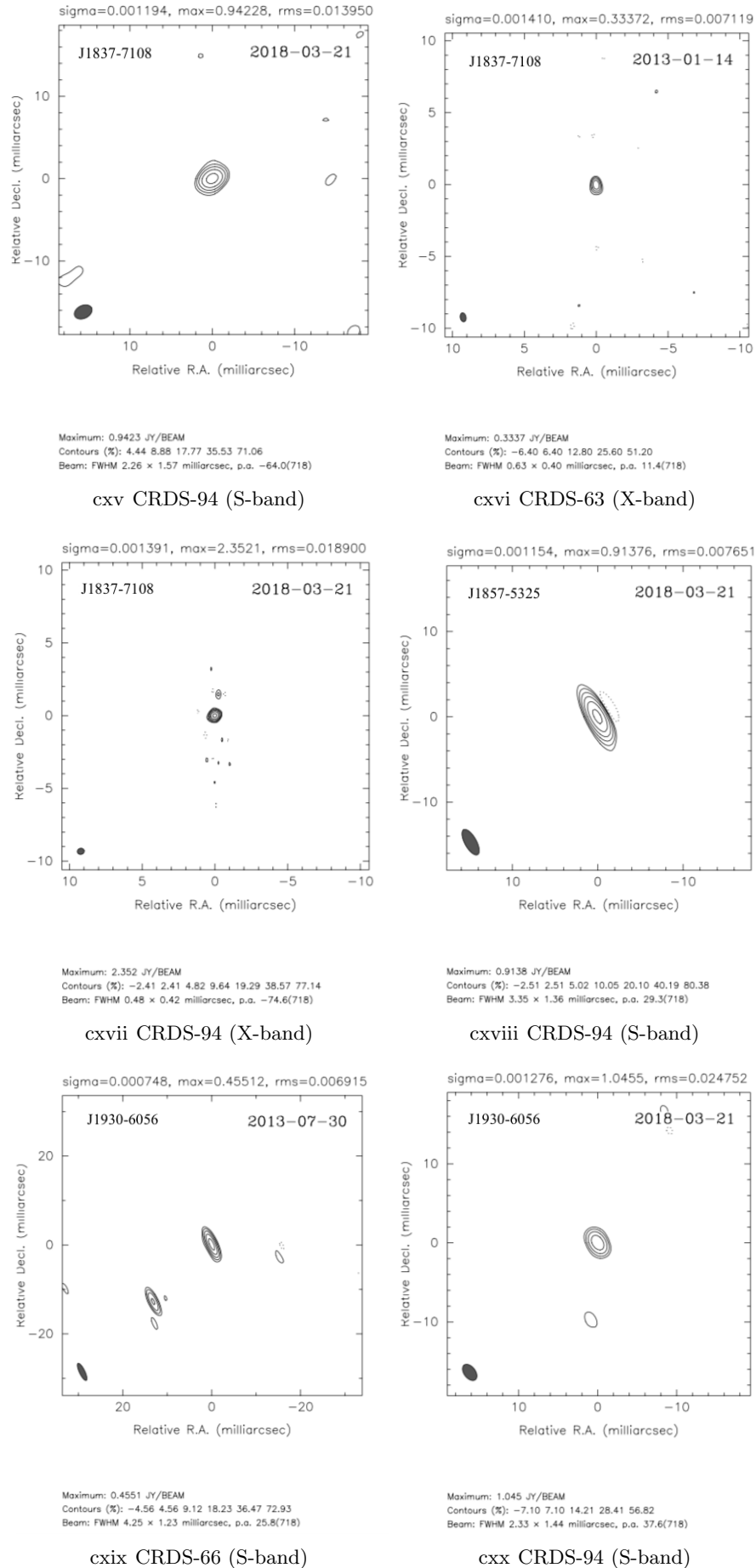


Figure 4.7 - Continued from previous page

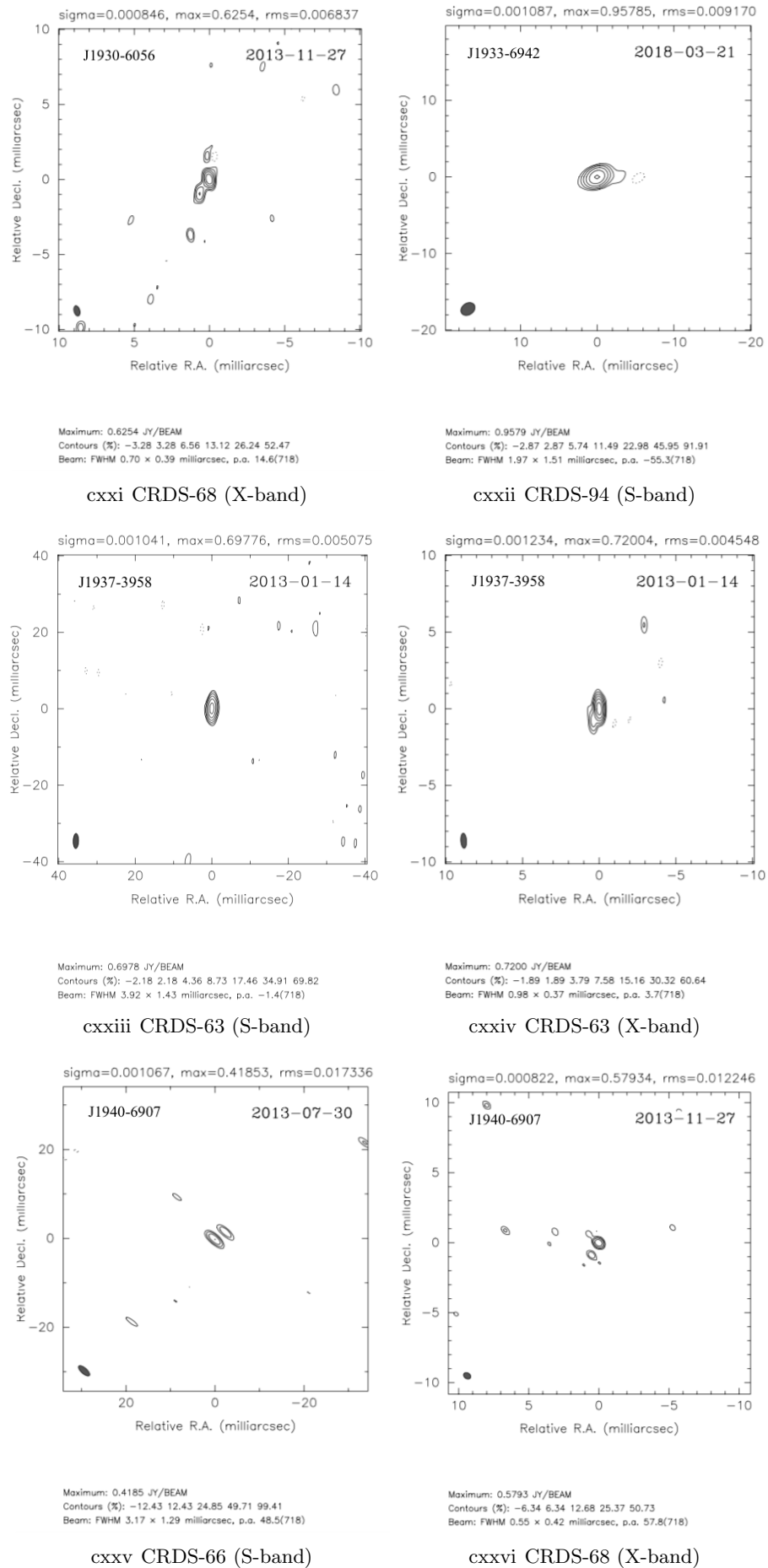


Figure 4.7 - Continued from previous page

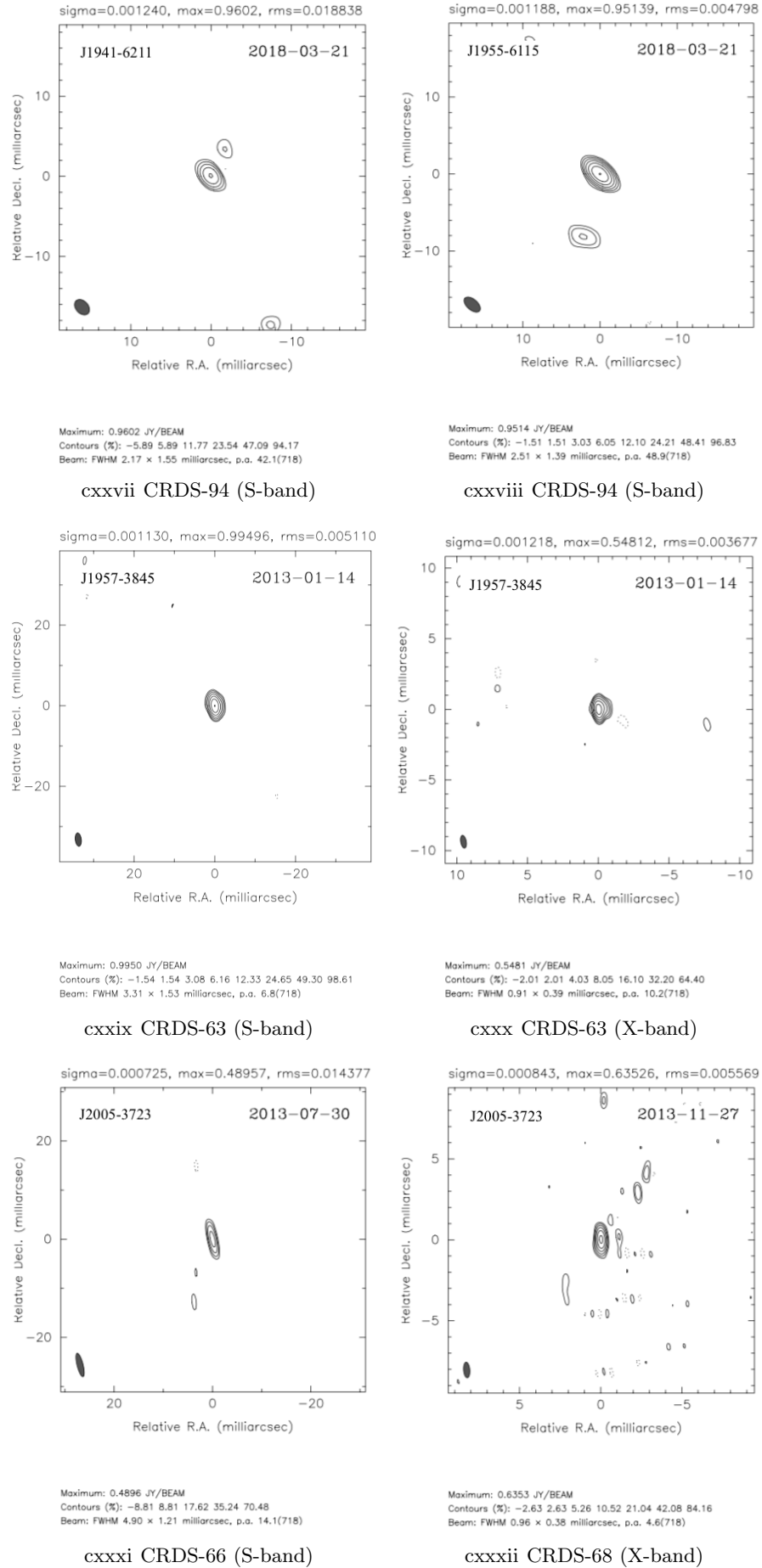
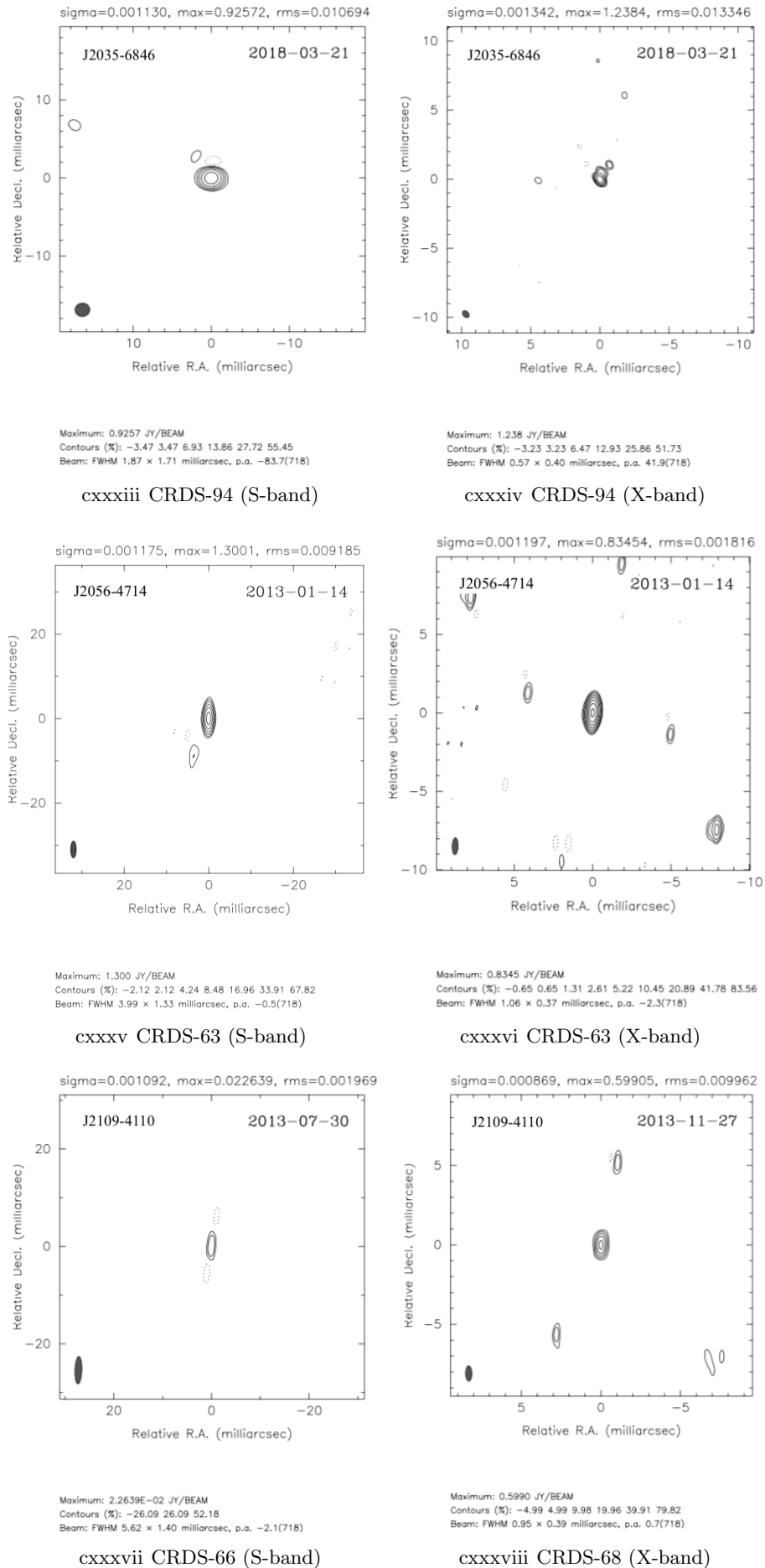


Figure 4.7 - Continued from previous page

Figure 4.7 - *Continued from previous page*

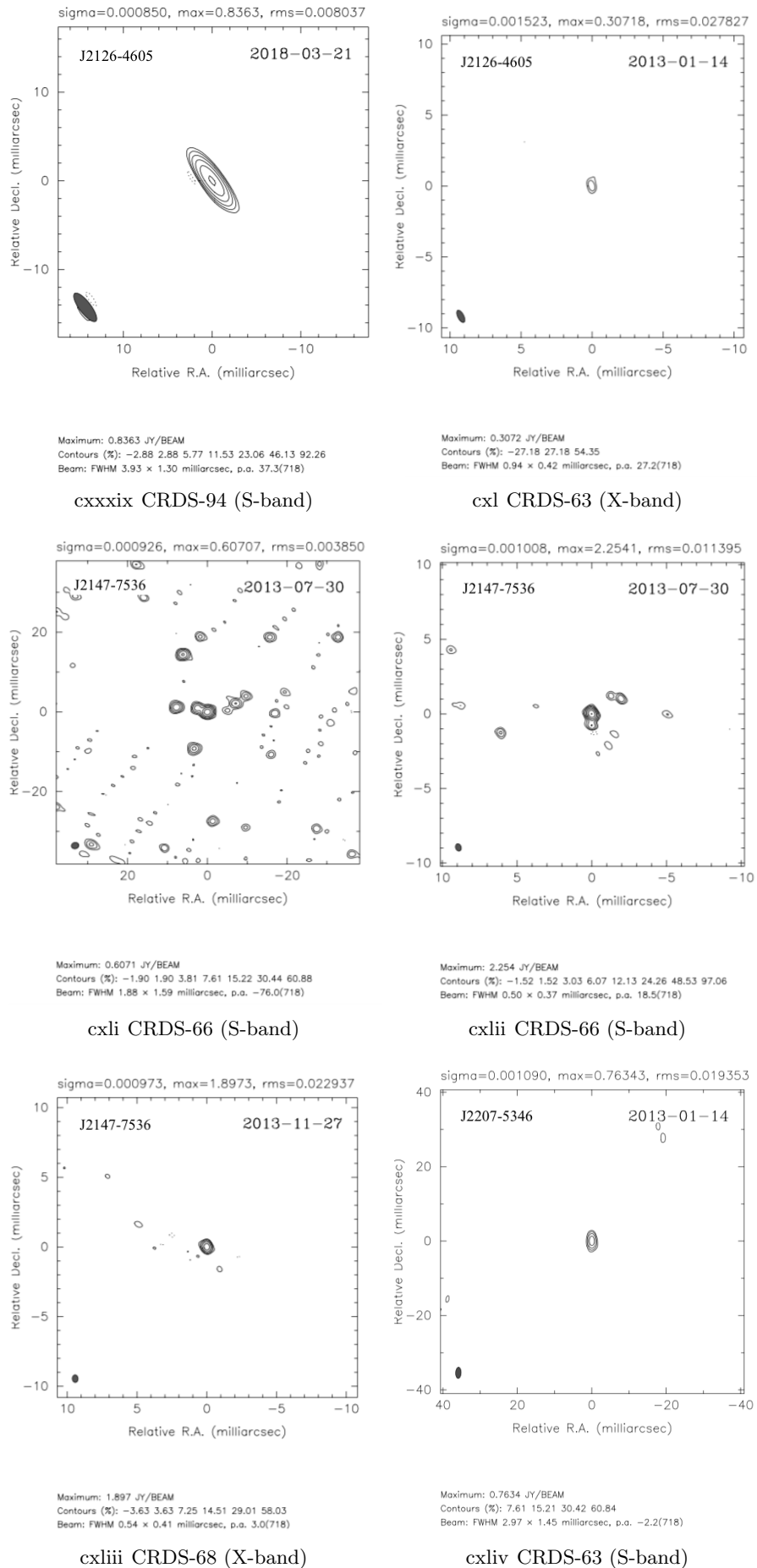
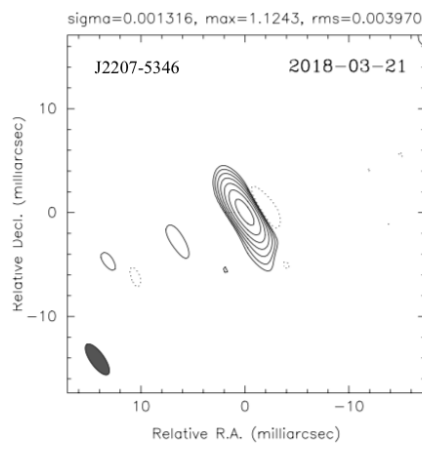
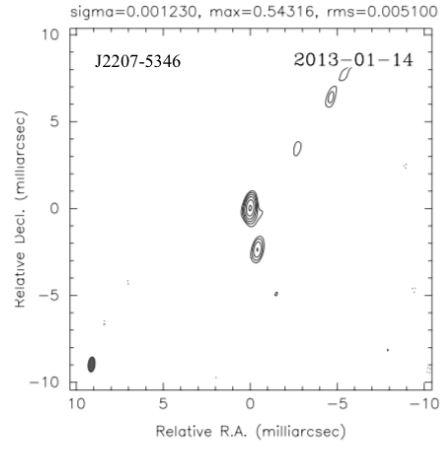


Figure 4.7 - Continued from previous page



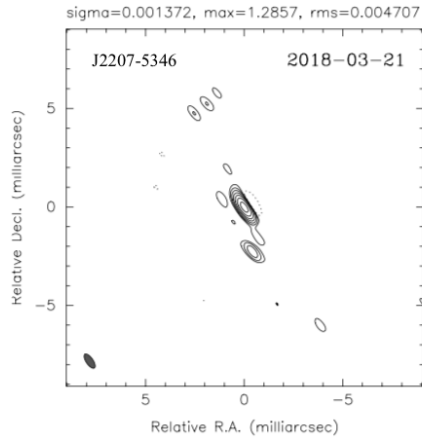
Maximum: 1.124 JY/BEAM
 Contours (%): -1.06 1.06 2.12 4.24 8.47 16.95 33.90 67.80
 Beam: FWHM 3.54 x 1.34 milliarcsec, p.a. 35.5(718)

cxlv CRDS-94 (S-band)



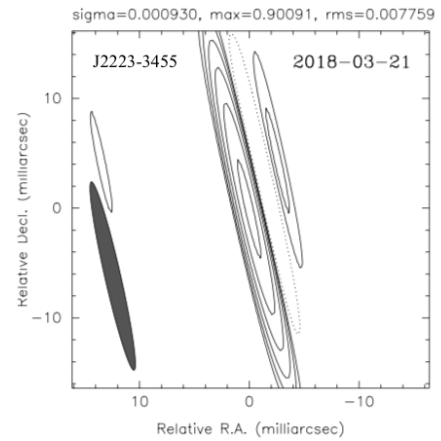
Maximum: 0.5432 JY/BEAM
 Contours (%): -2.82 2.82 5.63 11.27 22.53 45.07 90.14
 Beam: FWHM 0.86 x 0.39 milliarcsec, p.a. -5.7(718)

cxlvi CRDS-63 (X-band)



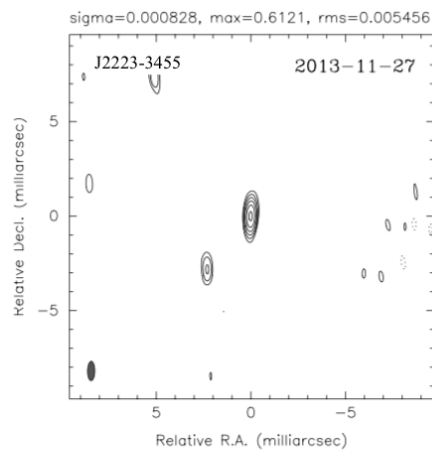
Maximum: 1.286 JY/BEAM
 Contours (%): -1.10 1.10 2.20 4.39 8.79 17.57 35.14 70.29
 Beam: FWHM 0.84 x 0.35 milliarcsec, p.a. 34.5(718)

cxlvii CRDS-94 (X-band)



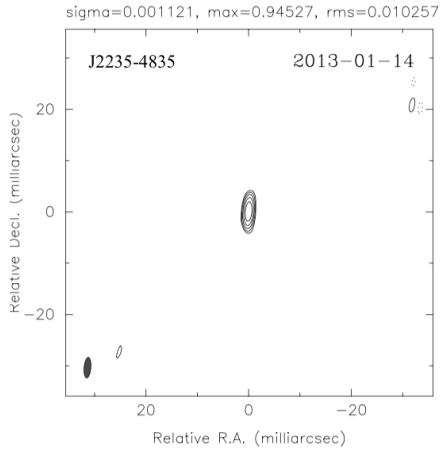
Maximum: 0.9009 JY/BEAM
 Contours (%): -2.58 2.58 5.17 10.33 20.67 41.34 82.68
 Beam: FWHM 17.60 x 1.44 milliarcsec, p.a. 12.8(718)

cxlviii CRDS-94 (S-band)



Maximum: 0.6121 JY/BEAM
 Contours (%): -2.67 2.67 5.35 10.70 21.39 42.78 85.57
 Beam: FWHM 1.02 x 0.38 milliarcsec, p.a. -0.5(718)

cxlix CRDS-68 (X-band)



Maximum: 0.9453 JY/BEAM
 Contours (%): -3.26 3.26 6.51 13.02 26.04 52.08
 Beam: FWHM 3.98 x 1.31 milliarcsec, p.a. -4.8(718)

cl CRDS-63 (S-band)

Figure 4.7 - *Continued from previous page*

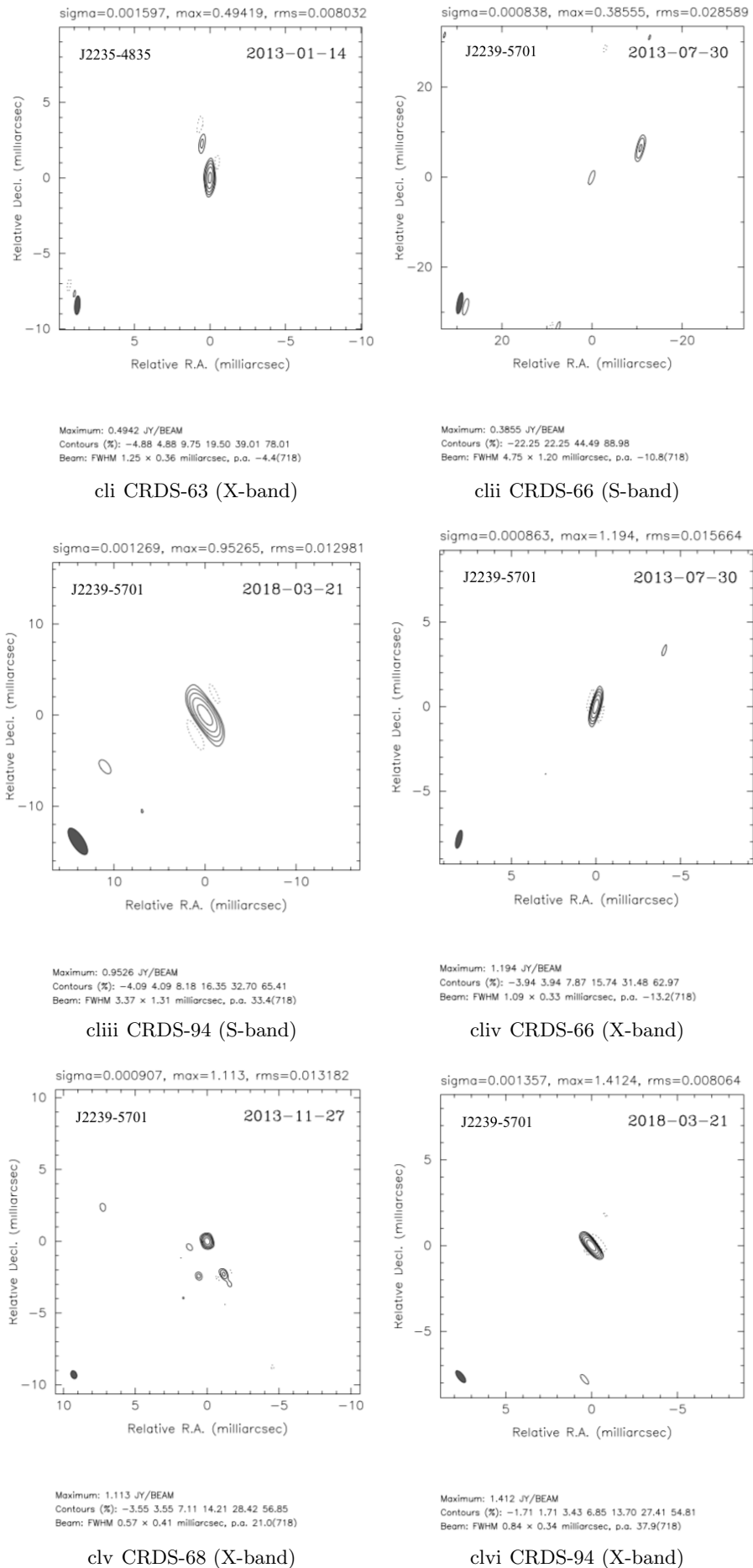
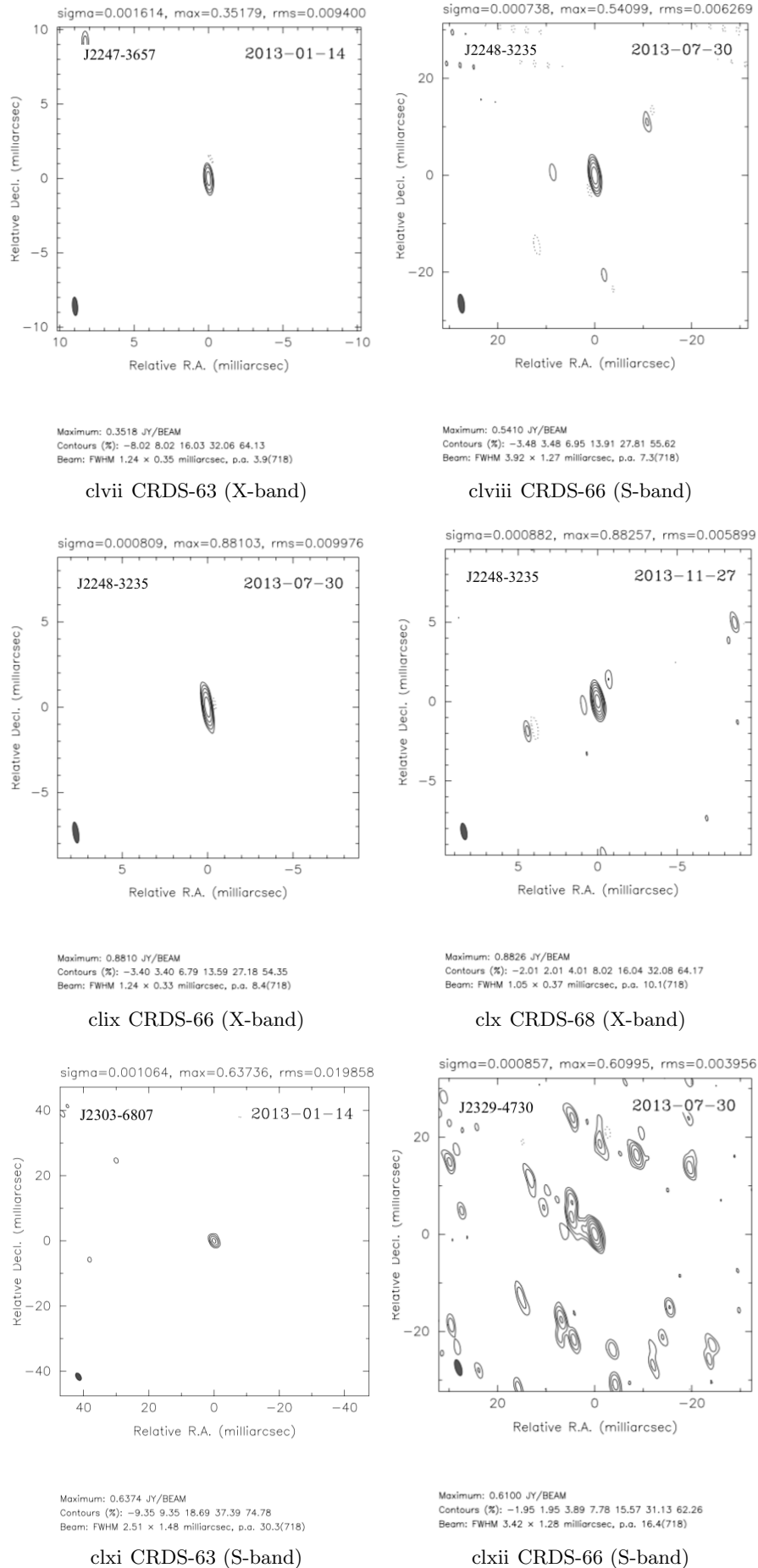
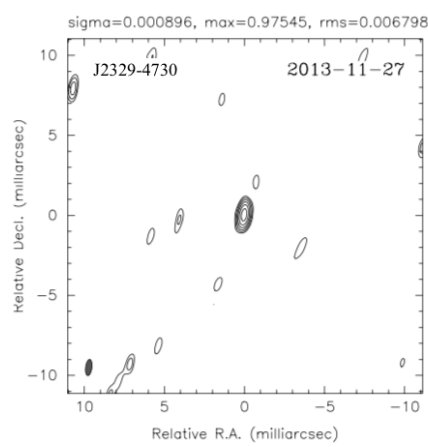


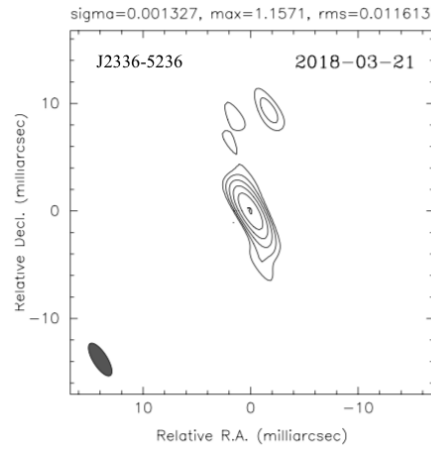
Figure 4.7 - Continued from previous page

Figure 4.7 - *Continued from previous page*



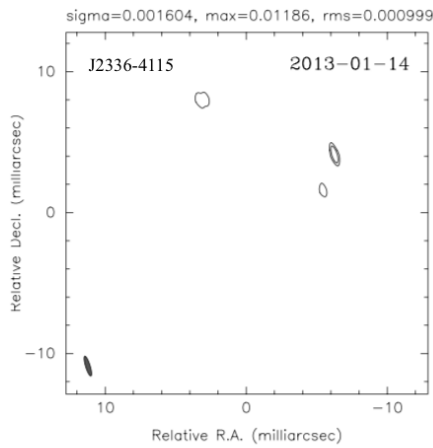
Maximum: 0.9754 JY/BEAM
 Contours (%): -2.09 2.09 4.18 8.36 16.73 33.45 66.90
 Beam: FWHM 1.01 x 0.39 milliarcsec, p.a. -7.2(718)

clxiii CRDS-68 (X-band)



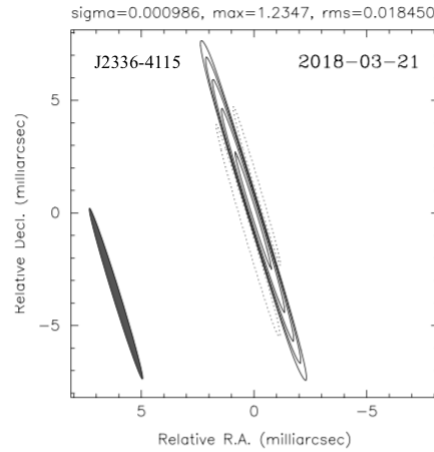
Maximum: 1.157 JY/BEAM
 Contours (%): -3.01 3.01 6.02 12.04 24.09 48.17 96.35
 Beam: FWHM 3.51 x 1.32 milliarcsec, p.a. 32.3(718)

clxiv CRDS-94 (S-band)



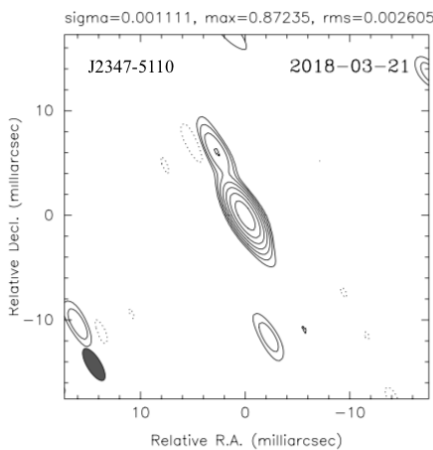
Maximum: 1.1860E-02 JY/BEAM
 Contours (%): 25.27 50.54
 Beam: FWHM 1.46 x 0.32 milliarcsec, p.a. 17.1(718)

clxv CRDS-63 (X-band)



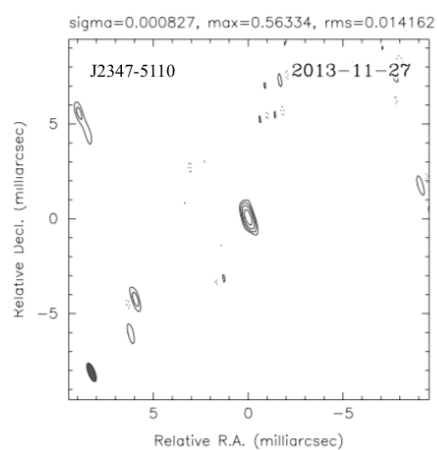
Maximum: 1.235 JY/BEAM
 Contours (%): -4.48 4.48 8.97 17.93 35.86 71.73
 Beam: FWHM 7.93 x 0.33 milliarcsec, p.a. 17.2(718)

clxvi CRDS-94 (X-band)



Maximum: 0.8723 JY/BEAM
 Contours (%): -0.90 0.90 1.79 3.58 7.17 14.33 28.67 57.34
 Beam: FWHM 3.51 x 1.32 milliarcsec, p.a. 31.4(718)

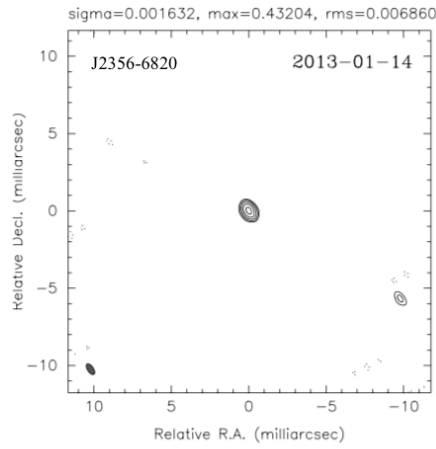
clxvii CRDS-94 (S-band)



Maximum: 0.5633 JY/BEAM
 Contours (%): -7.54 7.54 15.08 30.17 60.33
 Beam: FWHM 1.04 x 0.36 milliarcsec, p.a. 21.0(718)

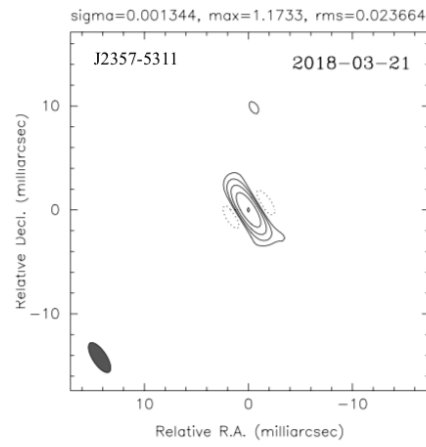
clxviii CRDS-68 (X-band)

Figure 4.7 - *Continued from previous page*



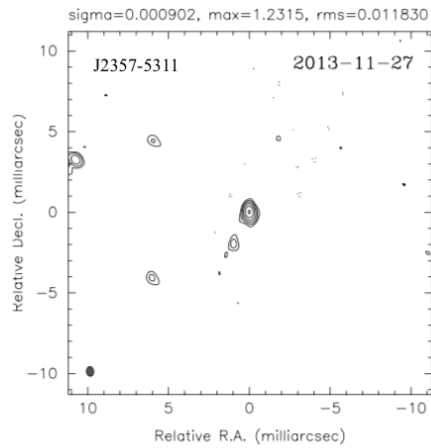
Maximum: 0.4320 JY/BEAM
Contours (%): -4.76 4.76 9.53 19.05 38.11 76.22
Beam: FWHM 0.80 × 0.38 milliarcsec, p.a. 33.3(718)

clxix CRDS-63 (X-band)



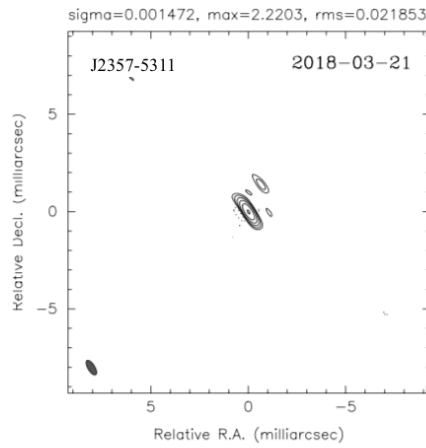
Maximum: 1.173 JY/BEAM
Contours (%): -6.05 6.05 12.10 24.20 48.41 96.81
Beam: FWHM 3.33 × 1.34 milliarcsec, p.a. 33.3(718)

clxx CRDS-94 (S-band)



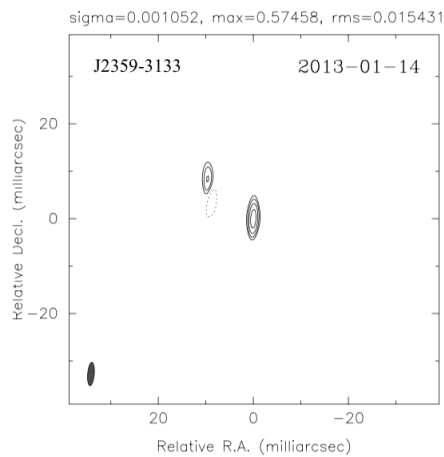
Maximum: 1.231 JY/BEAM
Contours (%): -2.88 2.88 5.76 11.53 23.06 46.11 92.22
Beam: FWHM 0.60 × 0.44 milliarcsec, p.a. 6.1(718)

clxxi CRDS-68 (X-band)



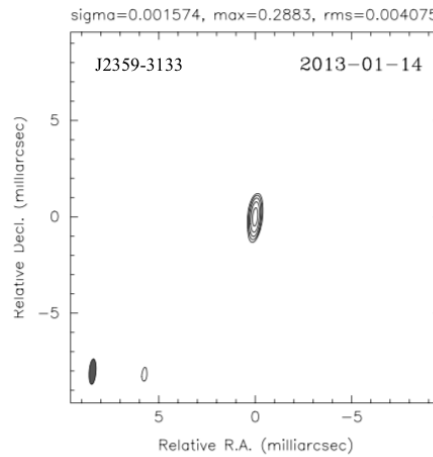
Maximum: 2.220 JY/BEAM
Contours (%): -2.95 2.95 5.91 11.81 23.62 47.24 94.49
Beam: FWHM 0.85 × 0.36 milliarcsec, p.a. 31.2(718)

clxxii CRDS-94 (X-band)



Maximum: 0.5746 JY/BEAM
Contours (%): -8.06 8.06 16.11 32.23 64.46
Beam: FWHM 4.92 × 1.38 milliarcsec, p.a. -4.6(718)

clxxiii CRDS-63 (S-band)



Maximum: 0.2883 JY/BEAM
Contours (%): 4.24 8.48 16.96 33.92 67.85
Beam: FWHM 1.32 × 0.35 milliarcsec, p.a. -4.3(718)

clxxiv CRDS-63 (X-band)

4.5 Discussion

In this work, I present VLBI contour maps of the 90 sources that was observed in four CRDS sessions. The findings in this work show that CRDS geodetic and astrometric sessions can be used for routine imaging purposes in the near future. In this section, I have combined all the results for each individual source and present them on a source-by-source basis. In each case, I discuss VLBI properties of the source and conclude with recommendations on the suitability of each source as a reference or calibrator source. In addition to the analysis from the VLBI contour maps, I also discuss structure variability (if any) in the sources using available VLBI contour maps in the RFC database (rfc_2019c). As a measure of total flux density variability, I calculate the range, which is the difference between the highest value and the lowest value of total flux density. It will give the reader an indication of how much the total flux density varies over the number of epochs.

Notes on individual sources

- **J0004-4736**

The source J0004-4736 is a defining source in the ICRF-3 catalogue. I present the VLBI map of the source at X-band, obtained from the CRDS-68 session. The total flux density is 0.853 Jy. The SC was measured to be 0.74 with an SI of 3.10. The higher SI is indicative of extended emission in the source which is detectable in the VLBI contour map in Figure 4.7. The μ is 0.40, and was calculated from 30 epochs of available data. Based on these results, the source should be used with caution when considered as a calibrator. I recommend that the source is regularly monitored at all frequencies of interest. The three contour maps of the source, between 2011 and 2017 from the RFC database (rfc_2019c), show the total flux density changing between 0.552 Jy and 0.224 Jy. The total flux density range is 0.328 Jy. The VLBI contour maps from the three epochs show the appearance and disappearance of a jet structure in the source.

- **J0040-5903**

The source J0040-5903 is an ICRF-3 non-defining source. This source was included in the CRDS-94 session to analyse its suitability as a defining source through imaging and astrometric quality assessments. I present the first-ever contour map of the source at S-band. The total flux density is 0.986 Jy and the SC was measured to be 0.93 with an SI of 1.75. The VLBI map in Figure 4.7 shows a compact structure that agrees with the SC and SI. The μ is 0.04, and was calculated from only two epochs of available data. Therefore, we cannot draw secure conclusions

about the flux density variability of the source. Based on the results, the source can be considered as a good calibrator. However, more observations are recommended in the near future for astrometric quality assessment at S- and X-band.

- **J0051-4226**

The source is an ICRF-3 defining source. The S- and X-band VLBI maps are obtained from the CRDS-63 session. At S-band, the total flux density is 0.826 Jy. The SC and SI are 0.98 and 1.75 respectively. The μ is 0.51, and was calculated from 155 epochs of available data. The VLBI contour map of the source in Figure 4.7 shows a compact nature of the source that agrees with the SC and SI. Based on the results, the source can be considered as a good calibrator source. Available VLBI maps in the RFC database (rfc_2019c) between 2002 and 2017 indicate a change in the total flux density between 0.722 Jy and 0.681 Jy. The range of the total flux density is 1.563 Jy from 14 epochs. The contour maps show a compact structure of the source. The source can be used as a good calibrator. At X-band, the total flux density is 0.400 Jy from the CRDS-63 map. The SC was measured to be 0.88 with an SI of 2.29. The μ is 0.51, and was calculated from 155 epochs of available data. The source shows a jet structure at X-band that can be seen in the map in Figure 4.7. Based on the results, the source may be considered as a calibrator but cautions should be taken while selecting the source. Multi-epoch contour maps in the RFC database (rfc_2019c) from 14 epochs between 2002 and 2017 indicate a change in the total density between 0.632 Jy and 0.512 Jy. The range of the total flux density is 0.450 Jy. The maps show the appearance and disappearance of a jet structure in the source.

- **J0106-4034**

The source J0106-4034 is a defining source in the ICRF-3. I present the VLBI map at X-band from the CRDS-68 session. A total flux density of 1.097 Jy is obtained from the map. The SC and SI are 1.00 and 2.65 respectively. The μ is 0.51, and was calculated from 1268 epochs of available data. The source may be used as a good calibrator but cautions should be taken when selecting the source. The VLBI contour map in Figure 4.7 shows a possible second component to the core. The available contour maps in the RFC database (rfc_2019c) between 1994 and 2017 show the total flux density changing between 0.006 Jy and 1.226 Jy. The range of the total flux density from 64 epochs is 4.510 Jy. Multiple epoch VLBI maps show source structure variability in the source with the appearance and disappearance of a jet structure.

- **J0109-6049**

The source is an ICRF-3 defining source. The VLBI map at X-band in Figure 4.7 is from the CRDS-63 session. The total flux density of the source is 0.339 Jy. The SC and SI are 0.87 and 2.30 respectively. The μ is 0.27, and was calculated from 26 epochs of available data. The VLBI contour map in the figure shows a possible second component to the core. The source may be used as a good calibrator but cautions should be taken. The only X-band contour map in the RFC database (rfc_2019c) from the epoch in 2010 shows a total flux density of 0.414 Jy a jet structure in the source.

- **J0133-5200**

The source J0133-5200 is an ICRF-3 reference source. I present the first-ever VLBI maps of this source at X-band, obtained from the CRDS-66 and -68 sessions. The total flux density is 0.602 and 1.151 Jy, respectively. The calculated SC is 1.08 and 0.67, respectively, and the SI is 1.25 and 2.20 respectively. The μ is 0.63, and was calculated from 252 epochs of available data. Both the SC and the SI indicate that the source is compact in nature which also agrees with the contour maps of the source, shown in Figure 4.7. Based on the results, the source can be considered as a good calibrator.

- **J0229-7847**

The source is an ICRF-3 defining source. I present the first-ever VLBI maps at S- and X-band, obtained from the CRDS-63 session. At S-band, the total flux density obtained is 0.929 Jy from the map. The SC was measured to be 1.00 with an SI of 1.60. The μ is 0.41, and is calculated from 46 epochs of available data. The VLBI contour map shows a compact structure that also agrees with the SC and SI. Based on the results, the source can be considered as a good calibrator. The total flux density at X-band is 0.527 Jy. The SC is 1.00 and the SI is 1.75. The μ is 0.47, and was calculated from 46 epochs of available data. The X-band map shows a compact structure of the source. The source, based on the results, can be considered as a good calibrator.

- **J0236-6136**

The source is an ICRF-3 defining source. I present the VLBI map at X-band from the CRDS-68 session. The total flux density is 0.606 Jy. The SC was measured to be 0.99 with an SI of 1.65. The μ is 0.27, and was calculated from 23 sessions of available data. The VLBI contour map in Figure 4.7 shows a compact structure that agrees with the SC and SI. Based on the results, the source can be considered as a good calibrator. The only available X-band map of the source in the RFC

database (rfc_2019c) is from the epoch in 2010 when a total flux density of 0.292 Jy was obtained. The map shows a compact structure of the source.

- **J0253-5441**

The source is a non-defining source in the ICRF-3 catalogue. I present the first-ever VLBI map at S-band from the CRDS-94 session. The total flux density is 1.645 Jy and the SC was measured to be 1.00 and an SI of 1.30. The μ is 0.84, and was calculated from four sessions of available data. At S-band, the source is compact in nature which can be seen in Figure 4.7 that also agrees with the SC and SI. The source can be considered as a good calibrator. CRDS X-band observations will be used in the near future to analyse the astrometric quality of the source.

- **J0303-6211**

The source is a reference source in the ICRF-3 catalogue. I present the first-ever contour maps at S- and X-band from the CRDS-63 session. At S-band, the total flux density is 1.437 Jy. The SC was measured to be 1.09 with an SI of 1.20. The μ is 0.29, and was calculated from 51 epochs of available data. The VLBI contour map in Figure 4.7 shows a point-like structure that agrees with the SC and SI. Based on the results, the source can be considered as a good calibrator. At X-band, the total flux density is 0.637 Jy. The SC and SI are 0.78 and 1.95 respectively. The μ is 0.44, and was calculated from 51 epochs of available data. At X-band, the source shows a compact structure (Figure 4.7) that agrees with the SC and SI. The X-band astrometric quality assessments indicate that the source can be considered as a good calibrator source.

- **J0309-6058**

The source is an ICRF-3 defining source. I present the first-ever contour maps of the source. The VLBI map at S-band is from the CRDS-66 session and the map at X-band is from the CRDS-68 session. At S-band, the total flux density is 1.61 Jy from the CRDS-66 map. The SC and SI are 0.90 and 1.31 respectively. The μ is 0.94, and was calculated from 713 epochs of available data. The VLBI contour map of the source in Figure 4.7 shows a compact structure that agrees with the SC and SI. The source can be considered as a good calibrator. At X-band, the total flux density is 1.305 Jy from the CRDS-68 map. The SC and SI are 1.00 and 1.23 respectively. The μ is 0.69, and was calculated from 713 epochs of available data. In Figure 4.7, the VLBI contour map shows a compact structure of the source that agrees with the SC and SI. Overall, the source can be considered as a good calibrator source.

- **J0334-4008**

The source is a defining source in the ICRF-3 catalogue. I present the VLBI maps of the source at S- and X-band, obtained from the CRDS-63 session. At S-band, the total flux density is 1.419 Jy. The SC and SI are 1.00 and 1.20 respectively. The μ is 0.22, and was calculated from 670 epochs of available data. The VLBI contour map in Figure 4.7 shows a compact structure of the source that agrees with the SC and SI. Based on these results, the source can be considered as a good calibrator. The VLBI contour maps in the RFC database (rfc_2019c) from 23 epochs between 2005 and 2017 show the total flux density changing between 0.572 Jy and 1.198 Jy. The flux density range is 1.303 Jy. Multi-epoch contour maps show the appearance and disappearance of a jet structure in the source. At X-band, the total flux density is 1.525 Jy. The SC and SI are 1.00 and 1.23 respectively. The μ is 0.33, and was calculated from 670 epochs of available data. The VLBI contour map in Figure 4.7 shows a compact structure of the source that agrees with the SC and SI. Based on the results, the source can be considered as a good calibrator. Multi-epoch contour maps in the RFC database (rfc_2019c) between 2005 and 2017 show the total flux density changing between 0.661 Jy and 0.852 Jy. The flux density range at X-band is 2.339 Jy from 23 epochs. The maps show significant variability in the source structure. I recommend that the cautions should be taken when selecting the source as a calibrator.

- **J0335-5430**

The source is an ICRF-3 reference source. I present the first-ever VLBI map at S-band from the CRDS-94 session. The VLBI maps at X-band are from the CRDS-66 and -68 sessions respectively. At S-band, a total flux density of 0.917 Jy is obtained. The SC and SI are 0.94 and 1.75 respectively. The μ is 0.24, and was calculated from 16 epochs of available data. The S-band, the map in Figure 4.7 shows a compact structure of the source that agrees with the SC and SI. Based on the results, the source can be considered as a good calibrator. At X-band, the total flux density is 0.686 Jy from the CRDS-66 map and 0.881 Jy from the CRDS-68 map. The calculated SC is 0.77 and 0.97, respectively, and the SI is 1.60 and 1.20, respectively. The μ is 0.19, and was calculated from 16 epochs of available data. Both the SC and the SI indicate that the source is compact in nature which also agrees with the contour maps of the source, shown in Figure 4.7. The source can be considered as a good calibrator. The only image in the RFC database from the epoch in 2010 shows a total flux density of 0.559 Jy. The VLBI contour map shows a compact structure of the source.

- **J0403-3605**

The source is an ICRF-3 defining source. I present S- and X-band VLBI maps from the CRDS-63 session. At S-band, the total flux density is 0.786 Jy. The SC and SI are 1.00 and 1.30 respectively. The μ is 0.40, and was calculated from 659 epochs of available data. The VLBI contour map in Figure 4.7 shows a compact nature of the source that agrees with the SC and SI. Based on the results, the source can be considered as a good calibrator. The contour maps in the RFC database (rfc_2019c) are from 45 epochs, between 1998 and 2017 show the flux density changing between 1.159 Jy and 1.208 Jy. The range of the total flux density is 0.512 Jy. The contour maps of the source show a jet structure appearing and disappearing over the epochs. At X-band, the total flux density is 1.317 Jy. The SC was measured to be 1.00 with a SI of 2.20. The μ is 0.80, and was calculated from 659 epochs of available data. In Figure 4.7, the source shows a compact structure that agrees with the SC and SI. The source can be considered as a good calibrator. The VLBI maps in the RFC database (rfc_2019c) are from 45 epochs between 1998 and 2017 show the flux density changing between 1.337 Jy and 2.280 Jy. The flux density range is 2.327 Jy. Multi-epoch maps show source structure variability with the appearance and disappearance of a jet structure.

- **J0406-3826**

The source J0406-3826 is an ICRF-3 reference source. I present the VLBI maps at X-band from the CRDS-66 and -68 session. The total flux density is 1.376 Jy from the CRDS-66 map and 1.591 Jy from the CRDS-68 map. The SC is 0.85 and 0.98, respectively, and the SI is 1.30 and 2.20, respectively. The VLBI contour maps of the source in Figure 4.7 show source structure variability over two epochs. In the first epoch, the source shows a compact structure, however, in the second epoch, a jet structure is detected. The μ is 0.67, and was calculated from 393 epochs of available data. The analysis suggests that the source can be considered as a calibrator but cautions should be taken when selecting the source. Multi-epoch VLBI maps in the RFC database (rfc_2019c) at X-band from 16 epochs between 2004 and 2017 show a change in total flux density between 1.329 Jy and 1.016 Jy. The range of the total flux density is 0.610 Jy. The contour maps show source structure variability with a jet structure appearing and disappearing. The imaging and structure analysis at S-band are suggested using CRDS sessions in the near future.

- **J0439-4522**

The source is an ICRF-3 defining source. I present the VLBI map at X-band from the CRDS-63 session when a total flux density of 0.673 Jy is measured. The

calculated SC is 0.81 with an SI of 2.35. The VLBI contour map of the source in Figure 4.7 shows a compact structure that agrees with the SC and SI. The μ is 0.41, and was calculated from 139 epochs of available data. Based on the results, the source can be considered as a good calibrator. Multi-epoch VLBI maps at X-band in the RFC database (rfc_2019c) are from 6 epochs between 2007 and 2017. The total flux density changes between 0.452 Jy and 0.889 Jy. The range of the total flux density is 0.790 Jy. The maps show a compact structure of the source. The imaging and structure analysis are suggested at S-band using CRDS sessions in the near future.

- **J0450-8101**

The source is an ICRF-3 defining source. I present the VLBI map at S-band from the CRDS-66 session. The VLBI maps at X-band are from the CRDS-66 and -68 sessions. At S-band, the total flux density is 2.239 Jy. The SC and SI are 0.43 and 1.35 respectively. The μ is 0.35, and was calculated from 121 epochs of available data. The VLBI contour map in Figure 4.7 shows a point-like source structure which agrees with the SC and SI. Based on the results, the source can be considered as a good calibrator. The VLBI map in the RFC database (rfc_2019c) is from 2011 when a total flux density of 0.949 Jy was obtained. The map shows a compact structure of the source. At X-band, the total flux density is 1.577 Jy from the CRDS-66 map and 1.397 Jy from the CRDS-68 map. The SC is 1.00 and 0.95, respectively, and the SI is 1.32 and 1.23, respectively. The μ is 0.27, and was calculated from 121 epochs of available data. The VLBI contour maps in Figure 4.7 at both epochs show a point-like structure which agrees with the SC and SI. The source can be considered as a good calibrator. The VLBI map available in the RFC database (rfc_2019c) is from 2011 when a total flux density of 1.516 Jy was obtained. The map shows a compact structure of the source.

- **J0506-6109**

The source is a defining source in the ICRF-3 catalogue. I present the first-ever VLBI maps at S- and X-band from the CRDS-63 session. At S-band, the total flux density is 0.639 Jy. The SC and SI are 0.82 and 1.21 respectively. The μ is 0.45, and was calculated from 153 epochs of available data. The VLBI contour map in Figure 4.7 shows a compact structure that agrees with the SC and SI. Based on the results, the source can be considered as a good calibrator. At X-band, the total flux density is 0.422 Jy. The SC is 0.73 and SI is 1.45. The μ is 0.27, and was calculated from 153 epochs of available data. Figure 4.7 shows a compact structure that agrees with the SC and SI. The source can be considered as a good calibrator source.

- **J0516-6207**

The source is a reference source in the ICRF-3 catalogue. I present the first-ever VLBI maps at S- and X-band from the CRDS-66 session. At S-band, the total flux density is 2.737 Jy. The SC and SI are 0.99 and 2.75 respectively. The μ is 0.23, and was calculated from 82 epochs of available data. The VLBI contour map in Figure 4.7 shows a jet structure to the compact core. Based on the results, I recommend that cautions should be taken when selecting the source as a calibrator at S-band. At X-band, the total flux density is 1.343 Jy. The SC and SI are 0.99 and 1.10 respectively. The μ is 0.31, and was calculated from 82 epochs of available data. The VLBI contour map in Figure 4.7 shows a point-like structure. The source can be considered as a good calibrator at X-band.

- **J0525-4557**

The source J0525-4557 is an ICRF-3 reference source. I present the first-ever X-band VLBI map from the CRDS-68 session. The total flux density is 0.710 Jy. The SC was measured to be 0.80 with an SI of 2.75. The μ is 0.59, and was calculated from 39 epochs of available data. The map in Figure 4.7 shows a jet structure. More imaging is recommended to confirm the jet structure in the source. I suggest that the source should be used with caution when considered as a calibrator. It is recommended that the source be regularly monitored in the near future at all frequencies of interest.

- **J0526-4830**

The source J0526-4830 is an ICRF-3 reference source. I present the VLBI maps at S- and X-band from the CRDS-63 session. At S-band, the total flux density is 0.781 Jy. The SC was measured to be 0.77 with a SI of 1.10. There is no flux density available on the GSFC server, therefore the μ was not calculated. The VLBI contour map in Figure 4.7 shows a compact structure that agrees with the SC and SI. Based on the results, the source can be considered as a good calibrator. The contour maps in the RFC database (rfc.2019c) are from four epochs between 2012 and 2016. The flux density, between the epochs, changes between 0.331 Jy and 0.314 Jy. The range of the flux density is 0.199 Jy. The VLBI maps show a jet structure in the source. At X-band, the total flux density is 0.428 Jy. The SC and SI are 0.89 and 1.60 respectively. There is no flux density available on the GSFC server, therefore the μ is not calculated. The VLBI map in Figure 4.7 shows a compact structure that agrees with the SC and SI. Based on the results, the source can be considered as a good calibrator. Multi-epoch VLBI maps at X-band in the RFC database (rfc.2019c) are from four epochs between 2012 and 2016. The flux density, between the epochs, changes between 0.441 Jy 0.580 Jy. The range of the

total flux density is 0.328 Jy. The maps show source structure variability in the source with a jet structure appearing and disappearing.

- **J0534-6106**

In the ICRF-3 catalogue, the source J0534-6106 is a reference source. I present the first-ever VLBI map at X-band from the CRDS-68 session. The total flux density obtained is 0.861 Jy. The SC and SI are 0.71 and 1.10 respectively. The μ is 0.29, and was calculated from 30 epochs of available data. The VLBI contour map in Figure 4.7 shows a point-like structure of the source that agrees with the SC and SI. The results from the astrometric quality assessment suggest that the source can be used as a very good calibrator.

- **J0536-3401**

The source is a defining source in the ICRF-3 catalogue. I present the VLBI map at X-band from the CRDS-63 session. A total flux density of 0.309 Jy is obtained. The SC was measured to be 1.00 with an SI of 1.40. The μ is 0.54, and was calculated from 105 epochs of available data. The VLBI contour map in Figure 4.7 shows a compact structure that agrees with the SC and SI. Based on the results, the source can be considered as a good calibrator. The contour maps in the RFC database (rfc.2019c) from 26 epochs between 2002 and 2017 show the flux density changing between 0.475 Jy and 0.283 Jy. Range of the total flux density is 0.541 Jy from 26 epochs. The maps show structure variability with a jet structure appearing and disappearing.

- **J0538-4405**

The source is an ICRF-3 reference source. I present the VLBI map at S-band from the CRDS-66 session. The VLBI maps at X-band are from the CRDS-66 and -68 session respectively. At S-band, the total flux density is 4.045 Jy. The SC was measured to be 0.63 with an SI of 1.10. The μ is 0.59, and was calculated from 1562 epochs of available data. The VLBI contour map in Figure 4.7 shows a compact structure that agrees with the SC and SI. The source can be considered as a good calibrator at S-band. The VLBI contour maps in the RFC database (rfc.2019c) from 48 epochs between 1995 and 2017 show a change in the flux density between 4.386 Jy and 3.418 Jy. The total flux density range is 7.022. Multi-epoch contour maps show a compact structure of the source. At X-band, the total flux density is 3.397 Jy from the CRDS-66 map and 0.861 Jy from the CRDS-68 map. The SC is 0.71 and 0.71, respectively, and the SI is 2.45 and 1.10, respectively. The μ is 0.62, and was calculated from 1562 epochs of available data. The VLBI maps in Figure 4.7 show a compact structure that agrees with the SC and SI. Based on the results, the source can be considered as a good calibrator. However, considering

the difference in the SI, I suggest more imaging of the source. Multi-epoch contour maps in the RFC database (rfc_2019c) are from 48 epochs between 1995 and 2017. The total flux density changes between 5.277 Jy and 1.489 Jy. The range of the total flux density is 6.097 Jy. The maps show structure variability with a jet structure appearing and disappearing.

- **J0550-5732**

The source is an ICRF-3 reference source. I present the first-ever VLBI maps of the source at S-band from the CRDS-63 and -94 sessions. The first-ever VLBI map at X-band is from the CRDS-63 session. At S-band, the total flux density is 0.836 Jy from the CRDS-63 map and 1.067 Jy from the CRDS-94 map. The SC is 0.54 and 1.20, respectively, and the SI is 0.95 and 1.60, respectively. The μ is 0.24, and was calculated from 41 epochs of available data. The VLBI contour maps in Figure 4.7 show a compact structure at both epochs that agrees with the SC and SI. The results suggest that the source can be considered as a good calibrator. At X-band, the total flux density is 0.572 Jy. The SC and SI are 0.66 and 2.52 respectively. The μ is 0.25, and was calculated from 41 epochs of available data. The VLBI map in Figure 4.7 shows a jet-like structure that agrees with the SC and SI. The source may be considered as a good calibrator but more imaging is suggested to monitor the source structure variability.

- **J0922-3959**

The source is a reference source in the ICRF-3 catalogue. I present the VLBI maps at X-band from the CRDS-66 and -68 sessions. The total flux density is 1.219 Jy from the CRDS-66 map and 1.191 Jy from the CRDS-68 map. The SC is 0.70 and 1.30, respectively, and the SI is 0.76 and 1.40, respectively. The μ is 0.42, and was calculated from 739 epochs of available data. The VLBI maps in Figure 4.7 shows a compact structure at each epoch that agrees with the SC and SI. Based on the results, the source can be considered as a good calibrator. The X-band contour maps in the RFC database (rfc_2019c) from 72 epochs between 1998 and 2017, show flux density changing between 1.569 Jy and 0.964 Jy. The range of the total flux density is 0.815 Jy. The contour maps show a compact structure of the source over the majority of the epochs.

- **J0930-8533**

The source is an ICRF-3 reference source. I present the first-ever VLBI map at S-band from the CRDS-94 session. A total flux density of 1.076 Jy is obtained. The SC was measured to be 0.92 with an SI of 1.40. The μ is 0.09, and was calculated from only two epochs. The VLBI contour map in Figure 4.7 shows a

compact structure that agrees with the SC and SI. The VLBI analysis suggests that the source can be considered as a good calibrator.

- **J1006-5018**

The source is a defining source in the ICRF-3 catalogue. I present the VLBI map at X-band from the CRDS-63 session. The total flux density is 0.653 Jy. The SC and SI are 0.96 and 1.45 respectively. The μ is 0.47, and was calculated from 168 epochs of available data. The VLBI map in Figure 4.7 shows a compact structure that agrees with the SC and SI. Based on the results, the source can be used as a good calibrator. The only X-band contour map available in the RFC database (rfc_2019c) is from 2012 when a total flux density of 0.750 Jy was obtained. The map shows a compact structure of the source.

- **J1014-4508**

The source is an ICRF-3 reference source. I present the VLBI maps at S- and X-band from the CRDS-94 session. The S-band contour map is the first-ever map of the source. At S-band, the total flux density is 1.400 Jy. The SC was measured to be 0.89 with an SI of 1.52. The μ is 0.45, and was calculated from 10 epochs of available data. The VLBI contour map in Figure 4.7 shows a compact structure of the source that agrees with the SC and SI. The source can be considered as a good calibrator source. At X-band, the total flux density is 1.328 Jy. The SC and SI are 0.90 and 2.40 respectively. The μ is 0.45, and was calculated from 10 epochs of available data. The VLBI map in Figure 4.7 shows a jet-like structure. I suggest that cautions should be taken when considering the source as a calibrator. The VLBI map available in the RFC database (rfc_2019c) is from 2002 when a total flux density of 2.945 Jy was obtained.

- **J1023-6646**

The source is an ICRF-3 defining source. I present the first-ever VLBI map at S-band from the CRDS-94 session. The VLBI maps at X-band are from the CRDS-66 and -68 sessions. At S-band, the total flux density is 0.946 Jy. The SC is 0.95 and the SI is 1.20. The μ is 0.18, and was calculated from 32 epochs of available data. The S-band map in Figure 4.7 shows a compact structure of the source that agrees with the SC and SI. The VLBI analysis suggests that the source can be considered as a very good calibrator. At X-band, the total flux density is 0.792 Jy from the CRDS-66 map and 1.005 Jy from the CRDS-68 map. The SC is 0.94 and 0.90, respectively, and the SI is 1.10 and 2.10, respectively. The μ is 0.25, and was calculated from 32 epochs of available data. At X-band, the source shows a compact structure at the first epoch and a jet structure at the second epoch (Figure 4.7). Based on the results, I suggest that the source may be selected as a

calibrator but cautions should be taken when selecting the source. The only VLBI contour map available in the RFC database (rfc_2019c) is from 2010 where a total flux density of 0.434 Jy was measured. The contour map shows the presence of a possible second component in the source. I recommend more imaging of this source in the near future to monitor the jet structure.

- **J1036-3744**

The source J1036-3744 is an ICRF-3 defining source. I present the VLBI map at X-band from the CRDS-63 session. The total flux density is 0.519 Jy. The SC was measured to be 0.89 with an SI of 1.52. The μ is 0.45, and was calculated from 42 epochs of available data. The VLBI contour map in Figure 4.7 shows a compact structure that agrees with the SC and SI. The VLBI analysis suggests that the source can be considered as a good calibrator. Multi-epoch X-band contour maps in the RFC database (rfc_2019c) from 21 epochs between 2005 and 2017 show the flux density changing between 0.490 Jy and 0.358 Jy. The range of total flux density is 0.434 Jy from 21 epochs. The contour maps show that the source has a compact structure.

- **J1041-4740**

The source is an ICRF-3 reference source. I present VLBI maps at S- and X-band from the CRDS-94 session. At S-band, the total flux density is 1.016 Jy. The SC was measured to be 0.92 with an SI of 1.30. The μ was not calculated due to lack of information on the GSFC server. The VLBI contour map in Figure 4.7 shows a compact structure of the source that agrees with the SC and SI. The results from the astrometric quality assessments suggest that the source can be considered as a good calibrator. Multi-epoch S-band contour maps in the RFC database (rfc_2019c) from three epochs between 2014 and 2017 show the total flux density changing between 1.060 Jy and 1.563 Jy. The range of the total flux density is 0.952 Jy. The contour maps in the RFC database show a jet structure appearing and disappearing over the epochs. At X-band, a total flux density 2.195 Jy is obtained. The SC and SI are 0.99 and 1.75 respectively. On the GSFC server, there is no flux density available to calculate the μ . The VLBI contour map in Figure 4.7 shows a compact structure. The VLBI analysis suggests that the source can be considered as a good calibrator. Multi-epoch X-band contour maps available in the RFC database (rfc_2019c) from three epochs between 2014 and 2017 show the total flux density changing between 1.531 Jy and 1.292 Jy. The range of the total flux density is 1.408 Jy. The contour maps from the three epochs show a compact structure of the source.

- **J1047-6217**

The source is an ICRF-3 reference source. I present the first-ever VLBI maps at S- and X-band contour maps from the CRDS-94 session. The total flux density at S-band is 1.154 Jy. The SC and SI are 0.88 and 2.95 respectively. The μ is 0.14, and was calculated from 8 epochs of available data. The VLBI contour map in Figure 4.7 shows a jet-like structure that agrees with the SC and SI. The source can be used with caution when considered as a calibrator. At X-band, the total flux density obtained is 2.443 Jy. The SC and SI are 0.77 and 1.23 respectively. The μ is 0.13, and was calculated from 8 epochs of available data. The source shows a compact structure in Figure 4.7 that agrees with the SC and SI. The VLBI analysis suggests that the source can be considered as a good calibrator.

- **J1103-5357**

The source is a defining source in the ICRF-3 catalogue. I present the first-ever VLBI maps at S- and X-band from the CRDS-94 session and -68 session respectively. At S-band, the total flux density is 0.876 Jy. The SC was measured to be 1.01 with an SI of 1.60. The μ is 0.44, and was calculated from 24 epochs of available data. The S-band contour map in Figure 4.7 shows a compact structure that agrees with the SC and SI. I suggest that the source can be considered as a good calibrator. At X-band, I obtain a total flux density of 0.845 Jy. The SC and SI are 0.77 and 1.60 respectively. The μ is 0.36, and was calculated from 24 epochs of available data. The contour map in Figure 4.7 shows a compact structure of the source that agrees with the SC and SI. The VLBI analysis at X-band suggests that the source can be considered as a good calibrator.

- **J1118-4638**

The source J1118-4638 is an ICRF-3 defining source. I present the first-ever VLBI maps at S- and X-band from the CRDS-94 session. At S-band, the total flux density is 0.986 Jy. The SC was measured to be 0.91 with an SI of 1.20. The μ is 0.30, and was calculated from 12 epochs of available data. The S-band contour map in Figure 4.7 shows a compact structure of the source that agrees with the SC and SI. The VLBI analysis suggests that the source can be used as a good calibrator. At X-band, I obtain a total flux density of 1.757 Jy. The SC was measured to be 0.96 with an SI of 2.10. The μ is 0.24, and was calculated from 12 epochs of available data. The VLBI map in Figure 4.7 shows a compact structure that agrees with the SC and SI. Based on the results, the source can be used as a good calibrator.

- **J1131-5818**

The source is an ICRF-3 source. I present the VLBI maps at S- and X-band from the CRDS-94 session. The map at S-band is the first-ever VLBI map of the source. At S-band, the total flux density is 0.951 Jy. The SC and SI are 0.93 and 1.30 respectively. The μ is 0.51, and was calculated from four epochs of available data. The VLBI contour map in Figure 4.7 shows a compact structure that agrees with the SC and SI. The VLBI analysis suggests that the source can be considered as a very good calibrator. At X-band, the total flux density is 2.429 Jy. The SC and SI are 0.76 and 2.60 respectively. The μ is 0.17, and was calculated from four epochs of available data. The X-band contour map in Figure 4.7 shows a jet-like structure. The VLBI analysis suggests that the source should be used with caution when considered as a calibrator. The only available X-band contour map in the RFC database (rfc_2019c) is from the epoch in 2010 when a total flux density of 1.523 Jy was obtained. The X-band contour map in the RFC database shows a compact structure of the source in the epoch.

- **J1145-6954**

The source is an ICRF-3 defining source. I present the first-ever VLBI map at S-band from the CRDS-63 and -94 sessions. The VLBI map at X-band is from the CRDS-63 session. At S-band, I obtain a total flux density of 0.463 Jy from the CRDS-63 map and 0.827 Jy from the CRDS-94 map. The SC is 0.53 and 2.20, respectively, and the SI is 1.00 and 1.60, respectively. The μ is 0.30, and was calculated from 25 epochs of available data. The S-band contour map in Figure 4.7 shows a compact structure that agrees with the SC and SI. The astrometric quality assessment results suggest that the source can be used as a good calibrator. At X-band, the total flux density is 0.420 Jy. The SC was measured to be 0.71 with an SI of 1.25. The μ is 0.28, and was calculated from 25 epochs of available data. The VLBI map in Figure 4.7 shows a point-like structure of the source that agrees with the SC and SI. The astrometric quality assessment results suggest that the source is a very good calibrator. The only X-band contour map of the source available in the RFC database (rfc_2019c) is from the epoch in 2010 when a total flux density of 0.879 Jy was measured. The available contour map also shows a compact structure of the source.

- **J1147-3812**

The source is an ICRF-3 defining source. I present the VLBI map at S-band from the CRDS-66 session. The VLBI maps at X-band are from the CRDS-66 and -68 sessions. At S-band, the total flux density obtained is 2.842 Jy. The SC was measured to be 0.38 with an SI of 1.20. The μ is 0.37, and was calculated

from 1334 epochs of available data. The VLBI contour map in Figure 4.7 shows a compact structure of the source that agrees with the SC and SI. The astrometric quality assessment results suggest that the source can be considered as a good calibrator. Multi-epoch contour maps in the RFC database (rfc_2019c) from 65 epochs between 1998 and 2017 show the total flux density changing between 1.171 Jy and 1.138 Jy. The total flux density range is 1.378 Jy. The contour maps show a compact structure of the source in most of the epochs. At X-band, the total flux density is 2.309 Jy from the CRDS-66 map and 3.876 Jy from the CRDS-68 map. The SC is 0.98 and 0.91, respectively, and the SI is 1.15 and 2.20, respectively. The μ is 0.40, and was calculated from 1334 epochs of available data. The VLBI contour maps in Figure 4.7 indicate a possible source structure variability. In the first epoch, the source shows a compact structure and a possible second component was detected in the second epoch. The VLBI analysis suggests that the source may be considered as a calibrator. I suggest that the cautions should be taken when selecting the source. Multi-epoch contour maps in the RFC database (rfc_2019c) from 65 epochs between 1998 and 2017 show the total flux density changing between 1.831 Jy and 1.616 Jy. The range of the total flux density is 0.783 Jy. The contour maps of the source show source structure variability with a jet structure appearing and disappearing.

- **J1151-6728**

The source is an ICRF-3 reference source. I present the VLBI maps at S- and X-band from the CRDS-94 session. The S-band contour map is the first-ever contour map of the source. At S-band, the total flux density of 1.375 Jy is obtained. The SC was measured to be 0.74 with an SI of 1.30. The μ is 0.30, and was calculated from four epochs of available data. The S-band contour map in Figure 4.7 shows a compact structure that agrees with the SC and SI. The results from the astrometric quality assessments suggest that the source can be considered as a good calibrator. At X-band, a total flux density of 1.145 Jy is obtained. The SC and SI are 0.95 and 2.10 respectively. The μ is 0.29, and was calculated from four epochs of available data. The X-band map in Figure 4.7 shows an elongated structure of the source. However, no jet structure has been detected. The VLBI analysis suggests that the source can be considered as a good calibrator. The only image in the RFC database (rfc_2019c) is from the epoch in 2010. A total flux density of 0.788 Jy was obtained in the epoch. The contour map of the source shows a compact structure.

- **J1254-7138**

The source is an ICRF-3 defining source. I present the first-ever VLBI map at X-band from the CRDS-68 session where a total flux density of 0.948 Jy is obtained. The SC was measured to be 0.75 with an SI of 1.10. The μ is 0.29, and was calculated from 30 epochs of available data. The VLBI contour map is presented in Figure 4.7 where a point-like structure is seen. The results from astrometric quality assessment suggest that the source can be considered as a very good calibrator.

- **J1316-3338**

The source is a defining source in the ICRF-3 catalogue. I present the VLBI maps at S- and X-band from the CRDS-63 session. At S-band, a total flux density of 0.752 Jy is obtained. The SC was calculated to be 0.94 with an SI of 1.20. The μ is 0.62, and was calculated from 152 epochs of available data. The map in Figure 4.7 shows a compact structure that agrees with the SC and SI. The VLBI analysis suggests that the source can be considered as a very good calibrator. The contour maps in the RFC database (rfc_2019c) from 62 epochs between 1997 and 2017 show the total flux density changing between 1.511 Jy and 0.540 Jy. The range of the total flux density is 1.285 Jy from 62 epochs. The contour maps show a jet structure appearing and disappearing over the epochs. At X-band, I obtain a total flux density of 0.475 Jy. The SC was measured to be 0.79 with an SI of 2.30. The μ is 0.63, and was calculated from 152 epochs of available data. The VLBI contour map in Figure 4.7 shows a compact structure. The results from the VLBI analysis suggest that the source can be considered as a good calibrator. Multi-epoch contour maps in the RFC database (rfc_2019c) from 62 epochs between 1997 and 2017 show the total flux density changing between 1.423 Jy and 0.688 Jy. The range of the total flux density is 1.698 Jy from 62 epochs. Multi-epoch contour maps show source structure variability with a jet structure appearing and disappearing.

- **J1326-5256**

The source is an ICRF-3 reference source. I present the first-ever VLBI maps at S- and X-band from the CRDS-94 session. The total flux density is 1.151 Jy at S-band. The SC is 0.91 and the SI is 1.70. The μ is 0.31, and was calculated from six epochs of available data. The VLBI contour map in Figure 4.7 shows a compact structure that agrees with the SC and SI. The astrometric quality assessment results suggest that the source can be considered as a good calibrator. The total flux density is 1.145 Jy at X-band. The SC and SI are 0.95 and 2.10 respectively. The μ is 0.39, and was calculated from six epochs of available data. I present the VLBI contour map in Figure 4.7 where a compact structure is seen which agrees

with the SC and SI. The results from the astrometric quality assessment suggest that the source can be considered as a calibrator.

- **J1329-5608**

The source is an ICRF-3 defining source. I present the first-ever VLBI map at X-band from the CRDS-68 session. The total flux density is 0.765 Jy. The SC and SI are 0.86 and 1.23 respectively. The μ is 0.65, and was calculated from 33 epochs of available data. The VLBI contour map in Figure 4.7 shows a point-like structure that agrees with the SC and SI. The astrometric assessment results suggest that the source can be considered as a very good calibrator.

- **J1352-4412**

The source is an ICRF-3 reference source. I present the VLBI map at X-band from the CRDS-63 session where a total flux density of 0.415 Jy is obtained. The SC was measured to be 0.73 with an SI of 3.10. The μ is 0.38, and was calculated from 43 epochs of available data. The VLBI contour map is presented in Figure 4.7 where a jet-like structure can be seen that agrees with the SC and SI. The source should be used with caution when considered as a calibrator. It is recommended that the source be regularly monitored in the near future at all frequencies of interest. Multi-epoch X-band contour maps in the RFC database (rfc.2019c) from seven epochs between 2001 and 2017 show the total flux density changing between 0.320 Jy and 0.186 Jy. The range of the total flux density is 0.334 Jy. The contour maps show that source structure variability with a jet structure appearing and disappearing.

- **J1424-6807**

The source is an ICRF-3 defining source. I present the first-ever VLBI maps at S- and X-band. The S-band map is from the session CRDS-94 and X-band contour maps are from the sessions CRDS-66, -68 and -94 respectively. At S-band, a total flux density of 0.938 Jy is obtained. The SC was measured to be 1.00 with an SI of 1.35. The μ is 0.24, and was calculated from 30 epochs of available data. The map in Figure 4.7 shows a compact structure of the source that agrees with the SC and SI. The results from the astrometric quality assessment show that the source can be considered as a very good calibrator. At X-band, the total flux density is 1.168 Jy from the CRDS-66 map, 1.607 Jy from the CRDS-68 map and 1.821 Jy from the CRDS-94 map. The SC is 0.95, 0.59, and 0.80, respectively, and the SI is 1.20, 2.60, and 1.75, respectively. The μ is 0.28, and was calculated from 30 epochs of available data. The VLBI contour maps in Figure 4.7 show mostly a compact structure. However, the second epoch map (CRDS-68 session) shows a jet-like structure. The source should be used with caution when considered as a

calibrator. It is recommended that the source be regularly monitored in the near future at all frequencies of interest.

- **J1427-4206**

The source is an ICRF-3 defining source. The VLBI maps at S- and X-band are from the CRDS-63 session. At S-band, the total flux density is 1.609 Jy. The SC was measured to be 0.94 with an SI of 1.20. The μ is 0.53, and was calculated from 1451 epochs of available data. The map in Figure 4.7 shows a compact structure that agrees with the SC and SI. The results from the astrometric quality assessment suggest that the source can be considered as a very good calibrator. Multi-epoch contour maps in the RFC database (rfc_2019c) from 44 epochs between 1994 and 2017 show the total flux density changing between 0.052 Jy and 3.812 Jy. The total flux density range is 3.760 Jy from 44 epochs. Multi-epoch contour maps show a jet structure appearing and disappearing over the epoch of observations. The total flux density at X-band is 3.674 Jy. The SC was measured to be 0.89 with an SI of 2.70. The μ is 0.77, and was calculated from 1451 epochs of available data. The map in Figure 4.7 shows a jet-like structure that agrees with the SC and SI. The source should be used with caution when considered as a calibrator. It is recommended that the source be regularly monitored in the near future at all frequencies of interest. In the RFC database (rfc_2019c), the source has VLBI maps from 44 epochs between 1994 and 2017. The total flux density changes between 0.003 Jy and 3.566 Jy. The range of the total flux density is 5.671 Jy. The contour maps show source structure variability with jet structures appearing and disappearing.

- **J1452-6502**

The source is an ICRF-3 defining source. I present the VLBI map at X-band from the CRDS-68 session. A total flux density of 0.741 Jy is obtained. The SC and SI are 0.78 and 1.10 respectively. The μ is 0.58, and was calculated from 16 epochs of available data. The VLBI contour map in Figure 4.7 shows a compact structure of the source that agrees with the SC and SI. The results from the astrometric quality assessment suggest that the source can be considered as a very good calibrator source. The only map in the RFC database (rfc_2019c) at X-band from the epoch in 2010 shows a total flux density of 0.260 Jy. The contour map shows a compact structure of the source.

- **J1454-4012**

The source is an ICRF-3 defining source. The VLBI map at X-band and is from the CRDS-63 session. A total flux density of 0.341 Jy is obtained. The SC was measured to be 1.00 with an SI of 1.60. The μ is 0.52, and was calculated from 48

epochs of available data. The VLBI contour map in Figure 4.7 shows a compact structure that agrees with the SC and SI. The VLBI analysis suggests that the source can be considered as a very good calibrator source. Multi-epoch contour maps in the RFC database (rfc.2019c) from 28 epochs between 1999 and 2017 show the total flux density changing between 0.459 Jy and 0.451 Jy. The range of the total flux density is 0.198 from 28 epochs. The contour maps of the source show a compact structure of the source over most of the epochs.

- **J1514-4748**

The source J1514-4748 is an ICRF-3 defining source. I present the first-ever VLBI maps at S- and X-band from the CRDS-94 session. At S-band, the total flux density is 1.005 Jy. The SC was measured to be 0.99 with an SI of 1.25. The μ is 0.32, and was calculated from 11 epochs of available data. The S-band contour map in Figure 4.7 shows a compact structure that agrees with the SC and SI. The astrometric quality assessment results suggest that the source can be considered as a very good calibrator. I obtain a total flux density of 2.088 Jy at X-band. The SC was measured to be 1.02 with an SI of 1.60. The μ is 0.20, and was calculated from 11 epochs of available data. The VLBI contour map in Figure 4.7 shows a compact structure that agrees with the SC and SI. The results from astrometric quality assessment suggest that the source can be considered as a good calibrator.

- **J1558-6432**

The source is an ICRF-3 reference source. I present the VLBI map at X-band from the CRDS-68 session where a total flux density of 0.984 Jy is obtained. The SC was measured to be 0.65 with an SI 1.20. The μ is 0.45, and was calculated from 17 epochs of available data. The VLBI contour map of the source is presented in Figure 4.7 where a point-like structure is seen that agrees with the SC and SI. The VLBI analysis suggests that the source can be considered as a very good calibrator source. The only X-band map available in the RFC database (rfc.2019c) from the epoch in 2010 shows a total flux density of 0.340 Jy. The contour map in the database shows a compact structure of the source.

- **J1616-7108**

The source is an ICRF-3 reference source. I present the first-ever VLBI map at X-band from the CRDS-68 session. A total flux density of 0.924 Jy is obtained. The SC and SI are 0.61 and 2.80 respectively. The μ is 0.18, and was calculated from 18 epochs of available data. The contour map in Figure 4.7 shows a jet-like structure of the source that agrees with the SC and SI. The source should be used with caution when considered as a calibrator. It is recommended that the source be regularly monitored in the near future at all frequencies of interest.

- **J1624-6809**

The source is an ICRF-3 defining source. I present the first-ever VLBI maps at S-band from the CRDS-63 and -94 sessions. The VLBI maps at X-band are from the CRDS-63 and -94 sessions. At S-band, the total flux density is 1.183 Jy from the CRDS-63 map and 2.111 Jy from the CRDS-94 map. The SC are 0.89 and 0.76 respectively, and the SI are 1.30 and 1.78 respectively. The μ is 0.25, and was calculated from 36 epochs of available data. The contour maps in Figure 4.7 show structure variability. In the first epoch, the source shows a compact structure and in the second epoch, the source shows a jet structure. The results from the astrometric quality assessment suggest that the source may be considered as a calibrator source but cautions should be taken when selecting the source. At X-band, the total flux densities are 0.458 Jy and 1.411 Jy respectively. The SC are 0.86 and 0.90 respectively. The SI are 1.10 and 2.30 respectively. The μ is 0.31, and was calculated from 36 epochs of available data. The VLBI contour maps are presented in Figure 4.7 where a compact structure can be seen in both epochs. The astrometric analysis suggests that the source can be considered as a good calibrator. The only X-band contour map in the RFC database (rfc_2019c) is from 2010 when a total flux density of 1.292 Jy was obtained. The contour map shows a jet structure in the source.

- **J1628-6152**

The source is a defining source in the ICRF-3 catalogue. I present the first-ever VLBI map of the source at S-band from the session CRDS-94. The VLBI maps at X-band are from the CRDS-68 and -94 sessions. At S-band, the total flux density is 0.948 Jy. The SC was measured to be 0.91 with an SI of 1.34. The μ is 0.32, and was calculated from 29 epochs of available data. The contour map in Figure 4.7 shows a compact structure. The results from the astrometric quality assessment suggest that the source can be considered as a very good calibrator. At X-band, the total flux density is 1.226 Jy from the CRDS-68 map and 1.411 Jy from the CRDS-94 map. The SC are 0.74 and 0.90 respectively. The SI are 1.14 and 2.30 respectively. The μ is 0.28, and was calculated from 29 epochs of available data. The VLBI contour maps in Figure 4.7 show compact structure. The VLBI analysis suggests that the source can be considered as a good calibrator. The only X-band map in the RFC database (rfc_2019c) is from the epoch in 2010 when a total flux density of 0.947 Jy was obtained. The contour map shows a compact structure of the source.

- **J1650-5044**

The source J1650-5044 is an ICRF-3 reference source. I present the first-ever VLBI map at X-band from the CRDS-94 session. A total flux density of 3.663 Jy is obtained. The SC was measured to be 0.73 with an SI of 2.17. The μ is 0.24, and was calculated from five epochs of available data. The map in Figure 4.7 shows a compact structure. However, two possible components can be seen on the map. The source should be used with caution when considered as a calibrator. It is recommended that the source be regularly monitored in the near future at all frequencies of interest.

- **J1701-5621**

The source is a reference source in the ICRF-3 catalogue. I present the first-ever VLBI maps at S- and X-band. The S-band maps are from the CRDS-66 and -94 sessions and X-band maps are from the CRDS-68 and -94 sessions. At S-band, the total flux density is 0.725 Jy from the CRDS-66 map and 1.668 Jy from the CRDS-94 map. The SC are 0.34 and 0.68, respectively, and the SI are 3.35 and 2.20, respectively. The μ is 0.41, and was calculated from 37 epochs of available data. The VLBI contour maps in Figure 4.7 at both epochs show extended source structure. At the first epoch, the presence of a possible second component can be seen and at the second epoch, a jet structure is detected. The astrometric assessment suggests that the source may not a good calibrator. It is recommended that the source be regularly monitored in the near future at all frequencies of interest. At X-band, the total flux density is 1.279 Jy from the CRDS-68 map and 2.137 Jy from the CRDS-94 map. The SC are 0.49 and 1.23, respectively, and the SI are 0.62 and 2.70, respectively. The μ is 0.33, and was calculated from 37 epochs of available data. The VLBI contour maps are presented in Figure 4.7. At the first epoch, the source shows a compact structure and the source shows a possible second component in the second epoch. Based on the results, the source may be considered as a calibrator but cautions should be taken when selecting the source. It is recommended that the source be regularly monitored at all frequencies of interest.

- **J1703-6212**

The source J1703-6212 is an ICRF-3 reference source. I present the first-ever VLBI maps at S- and X-band. The S-band contour map is from the CRDS-94 session and X-band contour maps are from the CRDS-63 and -94 sessions. At S-band, a total flux density of 0.982 Jy is obtained. The SC was measured to be 0.91 with an SI of 1.67. The μ is 0.27, and was calculated from 32 epochs of available data. The VLBI contour map in Figure 4.7 shows a compact structure that agrees with

the SC and SI. The results from astrometric quality assessment suggest that the source can be considered as a good calibrator. At X-band, the total flux density is 0.485 Jy from the CRDS-63 map and 1.644 Jy from the CRDS-94 map. The SC are 0.77 and 1.02, respectively, and the SI are 1.20 and 2.18 respectively. The μ is 0.40, and was calculated from 32 epochs of available data. The contour maps in Figure 4.7 show compact structure in both epochs. The astrometric quality assessments suggest that the source can be considered as a calibrator.

- **J1733-7935**

The source is an ICRF-3 reference source. I present the first-ever VLBI map at X-band from the CRDS-68 session where a total flux density of 0.903 Jy is obtained. The SC and SI are 0.74 and 2.60 respectively. The μ is 0.37, and was calculated from 25 epochs of available data. The VLBI contour map is presented in Figure 4.7. The source shows a jet structure which also agrees with the results from the astrometric quality assessment. The source should be used with caution when considered as a calibrator. It is recommended that the source be regularly monitored in the near future at all frequencies of interest.

- **J1803-6507**

The source is an ICRF-3 reference source. I present the first-ever VLBI maps at S- and X-band from the CRDS-63 session. At S-band, the total flux density is 0.807 Jy. The SC and SI are 0.79 and 1.10 respectively. The μ is 0.21, and was calculated from 239 epochs of available data. The map in Figure 4.7 shows a compact structure that agrees with the SC and SI. The results from astrometric quality assessment suggest that the source can be considered as a very good calibrator. At X-band, I obtain a total flux density of 0.439 Jy. The SC was measured to be 0.96 with an SI of 2.10. The μ is 0.30, and was calculated from 239 epochs of available data. Figure 4.7 shows a compact source structure. The astrometric quality assessment suggests the source can be considered as a good calibrator.

- **J1809-4552**

The source is an ICRF-3 defining source. The VLBI maps at S- and X-band are from the CRDS-66 and -68 sessions respectively. At S-band, the total flux density is 0.484 Jy. The SC was measured to be 0.69 with an SI of 2.10. The μ is 0.37, and was calculated from 50 epochs of available data. The VLBI contour map in Figure 4.7 shows a compact structure. The astrometric quality assessments suggest that the source can be considered as a good calibrator. The contour maps in the RFC database (rfc.2019c) from three epochs between 2013 and 2017 show the total flux density changing between 0.388 Jy and 0.453 Jy. The total flux density has a range of 0.089 Jy from three epochs. The contour maps show a compact structure

of the source. At X-band, the total flux density is 0.820 Jy. The SC and SI are 0.77 and 1.30 respectively. The μ is 0.26, and was calculated from 50 epochs of available data. The map in Figure 4.7 shows a compact structure of the source that agrees with the SC and SI. The astrometric quality analysis suggests that the source is a very good calibrator. The VLBI contour maps in the RFC database (rfc.2019c) from five epochs between 2010 and 2017 show the total flux density changing between 0.767 Jy and 0.687 Jy. The total flux density range is 0.313 Jy. The contour maps at X-band show a compact structure of the source.

- **J1819-5521**

The source is a defining source in the ICRF-3 catalogue. I present the first-ever VLBI maps at S-band from the CRDS-63 and -94 sessions. The VLBI map at X-band is from the CRDS-63 session. At S-band, the total flux density is 0.841 Jy from the CRDS-63 map and 0.997 Jy from the CRDS-94 map. The SC were 0.71 and 0.92, respectively, and the SI are 1.15 and 1.45, respectively. The μ is 0.35, and was calculated from 283 epochs of available data. The VLBI contour maps in Figure 4.7 show a compact structure in both epochs. The astrometric analysis suggests that the source can be considered as a good calibrator. At X-band, I obtain a total flux density of 0.450 Jy. The SC was measured to be 0.74 with an SI of 1.75. The μ is 0.45, and was calculated from 283 epochs of available data. The VLBI contour map in Figure 4.7 shows a compact structure. Based on the results, the source can be considered as a good calibrator. The only X-band map in the RFC database (rfc.2019c) is from the epoch in 2010 when a total flux density of 0.970 Jy was obtained. The map of the source shows a compact structure of the source.

- **J1829-5813**

The source J1829-5813 is a reference source in the ICRF-3 catalogue. I present the first-ever VLBI maps of the source at S- and X-band. The S-band contour map is from the CRDS-66 session and the X-band contour map is from the CRDS-68 session. At S-band, a total flux density of 0.419 Jy is obtained. The SC and SI are 0.92 and 2.75 respectively. The μ is 0.33, and was calculated from 30 epochs of available data. The VLBI contour map in Figure 4.7 shows a jet structure. The source should be used with caution when considered as a calibrator. It is recommended that the source be regularly monitored in the near future at all frequencies of interest. At X-band, the total flux density is 0.859 Jy. The SC is 0.85 and the SI is 1.30. The μ is 0.51, and was calculated from 30 epochs of available data. Figure 4.7 shows a compact structure of the source. The astrometric quality assessment suggests the source can be considered as a very good calibrator source.

- **J1837-7108**

The source is an ICRF-3 defining source. I present the VLBI maps at S- and X-band from the CRDS-63 and -94 sessions. The S-band contour maps are the first-ever to present. At S-band, I obtain a total flux density of 0.839 Jy from the CRDS-63 map and 1.103 Jy from the CRDS-94 map. The SC are 0.84 and 1.12 respectively, and the SI are 0.85 and 1.20 respectively. The μ is 0.33, and was calculated from 33 epochs of available data. The VLBI contour maps at both epochs (Figure 4.7) show a compact source structure. The astrometric analysis shows that the source can be used as a very good calibrator. At X-band, the total flux density is 0.355 Jy from the CRDS-63 map and 2.300 Jy from the CRDS-94 map. The SC are 0.93 and 1.02 respectively, and the SI are 1.60 and 2.16 respectively. The μ is 0.51, and was calculated from 33 epochs of available data. The contour maps presented in Figure 4.7 show a compact structure. The VLBI analysis suggests that the source can be considered as a good calibrator. The only X-band contour map available in the RFC database (rfc_2019c) is from the epoch in 2010 when a total flux density of 1.601 Jy was obtained. The map shows an extended emission in the source.

- **J1857-5325**

The source is an ICRF-3 reference source. I present the first-ever VLBI map of the source at S-band from the CRDS-94 session. A total flux density of 0.883 Jy is obtained. The SC was measured to be 1.03 with an SI of 1.29. The μ is 0.17, and was calculated from 8 epochs of available data. The VLBI contour map in Figure 4.7 shows a compact structure that also agrees with the results from the astrometric analysis. It suggests that the source can be considered as a very good calibrator. The X-band imaging and structure analysis are recommended using CRDS sessions in the near future.

- **J1930-6056**

The source is an ICRF-3 defining source. I present the first-ever VLBI maps at S-band from the CRDS-66 and -94 sessions. The X-band map is from the CRDS-68 session. At S-band, the total flux density is 0.684 Jy from the CRDS-66 map and 1.119 Jy from the CRDS-94 map. The SC are 0.66 and 0.93, respectively, and the SI are 1.45 and 1.34 respectively. The μ is 0.24, and was calculated from 36 epochs of available data. The map in Figure 4.7 shows a compact structure of the source in both of the epochs. The astrometric quality assessments suggest that the source can be used as a good calibrator. At X-band, a total flux density of 1.113 Jy is obtained. The SC is 0.56 and the SI is 3.10. The μ is 0.22, and was calculated from 36 epochs of available data. The map in Figure 4.7 shows an extended structure

of the source with a possible second component. The source should be used with caution when considered as a calibrator. It is recommended that the source be regularly monitored in the near future at all frequencies of interest. The only X-band map in the RFC database (rfc_2019c) is from the epoch in 2010 when a total flux density of 0.914 Jy was obtained. The contour map shows a compact structure of the source.

- **J1933-6942**

The source is an ICRF-3 reference source. I present the first-ever VLBI map at S-band from the CRDS-94 session where a total flux density of 0.975 Jy is obtained. The SC was measured to be 0.98 with an SI of 2.23. As there is no flux density available on the GSFC server, the μ was not calculated. The VLBI contour map in Figure 4.7 shows a compact structure of the source. The astrometric quality assessment suggests that the source can be considered as a good calibrator.

- **J1937-3958**

The source is an ICRF-3 reference source. I present the VLBI maps at S- and X-band from the CRDS-63 session. At S-band, a total flux density of 0.780 Jy is obtained. The SC was measured to be 0.89 with an SI of 1.23. The μ is 0.27, and was calculated from 75 epochs of available data. The VLBI contour map in Figure 4.7 shows a compact structure. The results from astrometric quality assessment suggest that the source can be considered as a very good calibrator. Multi-epoch contour maps in the RFC database (rfc_2019c) from 11 epochs between 2001 and 2017 show the total flux density changing between 0.812 Jy and 1.166 Jy. The total flux density range is 0.626 Jy from 11 epochs. The contour maps show a jet structure appearing and disappearing. At X-band, a total flux density of 0.816 Jy is obtained. The SC was measured to be 0.88 with an SI of 3.02. The μ is 0.29, and was calculated from 75 epochs of available data. The map in Figure 4.7 shows a jet structure in the source. The source should be used with caution when considered as a calibrator. It is recommended that the source be regularly monitored in the near future at all frequencies of interest. The VLBI contour maps in the RFC database (rfc_2019c) from 11 epochs between 2001 and 2017 show the total flux density changing between 0.419 Jy and 1.090 Jy. The range of total flux density is 1.110 Jy. The contour maps show source structure variability with the appearance and disappearance of a jet structure.

- **J1940-6907**

The source J19140-6907 is an ICRF-3 defining source. I present the first-ever VLBI map at S-band from the CRDS-66 session. The X-band contour map is presented from the session CRDS-68. At S-band, the total flux density of 0.699

Jy is obtained. The SC and SI are 0.59 and 2.20 respectively. The μ is 0.22, and was calculated from 30 epochs of available data. The VLBI contour map of the source in Figure 4.7 shows a compact structure with a possible second component. The results from astrometric quality assessment suggest that the source can be used as a good calibrator. At X-band, the total flux density is 0.980 Jy. The SC was measured to be 0.59 with an SI of 2.70. The μ is 0.27, and was calculated from 30 epochs of available data. The VLBI contour map in Figure 4.7 shows a jet structure. The source should be used with caution when considered as a calibrator. It is recommended that the source be regularly monitored in the near future at all frequencies of interest. The only X-band contour map in the RFC database (rfc_2019c) is from 2010 when a total flux density of 0.776 Jy was obtained. The contour map shows a jet structure in the source.

- **J1941-6211**

The source is an ICRF-3 reference source. I present the first-ever VLBI map at S-band from the CRDS-94 session where a total flux density of 1.120 Jy is obtained. The SC and SI are 0.85 and 2.10 respectively. The μ is 0.27, and was calculated from seven epochs of available data. The VLBI contour map in Figure 4.7 shows a compact structure. A possible second component is also detected which can only be confirmed from more imaging in the near future. The results from the astrometric analysis suggest that the source can be considered as a good calibrator.

- **J1955-6115**

The source is an ICRF-3 reference source. I present the first-ever VLBI map at S-band from the CRDS-94 session. A total flux density of 1.039 Jy is obtained. The SC and SI are 0.91 and 1.65 respectively. The μ is 0.14, and was calculated from four epochs of available data. The map in Figure 4.7 shows a compact structure of the source. The results from the astrometric analysis suggest that the source can be used as a good calibrator.

- **J1957-3845**

The source J1957-3845 is an ICRF-3 defining source. I present the VLBI maps at S- and X-band from the CRDS-63 session. At S-band, the total flux density is 1.182 Jy. The SC is 0.84 and the SI is 1.17. The μ is 0.39, and was calculated from 1070 epochs of available data. The VLBI contour map in Figure 4.7 shows a compact structure of the source. The results from astrometric quality assessments suggest that the source can be considered as a good calibrator. Multi-epoch contour maps in the RFC database (rfc_2019c) from 43 epochs between 1998 and 2017 show the total flux density changing between 2.503 Jy and 1.003 Jy. The total flux density has a range of 1.975 Jy. The S-band contour maps show source structure variability

with a jet structure appearing and disappearing. At X-band, the total flux density is 0.768 Jy. The SC and SI are 0.71 and 2.65 respectively. The μ is 0.42, and was calculated from 1070 epochs of available data. The VLBI contour map in Figure 4.7 shows a jet structure in the source. The source should be used with caution when considered as a calibrator. It is recommended that the source be regularly monitored in the near future at all frequencies of interest. Multi-epoch contour maps in the RFC database (rfc.2019c) from 43 epochs between 1998 and 2017 show the total flux density changing between 2.499 Jy and 0.917 Jy. The range of total flux density is 2.966 Jy from 43 epochs. The contour maps show source structure variability in some epochs with a jet structure.

- **J2005-3723**

The source is an ICRF-3 defining source. I present the VLBI maps at S- and X-band from the CRDS-66 and -68 sessions respectively. At S-band, the total flux density is 0.454 Jy. The SC and SI are 1.07 and 1.20 respectively. The μ is 0.23, and was calculated from 42 epochs of available data. The VLBI contour map in Figure 4.7 shows a compact structure. The astrometric quality assessment results suggest that the source can be considered as a very good calibrator. Multi-epoch VLBI contour maps in the RFC database (rfc.2019c) from 19 epochs between 2002 and 2017 show the total flux density changing between 0.244 Jy and 0.478 Jy. The range of total flux density is 0.249 Jy from 19 epochs. The contour maps show source structure variability in the source with a jet structure appearing and disappearing. At X-band, the total flux density is 0.874 Jy. The SC and SI are 0.72 and 2.10 respectively. The μ is 0.24, and was calculated from 42 epochs of available data. The VLBI contour map in Figure 4.7 shows a compact structure of the source. The results from astrometric quality assessment suggest that the source can be considered as a good calibrator. The contour maps in the RFC database (rfc.2019c) from 19 epochs between 2002 and 2017 show the total flux density changing between 0.412 Jy and 0.633 Jy. The total flux density has a range of 0.221 Jy from 19 epochs. The contour maps of the source show a jet structure appearing and disappearing.

- **J2035-6846**

The source is an ICRF-3 reference source. I present the VLBI maps at S- and X-band from the CRDS-94 session. The S-band contour map is the first-ever VLBI map. At S-band, a total flux density of 0.881 Jy is obtained. The SC and SI are 1.04 and 1.67 respectively. The μ is 0.37, and was calculated from seven epochs of available data. The VLBI contour map in Figure 4.7 shows a compact structure of the source. The results from astrometric quality assessments show that the

source can be considered as a good calibrator. At X-band, the total flux density is 1.650 Jy. The SC and SI are 0.75 and 2.80 respectively. The μ is 0.28, and was calculated from seven epochs of available data. The VLBI contour map in Figure 4.7 shows a jet structure. The source should be used with caution when considered as a calibrator. It is recommended that the source be regularly monitored at all frequencies of interest. The only contour map in the RFC database (rfc_2019c) is from 2010 when a total flux density of 0.605 Jy was obtained. The X-band contour map shows a compact structure of the source.

- **J2056-4714**

The source is an ICRF-3 defining source. I present the VLBI maps at S- and X-band from the CRDS-63 session. At S-band, a total flux density of 1.388 Jy is obtained. The SC was measured to be 0.93 with an SI of 1.25. The μ is 0.36, and was calculated from 1059 epochs of available data. The VLBI contour map in Figure 4.7 shows a compact source structure. The results from the astrometric quality assessment show that the source can be considered as a very good calibrator. Multi-epoch contour maps in the RFC database (rfc_2019c) from 27 epochs between 1999 and 2017 show the total flux density changing between 1.673 Jy and 1.896 Jy. The range of the total flux density is 0.748 Jy. The contour maps from the epochs show a jet structure appearance and disappearance in the source. At X-band, the total flux density is 1.139 Jy. The SC is 0.73 and the SI is 2.10. The μ is 0.70, and was calculated from 1059 epochs of available data. The VLBI contour map in Figure 4.7 shows a compact structure. The results from astrometric quality assessment suggest that the source can be considered as a good calibrator. The VLBI contour maps in the RFC database (rfc_2019c) from 28 epochs between 1999 and 2017 show the total flux density changing between 1.382 Jy and 1.887 Jy. The total flux density range is 1.172 Jy from 28 epochs. The contour maps from the 28 epochs show source structure variability in the source.

- **J2109-4110**

The source is an ICRF-3 reference source. The VLBI maps at S- and X-band are from the CRDS-66 and 68 sessions respectively. At S-band, a total flux density of 0.032 Jy is obtained. The SC was measured to be 0.68 with an SI of 1.10. The μ is 0.57, and was calculated from 42 epochs of available data. The VLBI contour map in Figure 4.7 shows a compact source structure. The results from astrometric quality assessments suggest that the source can be considered as a very good calibrator. Multi-epoch contour maps in the RFC database (rfc_2019c) from 17 epochs between 2002 and 2017 show the total flux density changing between 0.849 Jy and 0.868 Jy. The total flux density range is 1.587 Jy. The contour maps

show a compact structure of the source in most of the epochs. At X-band, the total flux density is 0.874 Jy. The SC and SI are 0.72 and 2.10 respectively. The μ is 0.83, and was calculated from 42 epochs of available data. The VLBI contour map in Figure 4.7 shows a compact structure of the source. The astrometric quality assessment results suggest that the source can be used as a good calibrator. The contour maps in the RFC database (rfc_2019c) from 17 epochs between 2002 and 2017 show the total flux density changing between 1.399 Jy and 0.495 Jy. The total flux density has a range of 1.209 Jy. The maps show the appearance and disappearance of a jet structure in the source.

- **J2126-4605**

The source J2126-4605 is a reference source in the ICRF-3 catalogue. I present the VLBI maps at S- and X-band from the CRDS-94 and -63 sessions respectively. The S-band contour map is the first-ever to present. At S-band, a total flux density of 0.784 Jy is obtained. The SC and SI are 1.06 and 1.70 respectively. The μ is 0.37, and was calculated from 32 epochs of available data. The VLBI contour map in Figure 4.7 shows a compact source structure that agrees with the SC and SI. The results from the astrometric quality assessment suggest the source can be considered as a good calibrator. The only S-band contour map in the RFC database (rfc_2019c) is from 2011 when a total flux density of 0.550 Jy was obtained. The source map shows an extended emission in the source. At X-band, the total flux density of 0.270 Jy is obtained. The SC was measured to be 1.13 with an SI of 1.30. The μ is 0.37, and was calculated from 32 epochs of available data. The VLBI contour map in Figure 4.7 shows a point-like structure. The results from the astrometric quality assessment suggest that the source can be considered as a very good calibrator. The VLBI map in the RFC database (rfc_2019c) is at X-band and is from 2011 when a total flux density of 0.442 Jy was obtained. The contour map shows a compact structure of the source.

- **J2147-7536**

The source is an ICRF-3 defining source. I present the first-ever VLBI map at S-band from the CRDS-66 session. The VLBI maps at X-band are from the CRDS-66 and -68 sessions respectively. At S-band, a total flux density of 2.164 Jy is obtained. The SC was measured to be 0.28 with an SI of 3.20. The μ is 0.25, and was calculated from 79 epochs of available data. The VLBI contour map in Figure 4.7 shows a jet structure that agrees with the SC and SI. The source should be used with caution when considered as a calibrator. It is recommended that the source be regularly monitored in the near future at all frequencies of interest. At X-band, I obtain a total flux density of 3.549 Jy from the CRDS-66 map and 2.076

Jy from the CRDS-68 map. The SC are 0.63 and 0.91 respectively, and the SI are 2.52 and 1.10 respectively. The μ is 0.28, and was calculated from 79 epochs of available data. The map in Figure 4.7 shows a jet structure in the first epoch and a point-like structure in the second epoch. The results from astrometric quality assessment suggest that the source can be considered as a calibrator. The only X-band map available in the RFC database (rfc_2019c) is from the epoch in 2010 when a total flux density of 1.062 Jy was obtained. The map shows a jet structure in the source.

- **J2207-5346**

The source is a reference source in the ICRF-3 catalogue. I present the first-ever VLBI maps at S-band are from the CRDS-63 and -94 sessions respectively. The VLBI maps at X-band are also from the CRDS-63 and -94 sessions respectively. At S-band, I obtain a total flux density of 0.922 Jy from the CRDS-63 map and 1.266 Jy from the CRDS-94 map. The SC are 0.82 and 0.88 respectively, and the SI are 1.15 and 2.10 respectively. The μ is 0.29, and was calculated from 48 epochs of available data. At both epochs, the VLBI contour maps in Figure 4.7 show a point-like structure. The results from the astrometric quality assessment suggest that the source can be considered as a good calibrator. At X-band, the total flux density is 0.740 Jy from the CRDS-63 map and 1.374 Jy from the CRDS-94 map. The SC is 0.73 and 2.65 respectively, and the SI is 0.93 and 3.10 respectively. The μ is 0.36, and was calculated from 48 epochs of available data. The VLBI contour maps in Figure 4.7 from both epoch show a jet structure. The source should be used with caution when considered as a calibrator. It is recommended that the source be regularly monitored in the near future at all frequencies of interest. The only VLBI map in the RFC database (rfc_2019c) is at X-band and is from 2010 when a total flux density of 0.891 Jy was obtained. The contour map shows an extended emission in the source.

- **J2223-3455**

The source is an ICRF-3 defining source. I present the VLBI maps at S- and X-band from the CRDS-94 and -68 sessions respectively. At S-band, the total flux density is 0.905 Jy. The SC was measured to be 0.99 with an SI of 2.30. The μ is 0.39, and was calculated from 42 epochs of available data. The VLBI contour map in Figure 4.7 shows a compact structure. The results from the astrometric quality assessment suggest that the source can be considered as a good calibrator. Multi-epoch contour maps in the RFC database (rfc_2019c) from 19 epochs between 2005 and 2017 show the total flux density changing between 0.337 Jy and 0.340 Jy. The total flux density has a range of 0.129 Jy. The contour maps show a compact

structure of the source in the majority of the epochs. At X-band, I obtain a total flux density of 0.794 Jy. The SC was measured to be 0.77 with an SI of 1.20. The μ is 0.39, and was calculated from 42 epochs of available data. The map in Figure 4.7 shows that the source has a compact structure. The astrometric quality assessments suggest that the source can be considered as a very good calibrator. Multi-epoch contour maps in the RFC database (rfc_2019c) from 21 epochs between 2005 and 2017 show the total flux density changing between 0.302 Jy and 0.289 Jy. The range of the total flux density is 0.112 Jy. The contour maps show a compact structure at the majority of the epochs.

- **J2235-4835**

The source is a defining source in the ICRF-3 catalogue. I present the VLBI map at S- and X-band from the CRDS-63 session. At S-band, a total flux density of 0.938 Jy is obtained. The SC was measured to be 1.00 with an SI of 1.27. The μ is 0.21, and was calculated from 149 epochs of available data. The VLBI contour map in Figure 4.7 shows a compact structure of the source. The result from the astrometric quality assessment show that the source can be considered as a good calibrator. The contour maps in the RFC database (rfc_2019c) are from 2007 and 2017. The range of total flux density is 0.093 Jy from the two epochs. The contour maps from the two epochs show a compact structure of the source. At X-band, the total flux density is 0.444 Jy. The SC was measured to be 1.11 with an SI of 1.75. The μ is 0.28, and was calculated from 149 epochs of available data. The VLBI contour map in Figure 4.7 shows a compact structure in the source. The results from the astrometric analysis suggest that the source can be considered as a good calibrator. Multi-epoch contour maps in the RFC database (rfc_2019c) from five epochs between 2007 and 2017 show the total flux density changing between 1.240 Jy and 0.814 Jy. The total flux density has a range of 0.694 Jy from five epochs. The source shows a compact structure over all the epochs.

- **J2239-5701**

Source J2239-5701 is an ICRF-3 defining source. I present the first-ever VLBI maps at S-band from the CRDS-66 and -94 sessions respectively. The VLBI maps at X-band are from the CRDS-66, -68 and -94 sessions respectively. At S-band, I obtain a total flux density of 0.510 Jy from the CRDS-66 map and 0.916 Jy from the CRDS-94 map. The calculated SC are 0.75 and 1.03 respectively, and the SI are 1.10 and 1.23 respectively. The μ is 0.42, and was calculated from 37 epochs of available data. The VLBI contour maps in Figure 4.7 show that the source has a compact structure. The astrometry analysis suggests that the source can be considered as a good calibrator. At X-band, the total flux density is 1.174 Jy

from the CRDS-66 map, 1.389 Jy from the CRDS-68 map and 1.322 Jy from the CRDS-94 map. The SC is 1.01, 0.80 and 1.06, respectively, and the SI is 1.20, 1.10 and 1.75 respectively. The μ is 0.21, and was calculated from 37 epochs of available data. The VLBI contour maps in Figure 4.7 show that the source has a compact structure at all the epochs. The results from the astrometric analysis suggest that the source can be considered as a good calibrator. The only VLBI contour map in the RFC database (rfc_2019c) is from the epoch in 2010 when a total flux density of 1.065 Jy was obtained. The contour map shows a compact structure of the source.

- **J2247-3657**

The source is an ICRF-3 defining source. I present the VLBI map at X-band from the CRDS-63 session. A total flux density of 0.379 Jy is obtained. The SC was measured to be 0.92 with an SI of 1.23. The μ is 0.33, and was calculated from 53 epochs of available data. The map in Figure 4.7 shows that the source is compact in nature. The astrometric quality assessment results suggest that the source can be considered as a good calibrator. Multi-epoch contour maps in the RFC database (rfc_2019c) from 15 epochs between 2005 and 2017 show the total flux density changing between 0.631 Jy and 0.790 Jy. The total flux density range is 0.401 Jy from 15 epochs. The contour maps show the appearance and disappearance of a jet structure in the source.

- **J2248-3235**

The source is an ICRF-3 defining source. I present the VLBI map at S-band from the CRDS-66 session. The VLBI maps at X-band are from the CRDS-66 and -68 sessions respectively. At S-band, the total flux density is 0.506 Jy. The SC and SI are 1.06 and 1.25 respectively. The μ is 0.28, and was calculated from 33 epochs of available data. The VLBI contour map in Figure 4.7 shows a compact structure. The result from astrometric quality assessments suggests that the source is a very good calibrator. Multi-epoch contour maps in the RFC database (rfc_2019c) from 15 epochs between 2000 and 2017 show the total flux density changing between 0.441 Jy and 0.470 Jy. The range of total flux density is 0.381 Jy from 15 epochs. The contour maps from the epochs show the appearance and disappearance of a jet structure in the source. At X-band, the total flux density is 0.864 Jy from the CRDS-66 map and 1.023 Jy from the CRDS-68 map. The calculated SC are 1.01 and 0.86 respectively, and the SI is 1.34 at both epochs. The μ is 0.37, and was calculated from 33 epochs of available data. The VLBI contour maps in Figure 4.7 show a compact structure of the source. The results from astrometric quality assessments suggest that the source can be considered as a good calibrator. The

VLBI contour maps in the RFC database (rfc_2019c) from 15 epochs between 2000 and 2017 show the total flux density changing between 0.308 Jy and 0.572 Jy. The range of the total flux density is 0.389 Jy. The contour maps of the source show source structure variability with the appearance and disappearance of a jet structure.

- **J2303-6807**

The source is a reference source in the ICRF-3 catalogue. I present the first-ever VLBI map at S-band from the CRDS-63 session. At S-band, a total flux density of 0.814 Jy is obtained. The SC and SI are 0.78 and 1.14 respectively. The μ is 0.25, and was calculated from 287 epochs of available data. The map in Figure 4.7 shows a point-like structure of the source. The astrometric quality assessment results suggest that the source can be considered as a very good calibrator.

- **J2329-4730**

The source is a reference source in the ICRF-3 catalogue. I present S-band contour map from the CRDS-66 session and X-band contour map from the CRDS-68 session. The total flux density at S-band is 2.062 Jy. The SC was measured to be 0.29 with an SI of 3.75. The μ is 0.25, and was calculated from 67 epochs of available data. The VLBI map in Figure 4.7 shows an extended structure of the source. The structure analysis suggests that the source may not be good calibrator at S-band. Multi-epoch contour maps in the RFC database (rfc_2019c) from three epochs between 2010 and 2017 show the total flux density changing between 1.771 Jy and 1.648 Jy. The range of total flux density is 0.365 Jy from the three epochs. The maps show a jet structure in the source. At X-band, the total flux density is 1.693 Jy. The SC and SI are 0.57 and 1.15 respectively. The μ is 0.26, and was calculated from 67 epochs of available data. The X-band image in Figure 4.7 shows a compact structure of the source. The astrometric quality assessment results suggest that the source can be considered as a very good calibrator. Multi-epoch contour maps in the RFC database (rfc_2019c) from three epochs between 2010 and 2017 show the total flux density changing between 1.657 Jy and 1.078 Jy. The range of total flux density is 0.579 Jy from three epochs. The appearance and disappearance of a jet structure have been detected in all the epochs.

- **J2336-4115**

The source is a reference source in the ICRF-3 catalogue. I present the VLBI maps at X-band from the CRDS-63 and -94 sessions respectively. The total flux density is 0.023 Jy from the CRDS-63 map and 1.195 Jy from the CRDS-94 map. The SC are 0.47 and 1.03 respectively, and the SI are 1.40 and 1.60 respectively. The μ is 0.36, and was calculated from 37 epochs of available data. The VLBI map in

Figure 4.7 shows a compact structure with an elongated beam. The astrometric analysis suggests that the source can be used as a good calibrator. Multi-epoch VLBI contour maps in the RFC database (rfc.2019c) from 11 epochs between 2012 and 2017 show the total flux density changing between 0.610 Jy and 0.536 Jy. The total flux density range is 0.213 Jy. The contour maps show source structure variability with the appearance and disappearance of a jet structure.

- **J2336-5236**

The source is an ICRF-3 reference source. I present the first-ever VLBI map at S-band from the CRDS-94 session. A total flux density of 1.442 Jy is obtained. The SC was measured to be 0.81 with an SI of 2.33. The μ is 0.09, and was calculated from five epochs. The VLBI map in Figure 4.7 shows that the source has a jet-like structure. The source should be used with caution when considered as a calibrator. It is recommended that the source be regularly monitored in the near future at all frequencies of interest.

- **J2347-5110**

The source is an ICRF-3 reference source. I present the first-ever VLBI map at S-band from the CRDS-94 session. The map at X-band is from the CRDS-68 session. At S-band, the total flux density is 1.017 Jy. The SC and SI are 0.85 and 2.60 respectively. The μ is 0.26, and was calculated from 26 epochs of available data. The VLBI contour map in Figure 4.7 shows an extended emission in the source. The source should be used with caution when considered as a calibrator. The X-band total flux density is 0.847 Jy. The SC and SI are 0.66 and 1.25 respectively. The μ is 0.33, and was calculated from 26 epochs of available data. The map at X-band in Figure 4.7 shows a compact structure of the source. The astrometric analysis suggests that the source can be considered as a good calibrator source. The only available map of the source in the RFC database (rfc.2019c) is from the epoch in 2010 when a total flux density of 0.347 Jy was obtained. The contour map of the source shows a compact structure.

- **J2356-6820**

The source J2356-6820 is an ICRF-3 defining source. I present the VLBI map at X-band from the CRDS-68 session. The total flux density obtained is 0.623 Jy. The SC and SI are 0.69 and 1.20 respectively. The μ is 0.29, and was calculated from 56 epochs. The VLBI contour map in Figure 4.7 shows a point-like structure. The results from the astrometric analysis suggest that the source can be considered as a very good calibrator. The only map of the source in the RFC database (rfc.2019c) is from the epoch in 2010 when a total flux density of 1.022 Jy was obtained. The contour map at X-band shows a jet-like structure in the source.

- **J2357-5311**

The source is an ICRF-3 defining source. I present the first-ever VLBI map at S-band from the CRDS-94 session. The first-ever VLBI maps at X-band are from the CRDS-68 and -94 sessions respectively. At S-band, the total flux density is 1.137 Jy. The SC was measured to be 1.03 with an SI of 1.80. The μ is 0.19, and was calculated from 95 epochs of available data. The VLBI contour map in Figure 4.7 shows a jet-like structure in the source. The results from the astrometric analysis suggest that the source can be considered as a good calibrator. At X-band, I obtain a total flux density of 2.064 Jy from the CRDS-68 map and 2.380 Jy from the CRDS-94 map. The calculated SC are 0.59 and 0.93 respectively, and the SI are 2.10 and 2.20 respectively. The μ is 0.24, and was calculated from 95 epochs of available data. The VLBI contour maps at both epochs (Figure 4.7) show a compact structure of the source. The astrometric quality assessment results suggest that the source can be considered as a good calibrator.

- **J2359-3133**

The source J2359-3133 is a reference source in the ICRF-3 catalogue. I present the VLBI maps at S- and X-band from the CRDS-63 session. At S-band, the total flux density is 0.612 Jy. The SC was measured to be 0.93 with an SI of 1.45. The μ is 1.00, and was calculated from 209 epochs of available data. The VLBI contour map in Figure 4.7 shows a compact structure. The results from the astrometric quality assessment suggest that the source can be considered as a good calibrator. Multi-epoch contour maps in the RFC database (rfc_2019c) from 30 epochs between 2002 and 2017 show the total flux density changing between 0.561 Jy and 0.581 Jy. The range of the total flux density from 30 epochs is 0.338 Jy. The contour maps at multi-epoch show the appearance and disappearance of a jet structure in the source. At X-band, the total flux density is 0.275 Jy. The SC was measured to be 1.04 with an SI of 1.45. The μ is 0.36, and was calculated from 209 epochs of available data. The map in Figure 4.7 shows that the source has a compact structure. The results from astrometric quality assessment suggest that the source can be considered as a good calibrator. Multi-epoch contour maps in the RFC database (rfc_2019c) from 36 epochs between 2002 and 2017 show the total flux density changing between 0.775 Jy and 0.461 Jy. The range of the total flux density is 0.409 Jy. The contour maps show a compact structure of the source over the majority of the epochs.

Chapter 5

Conclusion

In this work, I present a framework for studying the source structure in ICRF sources below a declination of -30° . I have used the CRDS S- and X-band observations from four sessions (three in 2013 and one in 2018) in which a total of 103 sources was observed. Among all IVS geodetic and astrometric observations, this work presents the first routine imaging campaign of ICRF sources in the Southern Hemisphere. In addition to the imaging, I calculated the following metrics from the CRDS data analysed in this work: SC, SI, R_w and $R_{95\%}$. The SC is the ratio of the sum of flux densities of CLEAN components within one synthesized beam to the total CLEAN flux density. The second metric which I calculated is the SI, which is widely used to analyse the astrometric quality of a source. A source with extended structure introduces additional components in the VLBI phase and delay observables, and therefore will have a higher SI. The last metric which was calculated is the radial extent. I calculated two types of radial extent: R_w , which quantifies the core dominance in a source, and $R_{95\%}$, which indicates how extended a source is. Finally, the μ was calculated for all the sources, using correlated flux densities from the GSFC server, for all IVS sessions in the time range from 2000 to 2017. The μ gives information about the overall source behaviour.

In order to verify the reliability of the images produced in this study, the X-band contour maps created from the CRDS sessions were compared to available X-band maps from the RFC database (rfc_2019c). It should be noted that the map scales between the CRDS maps and the maps from the RFC database differ by a factor of 5. Only three of the sources from the CRDS sessions analysed in this study had existing images at an epoch which is close to one of the epochs in the RFC database. The three sources are J0538-4405, J0922-3959 and J1147-3812, which have been imaged at 48, 72 and 65 epochs, respectively. For the assessment, roughly contemporaneous images were selected, and the SC and SI were calculated.

For the source J0538-4405, I have selected the RFC epoch 2013.09.11 as a roughly contemporaneous epoch to the CRDS-68 session on 2013.11.27. The SC measured from the image in the RFC database is 0.69 and from the CRDS session, an SC of 0.71 was measured. Similarly, the SI was measured to be 1.20 for the image in the RFC database and I calculated an SI of 1.10 from the CRDS image. It should be noted that the source was also imaged in 2012 (prior to the 2013 epoch), at which time a flux density of $4.230 \text{ Jy beam}^{-1}$ was measured. The time difference between the two epochs (shown in Figure 5.1), is ~ 2 months and both maps show a compact morphology with very little structure. It should be noted the image noise in the CRDS image is almost a factor of 50 higher than the RFC image.

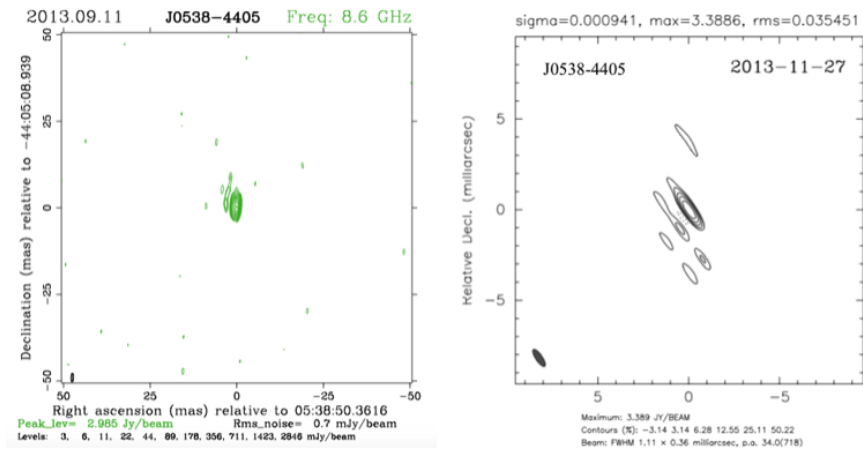


FIGURE 5.1: The contour maps from the RFC database (left panel) and the CRDS-68 session (right panel). The image RMS in the right panel is in units of Jy beam^{-1} . Two epochs are separated by ~ 2 months. The observations from the CRDS session, having a higher resolution, detect a jet structure in the source towards the north-east direction of the core. Image credit (left panel): Leonid Petrov, RFC database.

Similarly, for the source J0922-3959, I have selected the epoch 2013.07.24 as a roughly contemporaneous epoch to the CRDS-66 session on 2013.07.30. The SC calculated using the image from the RFC database and the CRDS-68 session are both 0.76. The SI calculated using the RFC database image is 1.37 and I obtained an SI of 1.40 from the CRDS-68 image of the source. Contour maps from the two epochs are presented in Figure 5.2. The peak flux density obtained from the RFC database is $0.841 \text{ Jy beam}^{-1}$ and I obtained a peak flux density of $0.863 \text{ Jy beam}^{-1}$. Both of the contour plots indicate a similar compact source structure, with a slight extension in a south-westerly direction. It should be noted the image noise in the CRDS image is almost a factor of 13 higher than the RFC image.

For the source J1147-3812, I selected the CRDS-68 session on 2013.07.30 as roughly contemporaneous to the contour map from the epoch 2013.07.24 in the RFC database. Figure 5.3 shows contour plots from both epochs. A peak flux density of $1.602 \text{ Jy beam}^{-1}$

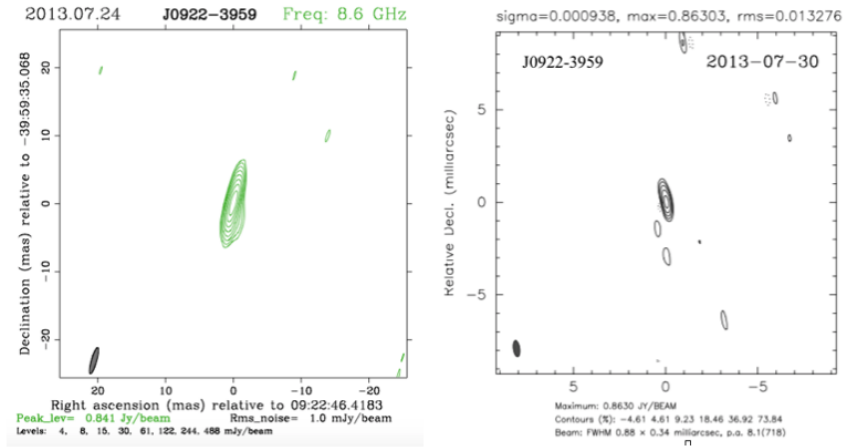


FIGURE 5.2: The contour maps from the RFC database (left panel) and the CRDS-66 session (right panel). The RMS in the right panel is in units of Jy beam^{-1} . Two epochs are separated by 6 days. Both contour maps show a similar source structure. Image credit (left panel): Leonid Petrov, RFC database.

was obtained from the RFC database image and I obtained a peak flux density of $2.270 \text{ Jy beam}^{-1}$ from the CRDS-66 image. An SC of 0.86 was measured from the RFC

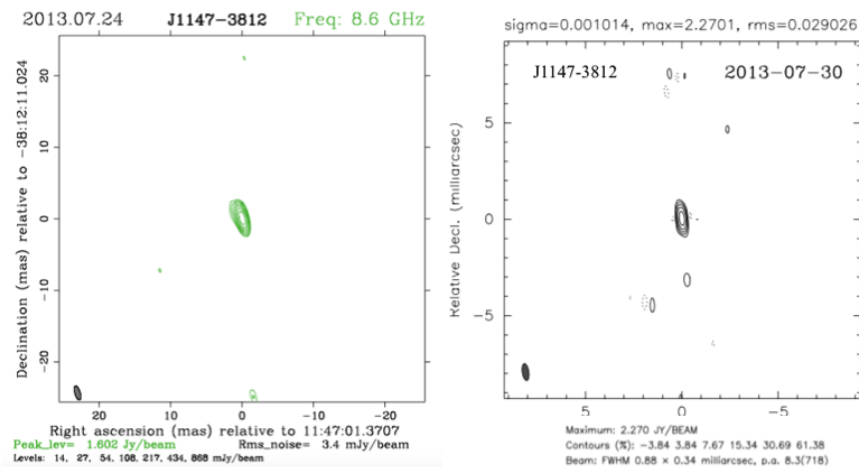


FIGURE 5.3: The contour maps from the RFC database (left panel) and the CRDS-66 session (right panel). The RMS in the right panel is in units of Jy beam^{-1} . Two epochs are separated by 6 days. Both contour maps show a similar source structure. Image credit (left panel): Leonid Petrov, RFC database.

database image and a value of 0.91 from the CRDS-66 image. The SI was measured to be 2.05 for the RFC image and 2.20 for the CRDS-66 image. Both contour maps show a compact source, with some extended structure visible to the north-east in the RFC image. It should be noted the image noise in the CRDS image is almost a factor of 8 higher than the RFC image. It should be noted that only X-band contour maps were available for comparison. Overall, I obtained a satisfactory result when comparing the CRDS images to the rfc_2019c images, which confirms that the images from CRDS

sessions can be used reliably to analyse and monitor the structure of AGN reference sources in the south.

I present VLBI contour maps as well as structure analysis results for 90 AGN reference sources, of which 31 were imaged on VLBI scales for the first time. From the 90 sources, 6 sources were imaged only at S-band, 21 sources were imaged only at X-band, and 63 sources were imaged at both S- and X-band. A total of 54 sources were imaged in only one epoch, and 36 sources were imaged in more than one epoch. Using the SC, it was found that at S-band, 35 sources had a compactness ratio of 0.90 or higher, indicative of very good astrometric quality. For 52 sources, an SI at S-band was calculated between 1 and 2 indicating their suitability as good calibrators. The results from the radial extent calculations showed that the above mentioned 52 sources are all compact in nature and core-dominated. For the remainder of the sources, the extended emission was confirmed by the presence of jet-like structures seen in the contour maps of these sources. Multi-epoch imaging with analysis is recommended for these sources using future CRDS sessions.

For the X-band observations, 33 sources had an SC of 0.90 or higher that is indicative of very good astrometric quality. It was found that these 47 sources have an SI at X-band between 1 and 2 that shows that these sources are suitable as calibrator sources. The results from the radial extent calculations showed that 47 sources are all compact in nature and core-dominated. For the remainder of these sources, jet structures in the X-band contour maps confirmed the presence of the extended emission, as indicated by the results from the structure metrics. It should be noted that the high variability between the R_w and $R_{95\%}$ is a result of faint extended features in the sources which were detected only at some epochs depending on the SNR. Generally, such low surface brightness features in a source have a negligible impact on the quality of the source as calibrator.

Among the 63 sources which were imaged at both S- and X-band, I found that 36 sources showed compact source structure at both observing bands. For the remaining 27 sources, it was found that for 25 sources, the X-band structure tends to be more compact, while for 2 sources the S-band structure tends to be more compact. A total of 18 sources was imaged from the CRDS-94 session to analyse their astrometric quality for potential selection as an ICRF-3 *defining* source. Among the 18 sources, three sources: J1103-5357, J1118-4638 and J1514-4748 were selected as *defining* sources.

In the geodetic and astrometric VLBI observations, sources with low SI and high SC are selected to minimize the effect of source structure on the VLBI observables, such as measurements of the station position coordinates and EOP. The imaging and astrometric quality assessment of the sources from the CRDS geodetic and astrometric

VLBI observations show the importance of a routine imaging campaign in the Southern Hemisphere. The VLBI analysis suggests that the majority of the sources observed in CRDS sessions are compact and will make good reference sources. However, there are a few sources where source structure variability has been detected. I recommend including these sources for regular observations so that imaging can be done and their astrometric quality can be assessed over time. The ICRF sources are also used in VLBI phase-referencing observations where SC is the most important factor. Therefore imaging results from CRDS sessions can also be useful to select good calibrator sources for astronomical phase-referencing observations.

The purpose of this study was to select a geodetic and astrometric VLBI session in the Southern Hemisphere that can be used for imaging. The CRDS sessions run by the IVS community, have been successfully utilised for the imaging and source structure analysis. The VLBI images and results from the additional analysis will be available on the HartRAO website in the near future for public use.

Chapter 6

Future Work

The contour maps and results from the source structure analysis used in this study successfully proved that the CRDS geodetic and astrometric VLBI sessions can be used for studying the astrometric quality of the ICRF sources in the Southern Hemisphere. There are only a few VLBI stations and only a few sessions in the Southern Hemisphere used for observing ICRF sources in the deep South. For this reason, the CRDS programme plays a crucial role and should be used continuously for imaging and structure analysis in the South. In the following sections, I discuss plans for future work using CRDS observations.

6.1 Continuous VLBI imaging

As referred to earlier, the number of CRDS sessions per year is approximately five or six, which is almost one CRDS session every two months. Therefore, routine VLBI imaging at S- and X-band using the CRDS experiments will provide a good opportunity to monitor source structure and variability over time.

Additional CRDS sessions after the CRDS-94 will be analysed, and results will be available shortly after the publication of this thesis. For continuous imaging, an automated process is needed to reduce the time of calibration and editing. I will use *ParselTongue* ([Kettenis et al., 2006](#)), a Python interface of AIPS, for this purpose.

6.2 Investigating source structure in VGOS observations

The VLBI Global Observing System (VGOS; Hase et al., 2012) is a great improvement from the traditional dual-frequency S/X-band systems, and will be fully operational in the near future. Source structure poses a challenge for the VGOS systems which will observe over a wide frequency range of 2-14 GHz. Initial tests have shown that source structure would significantly affect VGOS observations, and the development of mitigation methods is required for more precise delay measurements in future. While it is clear that it is important to investigate the effect of frequency-dependent source structure over the entire VGOS band, it is not clear how to choose a common reference point for correction of the measured delay at all frequencies. A routine imaging programme such as the one presented in this work will be important to investigate the effect of frequency-dependant source structure over the entire VGOS band and to choose a common reference point for correction at all frequencies.

6.3 Effects of source structure on station position estimation

As stated earlier, the quasars used in the ICRF are not always point-like and can exhibit time-dependent source structures. The effect on VLBI observables such as station coordinates, cannot be ignored if the stability of the ICRF is to be maintained in the near future. Shabala et al. (2014a) investigated the effects of source structure on estimated station coordinates from simulated geodetic VLBI data.

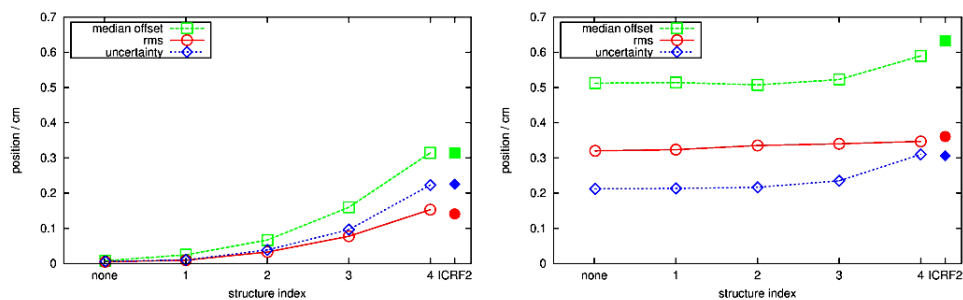


FIGURE 6.1: Source structure effects on station coordinate offsets. Green indicates measured and true values, red indicates debiased rms and blue represents median formal uncertainty. A 15-day CONT11 campaign was used for the simulation. The left panel indicates the structure-only simulation and the right panel shows the full simulation. The filled symbols are for the ICRF-2 distribution of sources. Picture courtesy: Stas Shabala.

In the work, models of radio sources with two-component structures from a mock catalogue have been used where the brighter component represents the core and the

secondary component represents the jet. Figure 6.1 shows the effects of source structures on station coordinates where a decrease in both accuracy (green line) and precision (red and blue lines) is seen when the SI is increased. The right panel of the figure shows results from a full simulation that includes also the contribution from the troposphere, where the effect of the source structure is still evident. These results show that source structure can contribute significantly to the station position uncertainties (at the mm level), and should be corrected or mitigated. Similar results were obtained for the estimated EOP. The study further shows that the source structure in radio sources degrade the quality of solutions for EOP.

I suggest that similar studies should be done using source models from VLBI images obtained from the CRDS sessions to measure the contribution of source structures on the station position measurements and EOP.

6.4 Core-shift effect

The accuracy of the ICRF is largely dependent on the radio-core (bright and point-like feature at the base of the jet) position in the *defining* sources. It is widely known that the core position is frequency-dependent (Blandford & Königl, 1979; Lobanov, 1998). The change of the VLBI core position with frequency is known as the core-shift effect.

If the VLBI core position is R_0 at an observing frequency ν , then the core-shift is described as

$$R_0(\nu) \propto \nu^{-\frac{1}{p}}, \quad (6.1)$$

where p depends on the physical properties of the jet. Jung et al. (2015) suggested a novel approach to estimate the core-shift effect using multi-frequency VLBI observations where a relative core position at lower frequency is measured first. The results using the VLBA observations of AGN indicate a typical core shift of 1.2 mas between 1.4 GHz and 15.4 GHz, and of 2.04 mas between 5 GHz and 15.4 GHz.

I suggest a campaign to calculate core shift in the southern sources below a declination of -30° between S- and X-band using VLBI observations such as CRDS sessions.

6.5 ICRF-*Gaia* transfer sources in the CRDS sessions

The *Global Astrometric Interferometer for Astrophysics* (*Gaia*; Gaia Collaboration et al., 2016) mission started in 2014 July and is busy surveying the entire sky, including observing extragalactic sources. One of the primary goals of this mission is to define

the Gaia Celestial Reference Frame (GCRF; [Le Bail et al., 2016](#)) in the optical domain, which will be aligned with the ICRF-3 in the future to establish the consistency of a fundamental reference frame. The LAB has identified 195 sources to align the GCRF with the ICRF-2. The sources have been selected based on their high optical magnitude ($V \sim 18$), astrometric quality and are known as the ICRF2-*Gaia* transfer sources. I have cross-matched the ICRF2-*Gaia* source list with the CRDS source list and found 19 common sources.

I propose future observations where additional radio bright AGN in the south, with an optical magnitude of ~ 18 will be included in CRDS schedules for routine imaging and astrometric quality analysis. This way CRDS sessions can contribute to increasing the number of ICRF-*Gaia* transfer sources in the South.

Bibliography

- Alef W., Graham D. A., 2002, in Ros E., Porcas R. W., Lobanov A. P., Zensus J. A., eds, Proceedings of the 6th European VLBI Network Symposium. p. 31
- Altamimi Z., Rebischung P., Metivier L., Collilieux X., 2016, *Journal of Geophysical Research: Solid Earth*, 121, 6109
- Basu S., de Witt A., Quick J. F. H., Bertarini A., Leeuw L., 2014, in Behrend D., Baver K. D., Armstrong L., eds, IVS 2014 General Meeting Proceedings "VGOS: The New VLBI Network". pp 426–430
- Beasley A. J., Gordon D., Peck A. B., Petrov L., MacMillan D. S., Fomalont E. B., Ma C., 2002, *ApJS*, 141, 13
- Bergeron J., 1992, *Transactions of the International Astronomical Union, Series B*, 21
- Blandford R. D., Königl A., 1979, *ApJ*, 232, 34
- Boehm J., et al., 2017, The VLBI SOuthern Astrometry Project (SOAP)
- Cappallo R. J., 2017, fourfit user's manual. MIT Haystack Observatory
- Charlot P., 1990a, *AJ*, 99, 1309
- Charlot P., 1990b, *AAP*, 229, 51
- Charlot P., 2002, in Vandenberg N. R., Baver K. D., eds, *International VLBI Service for Geodesy and Astrometry: General Meeting Proceedings*. p. 233
- Charlot P., 2008, in Finkelstein A., Behrend D., eds, *Measuring the Future, Proceedings of the Fifth IVS*. p. 345
- Charlot P., Lestrade J.-F., Boucher C., 1988, in Babcock A. K., Wilkins G. A., eds, *IAU Symposium Vol. 128, The Earth's Rotation and Reference Frames for Geodesy and Geodynamics*. p. 91
- Charlot P., Hough D. H., Lestrade J.-F., 1989, *AAP*, 211, 261

- Charlot P., Fey A. L., Collioud A., Ojha R., Boboltz D. A., Camargo J. I. B., 2008, in Jin W. J., Platais I., Perryman M. A. C., eds, IAU Symposium Vol. 248, A Giant Step: from Milli- to Micro-arcsecond Astrometry. pp 344–347
- Collioud A., Charlot P., 2009, in Bourda G., Charlot P., Collioud A., eds, 19th European VLBI for Geodesy and Astrometry Working Meeting. pp 19–22
- Cotton W., 1979, AJ, 84, 1122
- Diamond P. J., Conway J., Kembell A., Desai K., 2017, in , AIPS COOKBOOK. The National Radio Astronomy Observatory
- Fey A. L., Charlot P., 1997, ApJS, 111, 95
- Fey A. L., Charlot P., 2000, ApJS, 128, 17
- Fey A. L., Clegg A. W., Fomalont E. B., 1996, ApJS, 105, 299
- Fey A. L., Eubanks M., Kingham K. A., 1997, AJ, 114, 2284
- Fey A. L., et al., 2004, AJ, 127, 3587
- Fey A. L., Boboltz D. A., Ojha R., 2008, in Bridle A. H., Condon J. J., Hunt G. C., eds, Vol. 395, Frontiers of Astrophysics: A Celebration of NRAO's 50th Anniversary. p. 366
- Fey A. L., et al., 2015, AJ, 150, 58
- Fomalont E., 1981, National Radio Astronomy Observatory Newsletter, 3, 3
- Fomalont E., 1995, in Zensus J. A., Diamond P. J., Napier P. J., eds, ASP Conference Series Vol. 82, Very Long Baseline Interferometry and the VLBA. pp 363–378
- Fomalont E. B., Wright M. C. H., 1974, in Verschuur G. L., Kellermann K. I., eds, Galactic and Extragalactic Radio Astronomy. Springer, New York, Heidelberg, Berlin
- Fomalont E. B., Petrov L., MacMillan D. S., Gordon D., Ma C., 2003, AJ, 126, 2562
- Gaia Collaboration et al., 2016, A&A, 595, A1
- Gary D. E., 2018, Fourier Synthesis Imaging, <https://web.njit.edu/~gary/728/Lecture6.html>
- Gontier A.-M., et al., 2002, Advancement in Space Research, 30, 185
- Gontier A.-M., Arias E. F., Barache C., 2006, in Souchay J., Feissel-Vernier M., eds, The International Celestial Reference System and Frame - ICRS Center Report for 2001-2004. IERS Technical Note: 34. pp 7–21

- Gordon D., 2019, The International Celestial Reference Frame (ICRF) from VLBI, https://science.gsfc.nasa.gov/sci/content/uploadFiles/highlight_files/icrf3-17June22.pdf
- Guinot B., 1979, in McCarthy D. D., Pilkington J. D. H., eds, IAU Symposium Vol. 82, Time and the Earth's Rotation. pp 7–18
- Guoqiang T., Ronnang B., Baath L., 1987, AAP, 185, 87
- Hase H., Behrend D., Ma C., Petrachenko B., Schuh H., Whitney A., 2012, in Seventh General Meeting (GM2012) of the international VLBI Service for Geodesy and Astrometry (IVS). pp 8–12
- Högbom J. A., 1974, AAPS, 15, 417
- Jacobs C., et al., 2018, in 42nd COSPAR Scientific Assembly. pp B2.1–31–18
- Johnson M., et al., 2019, , 51, 273
- Jung T., et al., 2015, Journal of Korean Astronomical Society, 48, 277
- Kettenis M., van Langevelde H. J., Reynolds C., Cotton B., 2006, in Gabriel C., Arviset C., Ponz D., Enrique S., eds, Vol. 351, Astronomical Data Analysis Software and Systems XV. p. 497
- Kormendy J., Richstone D., 1995, ARAA, 33, 581
- Kormendy J., Fisher D. B., Cornell M. E., Bender R., 2009, ApJS, 182, 216
- Kovalev Y. Y., Petrov L., Fomalont E. B., Gordon D., 2007, AJ, 133, 1236
- Kovalevsky J., Feissel M., 1996, in Ferraz-Mello S., Morando B., Arlot J.-E., eds, IAU Symposium Vol. 172, Dynamics, Ephemerides, and Astrometry of the Solar System. p. 455
- Lanyi G. E., et al., 2010, AJ, 139, 1695
- Le Bail K., et al., 2016, AJ, 151, 79
- Lister M. L., et al., 2009, AJ, 138, 1874
- Lobanov A. P., 1998, A&A, 330, 79
- Lovell J. E. J., et al., 2000, in Hirabayashi H., Edwards P. G., Murphy D. W., eds, Astrophysical Phenomena Revealed by Space VLBI. pp 183–188
- Ma C., et al., 1998, AJ, 116, 516

- Ma C., et al., 2009, IERS Technical Note, 35
- Magorrian J., et al., 1998, AJ, 115, 2285
- Marr J. M., L. S. R., Kurtz S. E., 2016, Fundamentals of Radio Astronomy: Observational Methods. Series in Astronomy and Astrophysics, CRC Press
- Michelson A. A., 1890, Publ. Astron. Soc. Pac., 2, 115
- Michelson A. A., 1920, ApJ, 51, 257
- NRAO 2018, Interferometers, <https://www.cv.nrao.edu/course/astr534/Interferometers1.html>
- Ojha R., et al., 2004a, AJ, 127, 3609
- Ojha R., Fey A. L., Jauncey D. L., Lovell J. E. J., Johnston K. J., 2004b, ApJ, 614, 607
- Ojha R., et al., 2005, AJ, 130, 2529
- Petrov L., Kovalev Y. Y., Fomalont E., Gordon D., 2005, AJ, 129, 1163
- Petrov L., Kovalev Y. Y., Fomalont E. B., Gordon D., 2006, AJ, 131, 1872
- Petrov L., Kovalev Y. Y., Fomalont E. B., Gordon D., 2008, AJ, 136, 580
- Petrov L., Phillips C., Bertarini A., Murphy T., Sadler E. M., 2011, MNRAS, 414, 2528
- Petrov L., de Witt A., Sadler E. M., Phillips C., Horiuchi S., 2019, MNRAS
- Plank L., et al., 2017, Journal of Geodesy, 91, 803
- Readhead A. C. S., Wilkinson P. N., 1978, ApJ, 223, 25
- Ryle M., Vonberg D. D., 1946, Nature, 158, 339
- Schalinski C. J., Alberdi A., Elósegui P., Marcaide J. M., 1988a, in Reid M. J., Moran J. M., eds, IAU Symposium Vol. 129, The Impact of VLBI on Astrophysics and Geophysics. p. 39
- Schalinski C. J., Alef W., Witsel A., Campbell J., Schuh H., 1988b, in Reid M. J., Moran J. M., eds, IAU Symposium Vol. 129, The Impact of VLBI on Astrophysics and Geophysics. p. 359
- Schuh H., Behrend D., 2012, Journal of Geodynamics, 61, 68
- Schwab F. R., Cotton W. D., 1983, AJ, 88, 688

- Shabala S., Titov O., Lovell J., McCallum J., Blanchard J., Watson C., Dickey J., 2012, in Behrend D., Baver K. D., eds, IVS 2012 General Meeting Proceedings “Launching the Next-Generation IVS Network”. pp 329–333
- Shabala S., McCallum J., Plank L., Böhm J., 2014a, in Behrend D., Baver K. D., Armstrong K. L., eds, International VLBI Service for Geodesy and Astrometry 2014 General Meeting Proceedings: “VGOS: The New VLBI Network”. Science Press, Beijing, China, pp 421–425
- Shabala S. S., Rogers J. G., McCallum J. N., Titov O. A., Blanchard J., Lovell J. E. J., Watson C. S., 2014b, *Journal of Geodesy*, 88, 575
- Shaffer D. B., Marscher A. P., Marcaide J., Romney J. D., 1987, *ApJ*, 314, L1
- Shepherd M. C., 1997, in Hunt G., Payne H., eds, *Astronomical Society of the Pacific Conference Series Vol. 125, Astronomical Data Analysis Software and Systems VI*. p. 77
- Steel W. H., 1967, *Interferometry*. Cambridge University Press, Cambridge
- Taylor G. B., Carilli C. L., Perley R. A., 1999, in *Synthesis Imaging in Radio Astronomy II*.
- Thomas J. B., 1979, in 10th Ann. Precise Time and Time Interval (PTTI) Appl. and Planning Meeting.
- Thompson A. R., 1989, in Perley R. A., Schwab F. R., Bridle A. H., eds, *ASP Conf. Ser. Vol. 6, Synthesis Imaging in Radio Astronomy: A Collection of Lectures from the Third NRAO Synthesis Imaging Summer School*. p. 11
- Thompson A. R., Moran J. M., Swenson G. W., 2001, *Interferometry and Synthesis in Radio Astronomy*, 2 edn. Wiley, New York
- Xu M. H., Heinkelmann R., Anderson J. M., Mora-Diaz J., Karbon M., Schuh H., Wang G. L., 2017, *Journal of Geodesy*, 91, 767
- de Witt A., Gordon D., Jacobs C. S., Krasna H., McCallum J., Quick J., Bertarini A., 2018, in *Proceedings of the 10th IVS General Meeting*. p. E1
- de Witt A., Le Bail K., Jacobs C., Gordon D., Mayer D., Schartner M., Basu S., 2019a, in *International VLBI Service for Geodesy and Astrometry 2018 General Meeting Proceedings: ”Global Geodesy and the Role of VGOS - Fundamental to Sustainable Development*. pp 189–193

de Witt A., Gordon D., Jacobs C. S., Krasna H., McCalum J., Quick J., Soja B., 2019b,
in Proceedings of the 24th European VLBI for Geodesy and Astrometry (EVGA).
p. P306